Numerical Investigations of a Trapped Vortex Hydrogen Burner

Tarun Hegde

Delft University of Technology

TU Delft

Numerical Investigations of a Trapped Vortex Hydrogen Burner

by

Tarun Hegde

to obtain the degree of Master of Science

at the Delft University of Technology,

to be defended publicly on Friday August 30, 2024.

Student Number:	5694752	
Project Duration:	December 2023 - August 2024	
Thesis Committee:	Prof.dr.ir. S.A. Klein	Supervisor, TU Delft
	Dr. A.M.J. Felden	Supervisor, TU Delft
	Dr.ir. M.J. Tummers	TU Delft
	Dr. I. Langella	TU Delft

An electronic version of this thesis is available at http://repository.tudelft.nl/.

Cover Image: Generated using AI

TU Delft

Abstract

The use of hydrogen in gas turbines is promising to help with the energy transition since there are no carbon-based pollutants released during its combustion. However, the transition from fossil fuels to hydrogen in gas turbines involves significant challenges. Hydrogen flames exhibit higher flame speed, making burners more prone to flashback, which in turn can cause damage by propagating upstream into the premixing sections. To avoid this type of failure, it is necessary to understand the different mechanisms that can cause flame flashback in gas turbines and develop strategies to help reduce the flashback tendency of hydrogen flames. The FlameSheet™ burner, originally developed by Power Systems Manufacturing (PSM), is a two-stage burner that can be used with fuels having high content of hydrogen. The geometry of the main stage includes a 180-degree bend (U-bend). This feature, which abruptly changes the flow direction of the air-fuel mixture, creates a trapped vortex which helps in stabilizing the flame in the main stage. Such a design makes the burner more resistant to flame flashback.

In this thesis, a numerical study is done on an academic trapped vortex burner, inspired by the FlameSheet™ design using Ansys Fluent. Initially, a cold flow simulation of the flow inside the main stage of the burner was performed using RANS. This was followed by a parametric study (using RANS) of the cold flow patterns while varying several parameters like the shape of the inner liner tip, channel height ratio and the distance between the tip and outer wall of the U-bend. From these results, useful insights were gained by analyzing and comparing the velocity profiles in different parts of the U-bend. To gain more information from some of the relevant cases, large eddy simulations (LES) were used. With the LES results, two-point correlations and cumulative distribution functions of the velocity field were made to describe the cold flow behaviour in the main stage of the burner. These results confirmed that the tip shape and its distance from the U-bend are significant parameters since they affect the velocity profile in the boundary layers of the flow. This change in the velocity profile of its boundary layer can alter the flashback tendency of hydrogen flames in the burner. Along with these cold flow simulations, a reactive simulation was also performed with the original geometry of the trapped vortex burner to understand the flow features inside, in the presence of a flame. Super adiabatic flame temperature and non-uniform diffusion of hydrogen into the flame were observed at various points in the flame.

Acknowledgements

I would like to express my gratitude to all those who helped in the completion of this thesis.

Firstly, I would like to thank my supervisors, Sikke Klein and Anna Felden, for their support and guidance throughout the duration of my thesis. The opportunity to work on such an interesting topic was given to me by Sikke. The regular discussions during our update meetings and his encouragement have helped me push myself and achieve a lot during the last seven months. Special thanks to Anna for being a great supervisor. Her patience, knowledge on numerical modelling for combustion, helpful suggestions that were given in our weekly meetings and also her comments on reviewing this thesis have helped in improving the quality of this work. Without their motivation, a lot of work that was done in this thesis would have been impossible to achieve.

I would also like to thank Rene Pecnik for the insightful discussion we had on analysing the turbulent structures in the burner and also Mathieu Pourquie for allowing me to use the Reynolds cluster to run my simulations. My sincere thanks also go to Mark Tummers and Ivan Langella for being part of my graduation committee.

I would like to extend my gratitude to Rafael Pichler for sharing his insights on the trapped vortex burner. Our discussions in the Combustion Lab were very helpful in understanding flashback and also the impact of certain geometrical features on the flashback phenomenon.

I am also grateful for the support of my family and friends (both from Delft and Bangalore). Their encouragement and belief in my abilities have helped me push through several obstacles in life.

Thank you for being part of this wonderful journey!

Tarun Hegde
Delft, August 2024

Contents

Nomenclature

Non-dimensional Numbers

Symbol	Definition
Da_T	Damkohler number
Ka_T	Karlovitz number
Le	Lewis number
Re	Reynolds number

Symbols

Symbol	Definition	Unit
C_p	Pressure coefficient	[-]
D	Mass diffusivity	[m^2/s]
g_c	Critical velocity gradient	[1/s]
g_f	Flow velocity gradient	[1/s]
k	Turbulent kinetic energy per unit mass	[m^2/s^2]
L	Length scale	[m]
p	Pressure	[Pa]
S_L	Laminar flame speed	[m/s]
S_{lo}	Unstretched laminar flame speed	[m/s]
S_{ls}	Stretched laminar flame speed	[m/s]
S_t	Turbulent flame speed	[m/s]
T	Temperature	[K]
T_U	Unburnt mixture temperature	[K]
T_B	Burnt mixture temperature	[K]
u	Velocity	[m/s]
X	Mole fraction	[-]
Y	Mass fraction	[-]
$y+$	Wall y plus	[-]
α	Thermal diffusivity	[m^2/s]
β	Empirical factor	[-]
ρ	Density	[kg/m^3]
μ	Dynamic molecular viscosity	[kg/m/s]

Symbol	Definition	Unit
μ_t	Dynamic eddy viscosity	[kg/m/s]
ν	Kinematic molecular viscosity	[m^2/s]
ν_{sgs}	Subgrid eddy viscosity	[m^2/s]
ν_t	Kinematic eddy viscosity	[m^2/s]
ϕ	Equivalence ratio	[-]
δ	Boundary layer thickness	[m]
δ_L	Laminar flame thickness	[m]
δ_{lo}	Unstretched laminar flame thickness	[m]
τ	Shear stress	[N/m^2]

1

Introduction

Climate change is one of the most pressing challenges of our time, reshaping countries and economies for the present and future generations. In order to overcome this challenge, it is necessary to reduce the emission of greenhouse gases (mainly CO_2, methane and nitrous oxide), which have continued to increase over the last century [1, 2]. This increasing trend for CO_2 is shown in Figure 1.1. Countries around the world have signed various agreements like the popularly known Paris Agreement [3] in 2015 and recently, at COP28 (28th annual United Nations climate meeting), organized in Dubai, UAE, parties have agreed that they need to "transition away from fossil fuels in energy systems" [4].

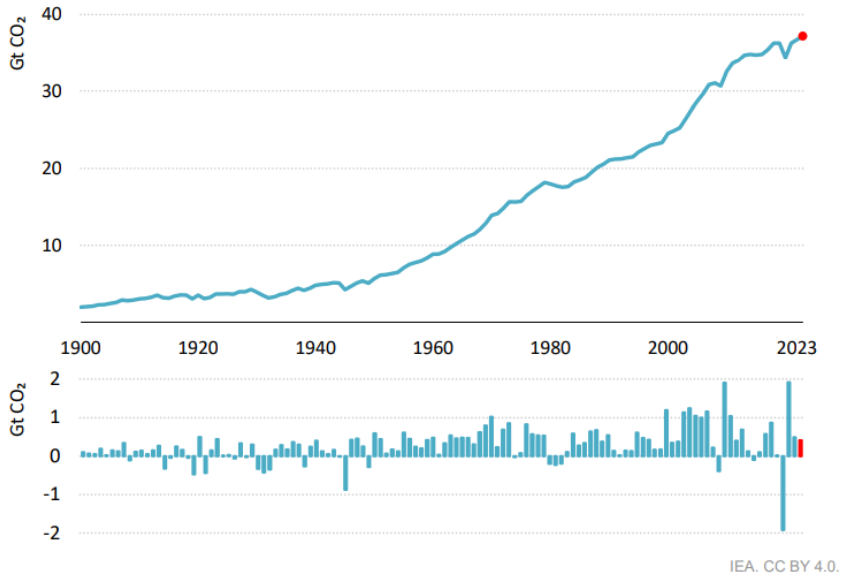

Figure 1.1: Increased emissions of CO_2 and their annual change from 1900-2023. Source: International Energy Agency [2]

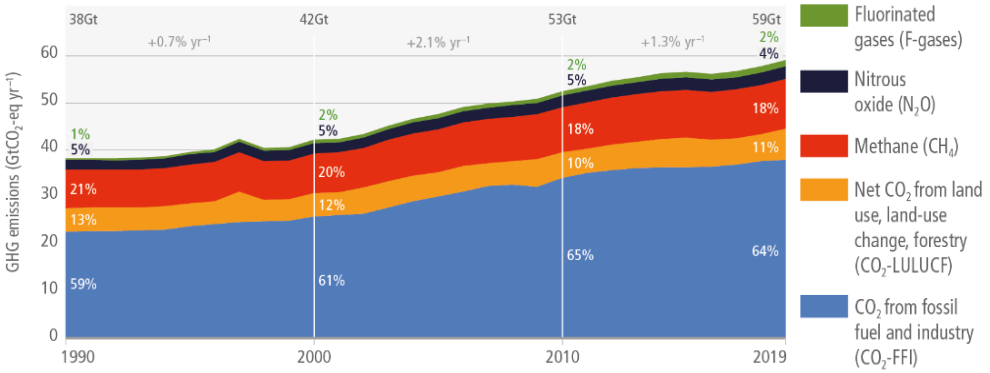

Figure 1.2: Global net anthropogenic greenhouse gas (GHG) emissions from 1900-2019. Source: [1].

Figure 1.2 shows how the various greenhouse gas (GHG) emissions have been changing in the last century and clearly most of it (about 64% in 2019 [1]) is comprised of CO_2 from fossil fuels (coal, oil and natural gas) and industrial processes. Another breakdown of how the various sectors contribute to GHG emissions is shown in Figure 1.3. Energy systems contributed 34% of the global GHG emissions in 2019 [5]. In the energy sector, fossil fuels like coal and natural gas are primarily used for generating electricity. Therefore, to meet the sustainability goals related to climate action, it is important we decarbonize our energy sectors and start developing technologies that facilitate the use of renewable sources of energy efficiently.

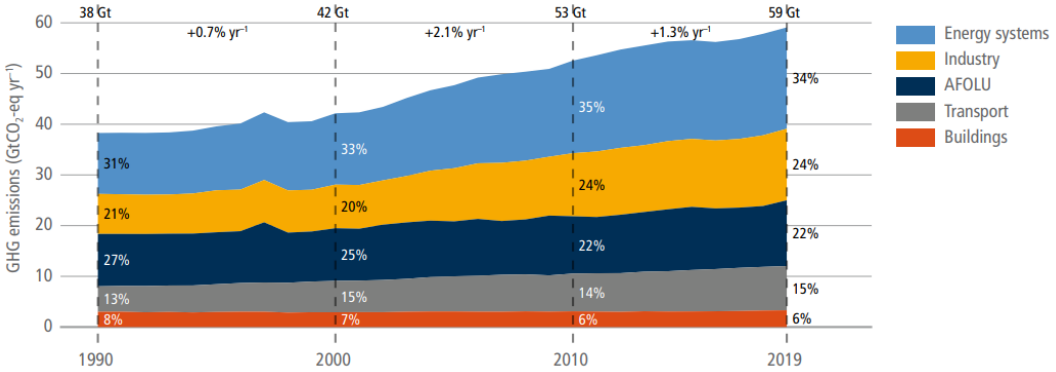

Figure 1.3: Trends in global GHG emissions by sector. Source: [5].

Renewable sources of energy (such as wind, solar, hydro, etc.) are variable and intermittent in nature and that is the major obstacle that needs to be overcome in order to fully transition away from fossil fuels [6]. To overcome this challenge, the excess energy that is available during low power demand should be stored in some form. This stored energy can then be utilized during excess demand for power. Hydrogen fuel, which can be produced from a variety of processes like electrolysis and thermolysis [6], can be used as an energy storage medium to overcome this fluctuating problem with renewable energy.

During excess energy demand, the stored hydrogen can be used in gas turbines which have

been modified with combustors that can support hydrogen combustion. Gas turbines are a popular choice for power generation because of their high efficiency, short start-up times and high turn-down ratios [7]. Another advantage of using hydrogen for combustion is that no CO_2 is released during combustion, making it a promising solution to balance the intermittent nature of the renewable energy sources and also help in reducing the emission of GHGs into the atmosphere.

Gas turbines normally operate in lean premixed mode (Section 2.4) in order to minimize NO_x emissions (nitrogen oxides that cause pollution). NO_x emissions depend on temperature and are reduced when the temperature of the flame is decreased [7]. This reduction in flame temperature is possible in lean premixed mode due to presence of excess air. However, the use of 100% H_2 fuels is not easy due to differences in properties (thermal and mass diffusivities, higher laminar flame speed and adiabatic flame temperature, etc.) [6, 8] compared to conventional fuels like natural gas.

Since H_2 flames burn with a higher flame velocity compared to natural gas, the flame velocity can exceed the incoming (or approaching) flow velocity of the unreacted mixture. This increases the risk of the flame propagating upstream, into the premixing section of the combustor, where the fuel and air is mixed [7]. This phenomenon is called flame flashback and can be dangerous, damaging the premixing section of the gas turbine. Section 1.1 will introduce the various types of flashback and then explain boundary layer flashback more in detail.

1.1. Flame Flashback

In this Section we will talk about flame flashback. Section 1.1.1 will be about the various mechanisms by which flashback can occur. This will be followed by a description of boundary layer flashback (one of the mechanisms which will be the focus of our work) in Section 1.1.2 and Section 1.1.3 will discuss the various numerical work done to study boundary layer flashback.

1.1.1. Flame Flashback Mechanisms

Flashback occurs when the flame front propagates upstream into the premixing section of the combustor [9]. This phenomenon can damage the premixing section (where fuel and air are mixed to form a homogenous mixture) of the combustor due to the high temperature of the flame. This flame flashback can occur because of four different mechanisms [9, 10]:

- **Core flow flashback:** This occurs when the flame velocity is greater than the flow velocity in the core region of the flow. Generally, the core flow velocity is higher than the flame velocity in gas turbines. Hence, this type of flashback rarely occurs.
- **Combustion instability induced flashback:** During combustion, instabilities can be generated due to unsteady heat release, fluctuations in flow field, interaction of acoustic modes. These instabilities can lead to flow reversals which leads to flashback in com-

bustors.

- **Combustion induced vortex breakdown (CIVB):** This type of flashback mechanism is found in swirl stabilized gas turbine combustors (Shown in Figure 1.4). In these combustors, a recirculation zone is created to stabilize the flame using swirling flows. In some cases when the fuel rate is increased, an upstream motion of the recirculation zone can happen, which may cause the vortex to breakdown while it is inside the premixing duct, leading to flashback.

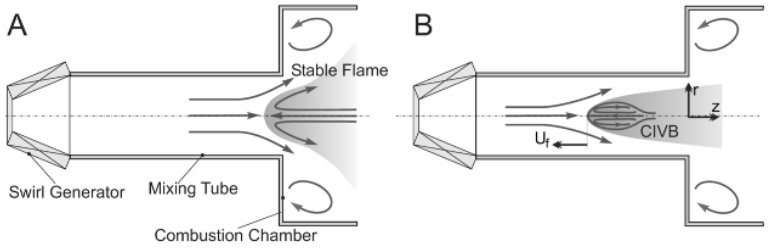

Figure 1.4: Figure showing a swirl stabilized premixed flame. A) Stable flame B) Flashback due to CIVB. Figure from [11]

- **Boundary layer flashback:** Flashback occurs when the local flame velocity is larger than the local flow velocity [7, 10]. This can happen in the boundary layer of the flow, where the flow velocity gradually decreases towards the wall. This is because of the wall's no-slip boundary condition which indicates there is no relative motion between the wall surface and the fluid at the interface. Figure 1.5 shows an example of a flame undergoing boundary layer flashback.

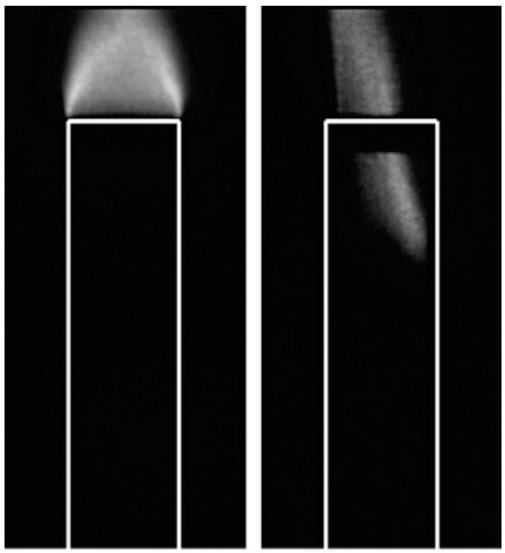

Figure 1.5: Figure showing a stable flame (left) and the flame undergoing boundary layer flashback (right). Source: [12]

Since this work focuses on boundary layer flashback, the other mechanisms will not be discussed further.

1.1.2. Boundary Layer Flashback Mechanism

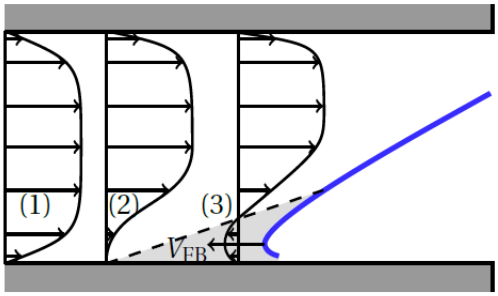

Figure 1.6: Mechanism of boundary layer flashback from [7]

The mechanism behind boundary layer flashback (in a confined geometry) can be explained using Figure 1.6. The velocity profile represented by (1) is an undisturbed turbulent flow inside a channel. Close to the flame tip (denoted by the blue curve), the undisturbed profile (1) is disfigured (2) due to an increase in pressure upstream of the flame. If this pressure rise increases above a critical value, then the flow separates from the surface (3) and a backflow region (light grey colored area) is formed close to the flame tip.

This was investigated by Eichler [10] who studied boundary layer flashback experimentally using Particle Image Velocimetry (PIV) and OH* chemiluminescence. Inside this backflow region, the flame propagates upstream with a flame speed V_{FB}. The absolute value of V_{FB} is greater than the mixture's burning velocity since the reversed flow velocity inside the backflow region would help in accelerating the propagating flame front [7].

Eichler [10] also studied flame flashback under the influence of adverse pressure gradients (with a diffuser channel) and suggested that the frequency of low axial velocity structures close to the wall may play a role in boundary layer flashback. An increased frequency of such structures might increase the flashback propensity of the flame.

1.1.3. Boundary Layer Flashback Modelling

Lewis and von Elbe [13] were first to study boundary layer flashback experimentally using laminar methane-air flames. Using the results of their experiments, they developed a model which uses the velocity gradients at the wall to identify if flashback happens or not. This model is known as the critical velocity gradient model (CVG).

Lewis and von Elbe [13, 14] assumed the velocity profile to be linear near the wall. They have also assumed flow and flame to be uncoupled (flow-flame interaction is neglected). The flame

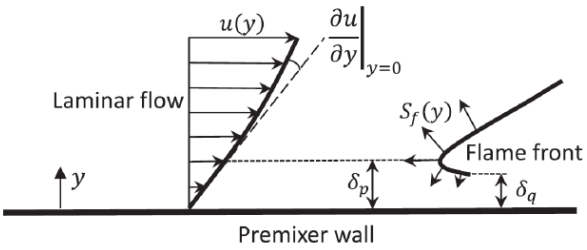

Figure 1.7: Figure showing the parameters used in the CVG model from [9].

front is quenched at a distance δ_q (Unit: [m]) from the wall and when flashback occurs, the flame speed is equal to the incoming flow speed at distance δ_p from the wall. This δ_p is the penetration distance (Unit: [m]). According to the model, flashback occurs when:

$$\frac{\partial u}{\partial y} < \frac{S_L}{\delta_p} \tag{1.1}$$

The term on the right hand side of Equation 1.1 is called the critical velocity gradient and is denoted by g_c (Unit: [s^{-1}]) and the term on the left hand side is the flow velocity gradient which is denoted by g_f (Unit: [s^{-1}]).

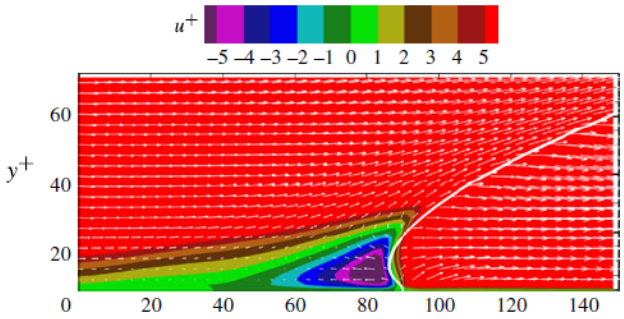

Figure 1.8: Figure describing BLF. The white line depicts the flame front. As the streamlines approach the flame front, they curve due to the presence of adverse pressure gradient in front of the flame. This lowers the flow velocity which can lead to separation and hence flame flashback. Source: [15]

Eichler [10] showed that the flame has a back-pressure effect on the incoming flow which was ignored in the critical velocity gradient model. This back-pressure effect causes the flow upstream to slow down and separate, allowing the flame to propagate upstream. This was confirmed by Gruber et al. [15] using direct numerical simulations (DNS) and shown in Figure 1.8. Figure 1.8 shows how the streamlines curve as they approach the flame front (indicated by the white line in Figure 1.8). They [15] found that if the velocity is low enough, separation will take place which will lead to flame flashback. Large eddy simulations (LES) have also been used to study boundary layer flashback and the effect of the size of the backflow region, upstream of the flame was investigated by Endres et al. [16, 17]

Using the assumption that boundary layer flashback occurs due to flow separation upstream

of the flame front due to adverse pressure gradients, Hoferichter et al. [7, 18, 19] developed a semi-analytical model which could predict flashback. The model uses Stratford's turbulent boundary layer separation criterion [20] which was developed for a flat plate. This approach was improved at TU Delft [21, 22] by using a generic boundary layer separation criterion. This modification made it possible to predict flashback limits for simple and complex geometries [23]. Similarly, several other models [24, 25] have been developed by various research groups to predict the flashback limits of gas turbines.

1.2. FlameSheet™ Combustor

The FlameSheet™ combustor, developed by Power Systems Manufacturing (PSM) [26, 27, 28], can use fuel blends with up to 80% per volume of hydrogen [29]. Figure 1.9 shows the interior design of the FlameSheet™ combustor with its two stages: an outer (main) burner and a central (pilot) burner. A key feature of the main stage is the presence of a 180 degree inversion (Figure 1.9b) in flow direction around a tip (inner liner tip). This creates a trapped-vortex which disrupts the turbulent boundary layer, making the burner more resistant to flame flashback [30].

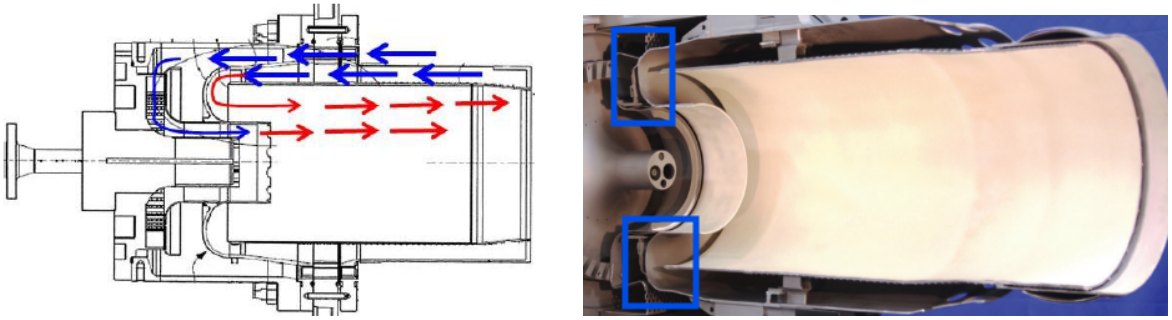

(a) (b)

Figure 1.9: (a) Design of the FlameSheet™ combustor from [26]. The airflow through the main and pilot stages are shown with blue arrows. The red arrow represents the fuel-air mixture. (b) Another image of the FlameSheet™ burner in which the 180 degree bend regions are marked within the blue boxes

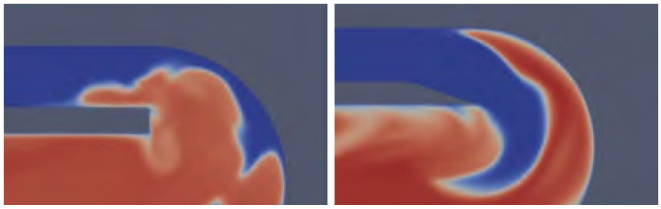

Figure 1.10: Instantaneous temperature field when flashback occurs with different inner liner tips: blunt tip (left) and sharp tip (right) [30]. The figure shows how the flame follows an inner route, closer to the tip, when the tip is blunt and an outer route when it is sharp

Gruber et al. [30] performed LES simulations on a simplified FlameSheet™ combustor, validated with experimentally obtained data, to gain valuable information on boundary layer flashback inside the combustor. They performed simulations with different shapes (blunt and sharp)

of the inner liner tip, around which the flow makes the 180 degree turn. From their results, they observed that the flame follows an inner route, closer to the tip, when the tip is blunt and an outer route, away from the tip, when it is sharp (Figure 1.10). They also found that the ratio of the channel thickness (ratio H2/H1 in Figure 5.3), upstream and downstream of the U-bend, can be an important parameter in controlling flashback. Further development of the FlameSheet™ burner is in progress within the Helios project, which is a cooperation between TU Delft and Thomassen Energy.

1.3. Trapped Vortex Burner

The trapped vortex burner is inspired by the FlameSheet™ design, but exhibits significant differences in its main features such as a simplified inner liner tip geometry and a flattened channel-way. It is a simplified, two dimensional burner which also has a U-bend shape to create a trapped vortex in its main stage to help in stabilizing the flame. Figure 1.11 shows the isometric view of the trapped vortex burner which will be used in this work.

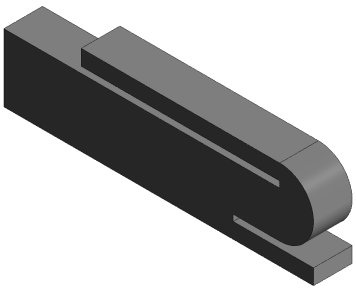

Figure 1.11: Isometric view of the trapped vortex burner

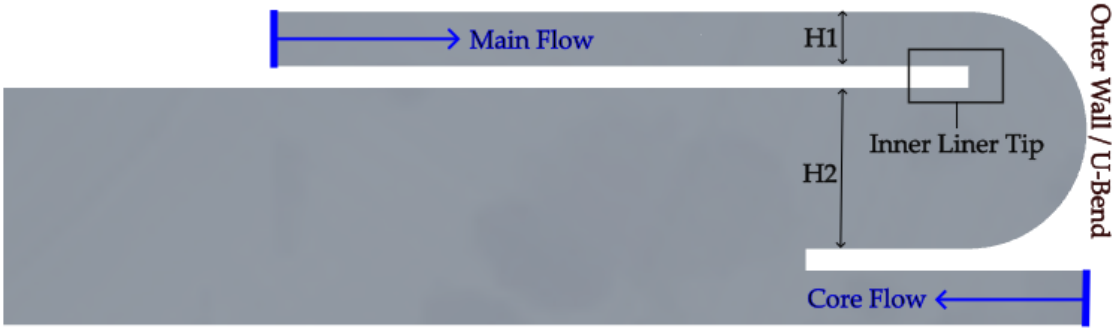

Figure 1.12: Side view of the trapped vortex burner showing the main parts - inner liner tip, the outer wall (or U-bend) and the channel heights H1 and H2. The inlets (main and core flow) are shown with blue arrows.

Figure 1.12 shows the side view of the burner with some of the relevant parts which will be studied in this work. The blue arrows show the main and core flow inlets. Our research focuses on optimizing the geometry of the trapped vortex burner to mitigate flashback risks, while

expanding its operational capabilities. This can be done by utilizing numerical simulations. The results from a base-case simulation (non reactive) will help in understanding the turbulent flow dynamics inside the burner, particularly in the U-bend region since this is where the flame propagates upstream [30]. Once we understand the role played by the near-wall turbulent structures in flame flashback, we can investigate the impact of various geometry features (such as distance of the outer wall from the tip, shape of the inner liner tip and height of the channel H2, etc.) and look at ways in which the design can be modified to improve flashback resistance.

1.4. Research Objectives

The current work will aim to accomplish the following objectives:

- What are the computational model requirements necessary to study the boundary layer in the U-bend section of the trapped vortex burner?
  - It is necessary to have a computational model which can accurately simulate the flow inside the combustor. This includes selecting appropriate turbulence models, mesh resolutions, and numerical schemes. Initially, the simulations will be conducted for non-reacting flows. Validation against experimental data (PIV data available for burner) will be done to ensure the accuracy of the computational simulations. This objective will help in identifying the turbulent structures near the wall using numerical simulation.
- What effect does the geometry of the U-bend and inner liner tip have on the turbulent structures and how can this be used to reduce flashback tendency of the flame?
  - The distance of the U-bend from the inner liner tip is one of the parameters that can be altered to observe its effect on the turbulent flow inside the combustor, particularly in the area adjacent to the wall as this is the region where the flame tends to propagate upstream. Other parameters could be the shape of the tip liner and the height of the main flow inlet which were investigated in [30]. These two parameters were found to be important in deciding the route taken by the flame to flashback in the main stage.

1.5. Thesis Outline

This thesis report is divided into eight chapters (including this chapter). In Chapter 2, the concepts related to turbulent flows and premixed combustion will be discussed. This chapter will introduce topics such as turbulent boundary layers, laminar and turbulent flames which are necessary to understand turbulence modeling and flame flashback. Chapter 3 details the various methodologies used in numerical simulations for both cold (absence of combustion) and reactive flows. There, we introduce the basics of modeling turbulent flows using RANS (Reynolds-averaged Navier Stokes) and LES (Large Eddy Simulation) and also some of the

combustion closure models used in LES.
The numerical assumptions used in this work are argued in Chapter 4. Along with the description of the numerical trapped vortex burner setup, the validation of the model with experimental data is also shown in this chapter. A numerical study with different geometry modifications using RANS is shown in Chapter 5. Using these results, some of the interesting cases were selected for an analysis with LES which is shown in Chapter 6. Chapter 7 shows the reactive simulations done on the trapped vortex burner. Finally, Chapter 8 includes the conclusion along with recommendations for future work.

2

Turbulent flows and Combustion

In this chapter, the theory behind turbulent flows and combustion will be discussed. Since this thesis investigates a turbulent hydrogen combustion setup, it is necessary to understand the basic principles and concepts which will be useful while performing and analyzing turbulent flow simulations.

Section 2.1 discusses the conservation equations needed for reacting and non-reacting flows. Turbulent flows will be discussed in Section 2.2. Section 2.3 explains how the reaction rates are computed in chemical kinetics and finally Section 2.4 discusses the relevant topics in pre-mixed combustion.

2.1. Governing Equations

In this section, the various conservation equations (mass, momentum, species and energy), required to study reacting and non-reacting flows will be discussed.

2.1.1. Mass Conservation

The conservation of mass, also known as the continuity equation, applied to a fluid passing through an infinitesimal control volume is shown below [31]:

$$\frac{\partial \rho}{\partial t} + \frac{\partial \rho u_i}{\partial x_i} = 0 \tag{2.1}$$

where ρ is the fluid density [kg/m^3], which refers to only gas in this work and u_i is the fluid velocity component [m/s].

2.1.2. Momentum Conservation

Momentum conservation, also known as the Navier-Stokes equation, is derived by applying Newton's Second Law to a fluid passing through an infinitesimal control volume, describing the changes of the flow momentum in space and time. For a Newtonian fluid, the Navier-Stokes equation is given by [31]:

$$\frac{\partial \rho u_j}{\partial t} + \frac{\partial \rho u_i u_j}{\partial x_i} = -\frac{\partial p}{\partial x_j} + \frac{\partial \tau_{ij}}{\partial x_i} + S_{M,i} \tag{2.2}$$

where p is the pressure [Pa], $S_{M,i}$ is the volumetric source term or the body force and τ_{ij} is the viscous stress tensor [N/m^2] given by:

$$\tau_{ij} = -\frac{2}{3}\mu \frac{\partial u_k}{\partial x_k}\delta_{ij} + \mu(\frac{\partial u_i}{\partial x_j} + \frac{\partial u_j}{\partial x_i}) \tag{2.3}$$

where μ is the dynamic viscosity and δ_{ij} is the Kronecker symbol (δ_{ij} = 1 if i = j and 0 otherwise).

The left hand side of Equation 2.2 shows the inertial effects where the first term represents the change in momentum with time and the second term denotes the convective effects on momentum. On the right hand side, the first two terms show the influence of surface forces and the last term denotes the body force effects on momentum.

2.1.3. Species Conservation

Conservation of mass for species k is given by [31]:

$$\frac{\partial \rho Y_k}{\partial t} + \frac{\partial}{\partial x_i}[\rho(u_i + V_{k,i})Y_k] = \dot{\omega}_k \tag{2.4}$$

where Y_k is the mass fraction of species k in an N - species mixture, $V_{k,i}$ is the i - component of the diffusion velocity V_k for species k and $\dot{\omega}_k$ is the reaction rate (explained further in Section 2.3.1). Equation 2.4 can also be written in the following form:

$$\frac{\partial \rho Y_k}{\partial t} + \frac{\partial}{\partial x_i}(\rho u_i Y_k) = -\frac{\partial}{\partial x_i}(\rho V_{k,i} Y_k) + \dot{\omega}_k \tag{2.5}$$

In this form, the left hand side contains a transient term and a convective term, which was also observed in the Navier-Stokes equation (Equation 2.2). The first term on the right hand side is also a convective term but with the diffusion velocity $V_{k,i}$ instead of the mixture velocity u_i.

The diffusion term $V_{k,i}Y_k$ can be approximated by Fick's law which assumes the pressure gradients to be small and neglects volume forces [31], assumes binary diffusion coefficients are equal (diffusion coefficient between any two species is D). This is expressed by:

$$V_{k,i}Y_k = -D\frac{\partial Y_k}{\partial x_i} \tag{2.6}$$

For this thesis Fluent's Full Multicomponent Diffusion Model [32], which is a more detailed approach for calculating the diffusion term, is used. This model uses Maxwell-Stefan equations to compute the diffusion term which is given in Equation 2.7.

$$V_{k,i}Y_k = -\sum_{j=1}^{N-1} D_{ij}\frac{\partial Y_k}{\partial x_i} - D_{T,i}\frac{1}{T}\frac{\partial T}{\partial x_i} \tag{2.7}$$

where D_{ij} is the binary mass diffusion coefficient of species i in species j and $D_{T,i}$ is the thermal (Soret) diffusion coefficient, which considers the diffusion of mass caused by temperature gradients. This thermal diffusion is important for a light species like H_2 [33].

2.1.4. Energy Conservation

In energy conservation, both total enthalpy and sensible enthalpy can be applied. The relation between the two terms is given below [31]:

$$h_k = \int_{T_o}^{T} C_{pk}dT + \Delta h^o_{f,k} \tag{2.8}$$

where h_k is the total enthalpy, first term on the right hand side ($\int_{T_o}^{T} C_{pk}dT$) is the sensible enthalpy h_{sk} and the second term is the chemical enthalpy, which is the enthalpy of species k at a reference temperature T_o. C_{pk} is the specific heat of species k.

The energy conservation equation is derived by applying the First Law of Thermodynamics to a fluid passing through an infinitesimal control volume. The enthalpy used here is the sensible enthalpy [31]:

$$\frac{\partial \rho h_s}{\partial t} + \frac{\partial}{\partial x_i}(\rho u_i h_s) = \frac{Dp}{Dt} - \frac{\partial q_i}{\partial x_i} + \tau_{ij}\frac{\partial u_i}{\partial x_j} + \dot{\omega}_T + \dot{Q} + S_H \tag{2.9}$$

where the third term on the right hand side is the viscous dissipation term, $\dot{Q}$ is the heat source term and the last term is the body force. The energy flux term (second term on the right side) includes a heat diffusion term from Fourier's law and a species diffusion related enthalpy term (Equation 2.10).

$$q_i = -\lambda\frac{\partial T}{\partial x_i} + \rho\sum_{k=1}^{N} h_{s,k}Y_k V_{k,i} \tag{2.10}$$

The heat release $\dot{\omega_T}$ is given by:

$$\dot{\omega}_T = -\sum_{k=1}^{N} \Delta h^o_{f,k}\dot{\omega}_k \tag{2.11}$$

2.2. Turbulent Flows

2.2.1. Introduction to Turbulent flows

Turbulent flows are quite relevant in our surroundings. Unlike laminar flows which are smooth and orderly [34], turbulent flows are characterized by irregular, chaotic patterns which also contain structures like eddies and vortices in them [34, 35]. The velocity field for a turbulent flow varies significantly in space and time. Figure 2.1 shows how the variation in velocity field at a point in a turbulent flow looks like.

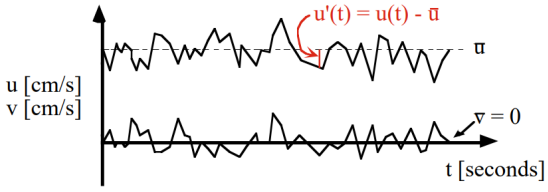

Figure 2.1: Velocity recorded at a point in a turbulent flow over a period of time. u and v represent two components of the velocity field. $\bar{u}$ and $\bar{v}$ represent the mean values of the two velocity components. Source: [36]

The Reynolds number is a non-dimensional number which is used to indicate whether a flow is laminar or turbulent. It is the ratio of inertial forces to viscous forces and this ratio is large for a turbulent flow (for example, Re > 2900 for turbulent pipe flows). Equation 2.12 shows how Re is calculated for a flow with density ρ, dynamic molecular viscosity μ, velocity u and length scale L.

$$Re = \frac{\rho u L}{\mu} \tag{2.12}$$

Turbulent flow consists of eddies, which are vortex-like structures, of various sizes. The largest eddies define the macrostructure and are described by a length scale L, velocity scale U and time scale T ($T \sim L/U$) which depend on the geometry of the flow [35]. Similarly, the smallest eddies are described by a length scale η, time scale τ and a velocity scale v which are also called the Kolmogorov scales [35] and are given by:

$$\eta = \left(\frac{\nu^3}{\epsilon}\right)^{\frac{1}{4}}, \qquad \tau = \left(\frac{\nu}{\epsilon}\right)^{\frac{1}{2}}, \qquad v = (\nu\epsilon)^{\frac{1}{4}} \tag{2.13}$$

Turbulent kinetic energy is produced at the macrostructure through instability processes in the average flow. This energy makes the large eddies unstable and causes them to break up into smaller eddies. This breakup of larger eddies into smaller eddies continues until it reaches the Kolmogorov scales where it is dissipated into heat through viscous friction. This phenomenon is called energy cascade [35].

2.2.2. Turbulent Boundary Layer

When a fluid flows past a wall, a thin layer where the viscous forces are significant starts (due to the no slip boundary condition at the wall) to develop adjacent to the wall. This layer is called the boundary layer [34] and Figure 2.2 shows an example of a boundary layer formed when a fluid flows past an airfoil.

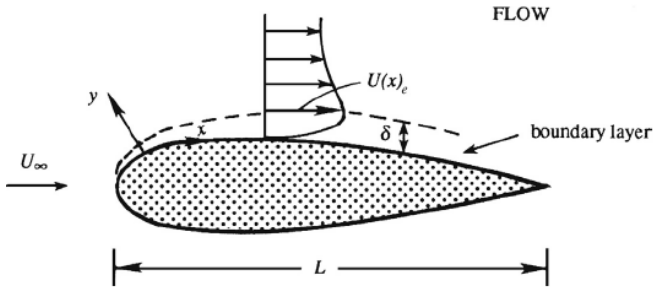

Figure 2.2: Boundary layer over a solid surface from [34]. U_∞ is the free-stream velocity in m/s, δ is the boundary layer thickness in m

In turbulent boundary layer flows, non-dimensional variables like wall distance y^+ (Equation 2.14) and velocity u^+ (Equation 2.15) are used to describe and separate the boundary layers into different regions or sub layers [35]. When wall distance and velocity is expressed in terms of these non-dimensional variables, the flow patterns and behavior becomes universal which helps while developing numerical models.

$$y^+ = \frac{\rho u_\tau y}{\mu} \tag{2.14}$$

$$u^+ = \frac{u}{u_\tau} \tag{2.15}$$

The shear stress velocity u_τ (m/s) is calculated using Equation 2.16, where τ_w is the wall shear stress (N/m^2).

$$u_\tau = \sqrt{\frac{\tau_w}{\rho}} \tag{2.16}$$

The turbulent boundary layer can be divided into different regions depending on the value of y^+ [35].

- **Viscous sublayer** ($y^+ < 5$): The viscous forces are very significant and the velocity profile is given by the following relation:

$$u^+ = y^+ \tag{2.17}$$

- **Buffer layer** ($5 < y^+ < 30$): This is a transition region between the viscous sublayer and the logarithmic region where both viscous and turbulent stresses are important
- **Logarithmic region** ($30 < y^+ < 100$): The velocity profile follows a logarithmic relation and both viscous and turbulent stresses are significant in this region. The velocity profile is given by Equation 2.18 where κ is 0.4 and Π is 2.0 [35].

$$u^+ = \frac{1}{\kappa}[ln(y^+) + \Pi] \tag{2.18}$$

- **Core region** ($y^+ > 100$): Flow is completely turbulent in this region.

Figure 2.3 shows how the velocity profile varies with distance from the wall. Accurate determination of this velocity profile in our simulations is crucial since we focus on near wall turbulent structures close to the wall. This will determine how accurately we capture flame flashback in our non-reactive flow simulations.

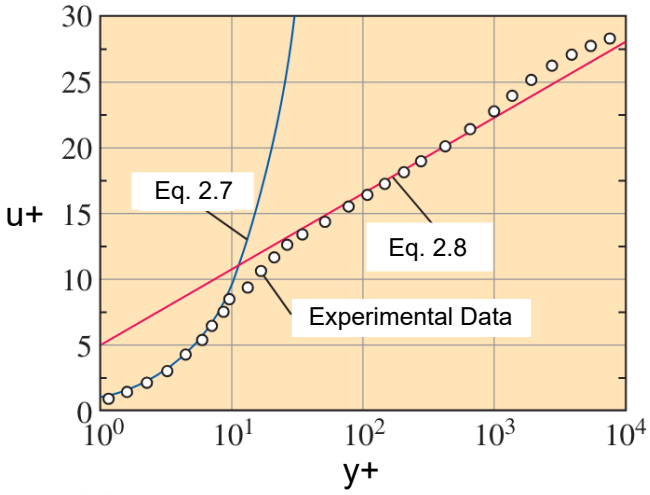

Figure 2.3: u+ as a function of y+ for a fully developed turbulent pipe flow. The figure shows how Equations 2.17 and 2.18 compare with experimental data. Source: [37]

2.3. Chemical Kinetics

Chemical kinetics deals with the reaction rates of different chemical reactions. This information is crucial in understanding how fast a species is produced or consumed during a reaction. Section 2.3.1 will explain how the reaction rate $\dot{\omega}_k$ in Equation 2.4 is calculated and Section 2.3.2 will discuss the details included in a mechanism file.

2.3.1. Computation of Reaction Rate

A chemical mechanism usually contains several elementary reactions. Let us consider an N-species chemical mechanism which contains M elementary reactions, then a reaction can be represented by [31]:

$$\sum_{k=1}^{N} v'_{kj}\mathcal{M}_k \rightleftharpoons \sum_{k=1}^{N} v''_{kj}\mathcal{M}_k \text{ for } j \in [1, M] \tag{2.19}$$

where $\mathcal{M}_k$ denotes species k, v'_{kj} and v''_{kj} are the molar stoichiometric coefficients of species k in reaction j. The total reaction rate of a species $\dot{\omega}_k$ [kg s^{-1} m^{-3}] is the sum of all rates $\dot{\omega}_{kj}$ in M reactions [31]:

$$\dot{\omega}_k = \sum_{j=1}^{M} \dot{\omega}_{kj} = M_k \sum_{j=1}^{M} (v''_{kj} - v'_{kj}) \mathcal{Q}_j \tag{2.20}$$

where M_k is the molecular weight of species k and $\mathcal{Q}_j$ is the rate of progress of reaction j. It is important to remember that the overall mass conservation remains conserved, therefore:

$$\sum_{k=1}^{N} \dot{\omega}_k = 0 \tag{2.21}$$

The progress rate $\mathcal{Q}_j$ of reaction j is given by:

$$\mathcal{Q}_j = K_{fj} \prod_{k=1}^{N} [X_k]^{v'_{kj}} - K_{rj} \prod_{k=1}^{N} [X_k]^{v''_{kj}} \tag{2.22}$$

where $[X_k]$ is the molar concentration ($[X_k] = \rho Y_k / M_k$), K_{fj} and K_{rj} are the forward and reverse rates of reaction j. The reaction rates K_{fj} and K_{rj} are calculated using empirical Arrhenius law [31]:

$$K_{fj} = A_{fj} T^{\beta j} \exp\left(-\frac{E_j}{RT}\right) \tag{2.23}$$

where A_{fj} is the preexponential constant, β_j is the temperature exponent and E_j is the activation energy. All these constants are provided in a mechanism file which will be described in the next section. K_{rj} is calculated from K_{fj} using the following relation [31]:

$$K_{rj} = \frac{K_{fj}}{\left(\frac{p_a}{RT}\right)^{\sum_{k=1}^{N}(v''_{kj} - v'_{kj})} \exp\left(\frac{\Delta S^o_j}{R} - \frac{\Delta H^o_j}{RT}\right)} \tag{2.24}$$

where p_a is the atmospheric pressure, ΔH^o_j and ΔS^o_j are the enthalpy and entropy changes for reaction j.

2.3.2. Mechanism File

The previous section explained how the reaction rate $\dot{\omega}_k$ for a species k is calculated from elementary reactions. In Equation 2.23, there are three constants (the preexponential constant A_{fj}, the temperature exponent β_j and the activation energy E_j) which need to be provided. These constants for all the reactions are provided in a reaction mechanism file.

A reaction mechanism file has N number of species and M reactions. For each reaction, A_{fj}, β_j and E_j values are provided. Figure 2.4 shows an example of a reaction mechanism file, the LiDryer mechanism [38] used for H_2/O_2 combustion. The mechanism has 9 species and 19 reactions.

In chemical kinetics, identifying the species and reactions that need to be considered is a challenge. The presence of certain species or reactions can significantly impact the the computation of reaction rates and also alter the overall chemistry observed in a process like combustion.

		A_{fj}	β_j	E_j
H_2/O_2 chain reactions				
1. $H + O_2 = O + OH$		3.55×10^{15}	−0.41	16.6
2. $O + H_2 = H + OH$		5.08×10^{4}	2.67	6.29
3. $H_2 + OH = H_2O + H$		2.16×10^{8}	1.51	3.43
4. $O + H_2O = OH + OH$		2.97×10^{6}	2.02	13.4
H_2/O_2 dissociation/recombination reactions				
5. $H_2 + M = H + H + M^a$		4.58×10^{19}	−1.40	104.38
$H_2 + Ar = H + H + Ar$		5.84×10^{18}	−1.10	104.38
$H_2 + He = H + H + He$		5.84×10^{18}	−1.10	104.38
6. $O + O + M = O_2 + M^a$		6.16×10^{15}	−0.50	0.00
$O + O + Ar = O_2 + Ar$		1.89×10^{13}	0.00	−1.79
$O + O + He = O_2 + He$		1.89×10^{13}	0.00	−1.79
7. $O + H + M = OH + M^a$		4.71×10^{18}	−1.0	0.00
8. $H + OH + M = H_2O + M^b$		3.8×10^{22}	−2.00	0.00
Formation and consumption of HO_2				
9. $H + O_2 + M = HO_2 + M^c$	k_0	6.37×10^{20}	−1.72	0.52
$H + O_2 + M = HO_2 + M^d$	k_0	9.04×10^{19}	−1.50	0.49
	k_∞	1.48×10^{12}	0.60	0.00
10. $HO_2 + H = H_2 + O_2$		1.66×10^{13}	0.00	0.82
11. $HO_2 + H = OH + OH$		7.08×10^{13}	0.00	0.30
12. $HO_2 + O = OH + O_2$		3.25×10^{13}	0.00	0.00
13. $HO_2 + OH = H_2O + O_2$		2.89×10^{13}	0.00	−0.50
Formation and consumption of H_2O_2				
14. $HO_2 + HO_2 = H_2O_2 + O_2^e$		4.20×10^{14}	0.00	11.98
$HO_2 + HO_2 = H_2O_2 + O_2$		1.30×10^{11}	0.00	−1.63
15. $H_2O_2 + M = OH + OH + M^f$	k_0	1.20×10^{17}	0.00	45.5
	k_∞	2.95×10^{14}	0.00	48.4
16. $H_2O_2 + H = H_2O + OH$		2.41×10^{13}	0.00	3.97
17. $H_2O_2 + H = H_2 + HO_2$		4.82×10^{13}	0.00	7.95
18. $H_2O_2 + O = OH + HO_2$		9.55×10^{6}	2.00	3.97
19. $H_2O_2 + OH = H_2O + HO_2^e$		1.00×10^{12}	0.00	0.00
$H_2O_2 + OH = H_2O + HO_2$		5.8×10^{14}	0.00	9.56

Figure 2.4: An example of the data provided in a mechanism file for all the reactions. This is the LiDryer mechanism for H_2/O_2 combustion which has 9 species and 19 reactions [38]

Several mechanisms are available for computing hydrogen combustion and some of them have been summarized in Table 2.1.

Mechanism	No. of species	No. of reactions	Reference
LiDryer	9	19	[38]
San Diego	9	21	[39]
O Conaire	9	19	[40]
Boivin	9	12	[41]

Table 2.1: Description of some of the mechanism files available for combustion of hydrogen

These mechanism files can be used in CFD simulations to study the reactive flow field inside a combustor. Since this work focuses on hydrogen combustion using lean mixtures, only mechanisms developed for H_2/O_2 combustion are considered, and N_2 is treated as an inert gas. Therefore the emission of NO_x is completely ignored in our work. A typical mechanism file for methane combustion consists of 50 species and over 300 reactions (like GRI 3.0 [42]). But

since we are not considering any hydrocarbon in our fuel-air mixture, the size of the reaction mechanism for hydrogen combustion is reduced to 9 species and about 19-21 reactions.

2.4. Premixed Combustion

In this section, the fundamental theory of combustion related to this research will be discussed. The basic combustion concepts are discussed in Subsection 2.4.1. Sections 2.4.2 and 2.4.3 deal with laminar and turbulent premixed flames respectively. The section on laminar premixed flame introduces topics which will help in understanding the concepts discussed in turbulent premixed flames.

2.4.1. Introduction to Combustion

Combustion is best described as an exothermic reaction between a fuel (H_2 in our case) and an oxidant (like air). Equations 2.25 and 2.26 represent global CH_4 and H_2 combustion reactions taking place under stoichiometric conditions [33]. Stoichiometry is when the fuel and oxidizer consume each other completely. When there is an excess of fuel, the condition is called fuel-rich and the opposite (excess of oxidizer) is called fuel-lean [33].

$$CH_4 + 2\ O_2 + 2 \times 3.76\ N_2 \rightarrow CO_2 + 2H_2O + 2 \times 3.76\ N_2 \tag{2.25}$$

$$H_2 + 0.5\ O_2 + 0.5 \times 3.76\ N_2 \rightarrow H_20 + 0.5 \times 3.76\ N_2 \tag{2.26}$$

The nature of combustion (fuel-rich, fuel-lean or stoichiometric) can be described by the equivalence ratio of the mixture, which is typically denoted by ϕ. ϕ is the ratio of actual fuel-air ratio to the stoichiometric fuel-air ratio [33]:

$$\phi = \frac{(\frac{X_{fuel}}{X_{air}})}{(\frac{X_{fuel}}{X_{air}})_{st}} \tag{2.27}$$

When ϕ > 1, the mixture is said to be fuel-rich and when ϕ < 1, it is fuel-lean.

Depending on how the fuel and oxidizer is mixed, flames can be divided into two categories [33]. If the reactants are mixed first to form a homogeneous mixture and then burned it is called premixed. If combustion and mixing occurs at the same time, it is called non-premixed.

2.4.2. Laminar Premixed Flames

Figure 2.5 shows a one-dimensional, planar premixed flame [43]. The propagation speed of a laminar flame, relative to the mixture flow is called its laminar flame speed and it is denoted by S_L. The thickness of a laminar flame is denoted by δ_L. From this figure, we can identify four regions in laminar premixed flames [44].

- **Unburnt side:** The air-fuel mixture moving from left to right with an inlet velocity u towards the flame front. The mixture has a temperature T_u which denotes the value of the incoming (unburned) mixture temperature. When the inlet velocity is the same as the flame speed (like Figure 2.5), the flame is stationary.

- **Preheat or Diffusion region:** In this region, heat and mass transfer takes place. Heat is transferred from the burnt section to the unburnt mixture and the incoming mixture is convected into this preheat zone. From Figure 2.5, we can see that the temperature of the mixture starts to increase from T_u to T_B due to the diffusion of heat. δ_{PR} in Figure 2.5 represents the thickness of the preheat zone.
- **Reaction zone:** Within this zone, most of the energy production takes place due to combustion of the fuel. Also, the thickness of this zone is lesser than the diffusion zone and is denoted by δ_R.
- **Post-flame zone:** This zone consists of the high temperature products of combustion.

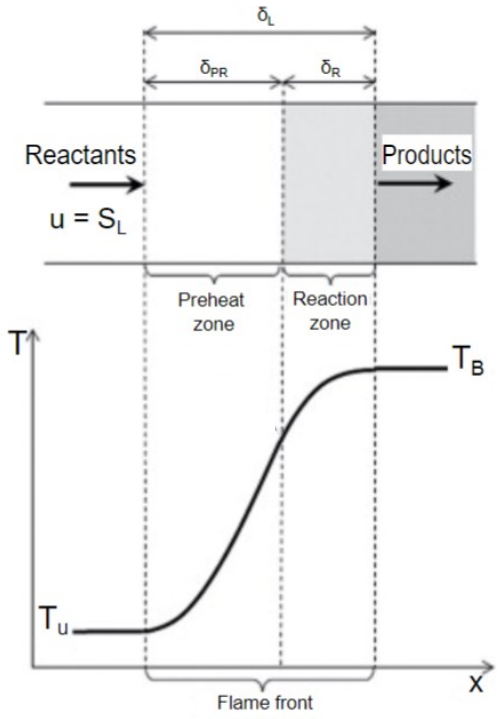

Figure 2.5: One-dimensional, laminar flame structure from [43]

The laminar flame thickness δ_L is the sum of the preheat zone thickness δ_{PR} and reaction zone thickness δ_R.

The relative strength of thermal diffusion and species mass diffusion is described by a non-dimensional number called the Lewis number. It is defined by Equation 2.28 for an $i-$th species in the mixture:

$$Le_i = \frac{\alpha_{mix}}{D_{i,mix}} \tag{2.28}$$

where α_{mix} is the thermal diffusivity [m^2/s] of the mixture which is a measure of heat transfer in the mixture and $D_{i,mix}$ is the mass diffusivity [m^2/s] of an $i-$th species in the mixture which indicates the rate at which a component can diffuse in the mixture. These quantities can be estimated using several approaches. The diffusivities can either be defined as a constant value

for the entire mixture, or as a polynomial function of temperature, or using a multi component model which uses the kinetic theory to calculate the diffusivities [45, 46].

Cantera [47], which is an open source chemical kinetics software, can be used to calculate flame properties like S_L and δ_L by performing one-dimensional, steady state simulations using a reaction mechanism (explained in Section 2.3.2).

2.4.3. Turbulent Premixed Flames

Under the influence of an incoming turbulent flow, the flame front will wrinkle, which leads to an increased surface area and a change in laminar flame properties such as laminar flame velocity. To describe the different regimes in turbulent premixed flames, three time scales need to be computed:

- Integral time scale: It is the ratio of the integral length scale of the large eddies l_o to the velocity fluctuation u' of the large eddies.

$$t_t = \frac{l_o}{u'} \tag{2.29}$$

- Kolmogorov time scale: It is the ratio of the kolmogorov length scale of the smallest eddies η_k to the velocity fluctuation u' of the smallest eddies.

$$t_k = \frac{\eta_k}{u'(\eta_k)} \tag{2.30}$$

- Chemical time scale: It is the ratio of flame thickness δ_L to the laminar flame speed S_L.

$$t_c = \frac{\delta_L}{S_L} \tag{2.31}$$

Using these three time scales, two non-dimensional numbers can be derived for turbulent premixed flames. The Damkohler number compares the integral time scale to the chemical time scale.

$$Da_T = \frac{t_t}{t_c} \tag{2.32}$$

And the Karlovitz number compares the chemical time scale to the kolmogorov scale.

$$Ka_T = \frac{t_c}{t_k} \tag{2.33}$$

Along with these two numbers, the turbulent Reynolds number can also be computed using the following relation:

$$Re_T = \frac{u' l_o}{\nu} \tag{2.34}$$

Using the three non-dimensional numbers defined above, Peters [48] described different regimes in turbulent premixed combustion (Figure 2.6). Various characteristic scales, such as velocity fluctuation u' and an integral length scale of the eddies l_o, were used to classify turbulent flames into different regimes. Figure 2.6 shows the regime classification for premixed turbulent combustion given by Peters [48].

- **Laminar flames:** In this region, where $Re_T < 1$, the flame is laminar in nature
- **Wrinkled flames:** These flames show a wrinkled flame front due to the effect of the incoming turbulent flow. Because of this, they have a higher surface area which increases the burning intensity.
- **Corrugated flames:** In these flames, the velocity fluctuations is higher than the flame velocity which leads to increased wrinkling compared to wrinkled flames. However the internal structure remains unaffected since the $\mathrm{Ka}_T < 1$ which indicates that the flame thickness is less than turbulent length scales and thus the turbulent eddies cannot penetrate into the flame.
- **Thin reaction zone (Thickened wrinkled flames):** In this zone, the kolmogorov eddies can penetrate the preheat zone of the flame ($\mathrm{Ka}_T > 1$). This interaction enhances mixing. The reaction zone remains unaffected.
- **Broken reaction zone (Well-stirred reactor):** For these flames, the kolmogorov eddies can penetrate into the flame and alter the internal structure of the flame.

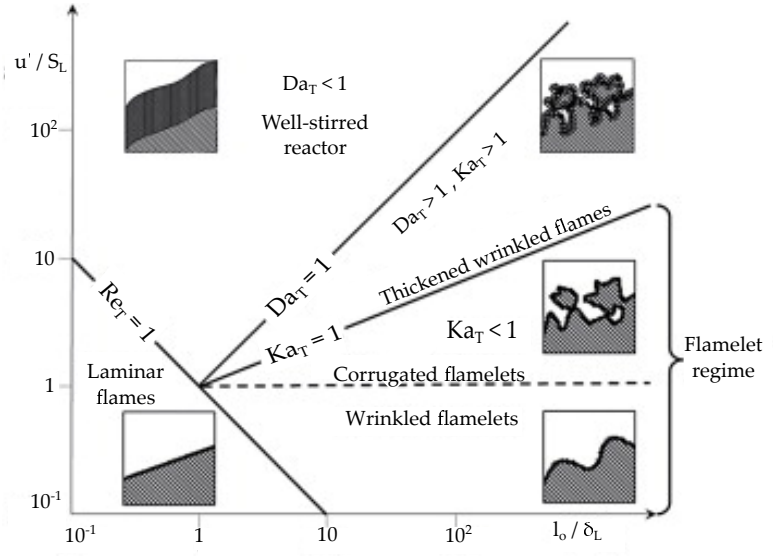

Figure 2.6: Flame regime diagram for premixed turbulent combustion based on Peters [48]. Figure from [43]

In turbulent flames, when the chemical timescale is lesser than the convection and diffusion timescale, combustion can be assumed to take place in thin layers called flamelets [49] which are embedded in turbulent flow. This assumption allows us to treat the turbulent flame as an ensemble of laminar flamelets and such models are called laminar flamelet models which can be used to model wrinkled, corrugated flames and also flames in the thin reaction region.

When the flow becomes turbulent, the flame will propagate with a speed which is also influenced by the incoming turbulent flow [33]. A correlation for turbulent flame speed, denoted by S_t, was first developed by Damköhler in 1940 [23, 33]. Damköhler proposed that the ratio of the wrinkled, total flame surface area A_T (m^2) and the cross-sectional area A (m^2) can be used to obtain the turbulent flame speed [48].

$$\frac{S_t}{S_l} = \frac{A_T}{A} \tag{2.35}$$

2.4.4. Flame Instabilities

In reality, and under specific conditions, several instabilities can be seen to develop and influence the flame surface shape. Examples are hydrodynamic instabilities and thermo-diffusive instabilities which give the flame a cellular structure like the ones shown on the right of Figure 2.7.

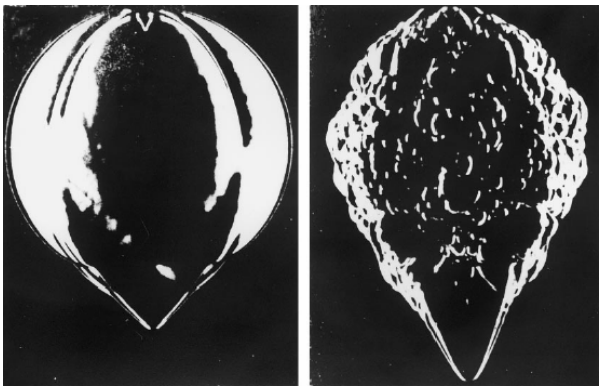

Figure 2.7: Flames formed by burning lean butane-air mixture (left) and lean hydrogen-air mixture(right) from [44], showing a cellular flame structure being formed when hydrogen is used

Hydrodynamic or Darrieus Landau (DL) Instability

Figure 2.8 shows how a planar flame would look when perturbed by an incoming turbulent flow. The flame front shows alternating convex-concave regions. The DL instability occurs due to the expansion of the reactant flow in front of the flame front due to a temperature jump and expansion of the flow over the flame front. The incoming flow will expand sooner in front of the convex regions (towards the reactants) of the flame front. This leads to increase in pressure in front of the convex parts of the flame, which causes the flow to decelerate [44]. In the concave region, the opposite is observed which increases the velocity of the flow. These alternating high pressure (convex) and low pressure (concave) regions allow the flame to move upstream (convex) and downstream (concave), leading to an unstable flame.

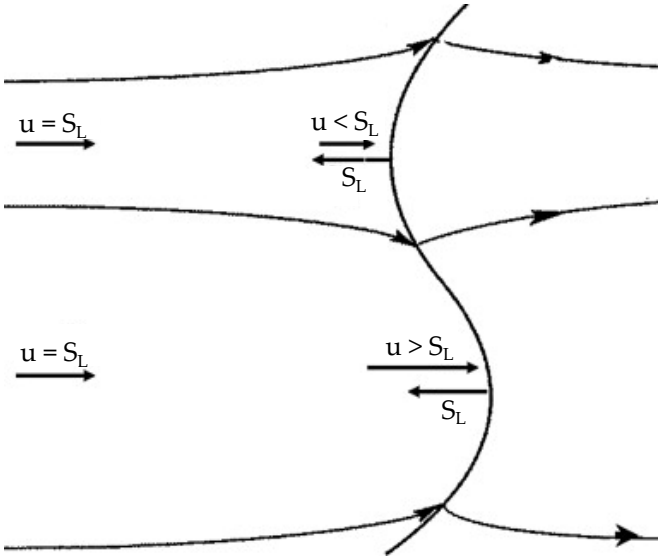

Figure 2.8: Hydrodynamic instability from [50]

Thermo-diffusive Instability

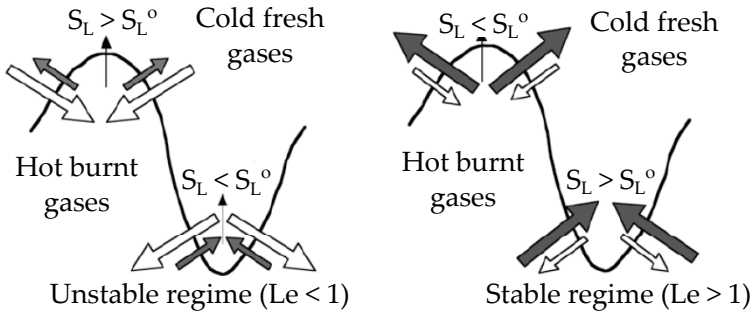

Figure 2.9: Thermo-diffusive instability from [31]. Grey arrow represents diffused heat and the white arrows represent diffused mass.

Thermo-diffusive instabilities occur due to unequal thermal and mass diffusivities (Lewis number $\neq$ 1). Let us consider Figure 2.9. The grey arrows represent diffusion of heat from the product side into the reactants. The white arrows represent mass diffusion of the reactants into the flame. The relative strength of thermal diffusion to mass diffusion is determined by the Lewis number. When Lewis number is less than one, mass diffusivity is greater than thermal diffusivity (reactants diffuse into the flame faster than heat diffuses towards the fresh gases).

The left side of Figure 2.9 shows the case for a flame with Le $<$ 1. In such flames, at the convex regions (towards the reactants), we can see that the white arrows (mass flux) are converging into the curved region. This would indicate an enrichment of reactants at these convex regions, which tends to increase the flame speed. At the concave regions, the opposite effect is observed due to the diverging arrows of mass flux into the flame. This leads to an unstable, wrinkling flame front with growing perturbations [51].

The right side of Figure 2.9 shows a flame front with Le $>$ 1. In such flames, the strength of thermal diffusion is greater than mass diffusion. At the convex sections, the diverging action of the heat flux arrows (grey) would lead to reduced flame speeds due to cooling of the flame. At the concave regions, the grey heat flux arrows converge, which would increase the temperature of the flame, leading to higher flame speeds. This would give a stable flame for Le $>$ 1 [44].

3

Numerical Modeling of Turbulent Flows

In this chapter, the numerical models employed to make the simulation of the cold and reactive flow inside the trapped vortex hydrogen burner will be discussed. Section 3.1 introduces the different approaches to Computational Fluid Dynamics (CFD). Section 3.2 explains how Reynolds-averaged Navier-Stokes (RANS) equations are derived and used in simulations. Finally, Section 3.3 focuses on Large Eddy Simulation (LES), where the equations for both non-reactive and reactive simulations are discussed. These sections will help in understanding the key differences between the various approaches and models.

3.1. Introduction

Computational Fluid Dynamics (CFD) can be used to simulate turbulent flows using three different approaches [31] as can be seen in Figure 3.1

- **Reynolds Averaged Navier Stokes (RANS):** Solve for the mean (ensemble-averaged [35]) flow. The equations are obtained by time averaging the instantaneous governing equations. RANS is extensively used, for instance as a tool in the industry since they utilize less computational resources compared to the other two approaches.
- **Large Eddy Simulations (LES):** The large turbulent scales are calculated explicitly while the smaller scale effects are modeled using subgrid scale models. The equations for LES are obtained by performing filtering operations on the instantaneous governing equations. Only the largest spatial frequencies (up to a cut-off frequency) in the energy spectrum are resolved in LES. LES requires finer grids compared to RANS but coarser grids when compared to DNS.
- **Direct Numerical Simulations (DNS):** All scales of turbulence are solved without any

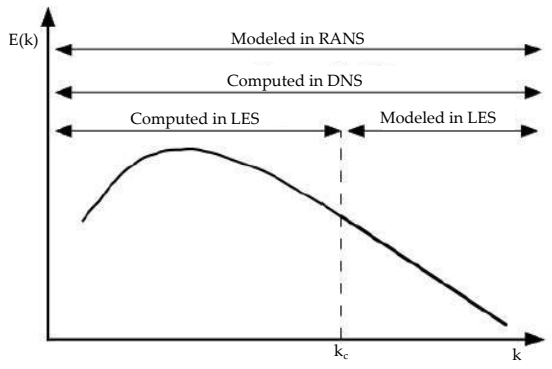

Figure 3.1: Turbulence energy spectrum vs wave number from [31]. E(k) is the turbulence energy spectrum [m^3/s^2] and k is the wavenumber [1/m]. k_c is the cut-off wave number used in LES

model. All spatial frequencies in the energy spectrum are resolved in DNS. DNS requires the most computational resources among the three approaches and are usually limited to low Reynolds numbers. According to Pope [52], the total number of grid nodes needed to resolve a turbulent flow using DNS is given by the following relation:

$$N \sim 4.4Re^{\frac{9}{4}} \tag{3.1}$$

where N is the total number of grid nodes. For an Re value of 7000, approximately 2×10^9 nodes will be required. Due to such expensive computational requirements, DNS is usually limited to low Re values.

3.2. Reynolds Averaged Navier-Stokes Equations (RANS)

3.2.1. Reynolds Decomposition and Favre Averaging

DNS solves all turbulent scales which makes it the best method in principle but the problem with DNS is that the mesh must be very fine and resolved down to the Kolmogorov scales (the smallest turbulent scales). This increases computation costs and is not suitable for all applications. On the otherhand, RANS is less computationally expensive and can be easily used for a lot of industrial applications. This is done by splitting the instantaneous components into two components: a mean (time averaged) quantity and a fluctuating quantity which is shown below for a property f [35].

$$f = \overline{f} + f' \tag{3.2}$$

Where the symbol denotes an averaged quantity and ’ denotes a fluctuating quantity and this splitting into two parts is called Reynolds decomposition. Also, the averaging operator has the following properties (useful in deriving the RANS equations):

$$\overline{a'} = 0 \tag{3.3}$$

$$\overline{a\bar{b}} = \overline{a}\bar{b} \tag{3.4}$$

$$\overline{a'b'} \neq 0 \tag{3.5}$$

This description is sufficient when studying constant density flows. For varying density flows, like combustion, this approach will introduce additional terms because density also needs to be split into a mean and fluctuating term. To avoid this in CFD codes, mass-weighted averages called Favre averages [53] are used:

$$\tilde{f} = \frac{\overline{\rho f}}{\overline{\rho}} \tag{3.6}$$

The tilde operator represents Favre averaging. With this, any quantity f can be split into mean and fluctuating components:

$$f = \widetilde{f} + f'' \tag{3.7}$$

3.2.2. RANS Equations

The RANS equations can be derived by applying favre averaging to the governing equations explained in Section 2.1 [31]:

- **Mass:**

$$\frac{\partial \overline{\rho}}{\partial t} + \frac{\partial}{\partial x_i}(\overline{\rho}\widetilde{u}_i) = 0 \tag{3.8}$$

- **Momentum:**

$$\frac{\partial \overline{\rho}\widetilde{u}_i}{\partial t} + \frac{\partial}{\partial x_i}(\overline{\rho}\widetilde{u}_i\widetilde{u}_j) = -\frac{\partial \overline{p}}{\partial x_j} + \frac{\partial}{\partial x_i}(\overline{\tau}_{ij} - \overline{\rho}\widetilde{u_i'' u_j''}) \tag{3.9}$$

- **Species:**

$$\frac{\partial \overline{\rho}\widetilde{Y}_k}{\partial t} + \frac{\partial}{\partial x_i}(\overline{\rho}\widetilde{u}_i\widetilde{Y_k}) = -\frac{\partial}{\partial x_i}(\overline{V_{k,i}Y_k} + \overline{\rho}\widetilde{u_i'' Y_k''}) + \overline{\dot{\omega}}_k \tag{3.10}$$

- **Energy:**

$$\frac{\partial \overline{\rho}\widetilde{h}_s}{\partial t} + \frac{\partial}{\partial x_i}(\overline{\rho}\widetilde{u}_i\widetilde{h}_s) = \overline{\dot{\omega}}_T + \frac{\overline{Dp}}{Dt} + \frac{\partial}{\partial x_i}\left(\overline{\lambda\frac{\partial T}{\partial x_i}} - \overline{\rho u_i'' h_s''}\right) + \overline{\tau_{ij}\frac{\partial u_i}{\partial x_j}} - \frac{\partial}{\partial x_i}\left(\overline{\rho\sum_{k=1}^{N} V_{k,i}Y_k h_{s,k}}\right) \tag{3.11}$$

From Equation 3.8 to 3.11, the following unknown terms remain unclosed:

- Reynolds stresses ($\widetilde{u_i'' u_j''}$): These terms require a turbulence model which will discussed in Section 3.2.3.
- Species ($\widetilde{u_i'' Y_k''}$) and enthalpy ($u_i'' h_s''$) turbulent fluxes: These fluxes are closed using a gradient assumption [31].
- Laminar diffusive fluxes for species ($\overline{V_{k,i}Y_k}$) or enthalpy ($\overline{\lambda\frac{\partial T}{\partial x_i}}$): These are also closed using a gradient assumption.

- Species chemical reaction rates $\overline{\dot{\omega}_k}$: This term can be closed using a combustion model. In our work, we are using finite rate chemistry with RANS to compute the reaction rate terms.

3.2.3. Turbulence Models for Reynolds Stresses

In the above equations, we can see the appearance of a new term, $\widetilde{u_i'' u_j''}$. This term is called the Reynolds stress and in order to use RANS equations, additional closure models are required to solve them. Eddy viscosity models use the Boussinesq hypothesis, which define an effective eddy viscosity μ_t [kg/m/s] to describe the momentum transfer of turbulent eddies:

$$-\rho\widetilde{u_i'' u_j''} = \mu_t \left(\frac{\partial \widetilde{u}_i}{\partial x_j} + \frac{\partial \widetilde{u}_j}{\partial x_i} \right) - \frac{2}{3} \left(\overline{\rho} k + \mu_t \frac{\partial \widetilde{u}_k}{\partial x_k} \right) \delta_{ij} \tag{3.12}$$

Where k is the turbulent kinetic energy per unit mass [m^2/s^2]. Some popular eddy viscosity models are the $k-\epsilon$, $k-\omega$, $k-\omega$ SST turbulence models [54, 55, 56]. However, the main drawback of these models is that the turbulence is assumed to be isotropic. In order to consider anisotropic turbulence, the Reynolds Stress Model (RSM) can be used where the transport equations for Reynolds Stress are solved. For this thesis, realizable $k-\epsilon$ model, which will be explained in the next section, will be used. In this model, μ_t is estimated using the following relation:

$$\mu_t = \overline{\rho} C_\mu \frac{k^2}{\epsilon} \tag{3.13}$$

where k is the turbulent kinetic energy, ϵ is the turbulent energy dissipation rate, C_μ is a model constant set to 0.09. In order to obtain μ_t, additional equations are required to calculate k and ϵ which will be discussed in the following sections for $k-\epsilon$.

Standard $k-\epsilon$ Model

The standard $k-\epsilon$ model is a two-equation closure model for estimating turbulent kinetic energy k and turbulent energy dissipation rate ϵ. The two equations are given below:

$$\frac{\partial}{\partial t}(\overline{\rho} k) + \frac{\partial}{\partial x_i}(\overline{\rho}\widetilde{u}_i k) = \frac{\partial}{\partial x_i}[(\mu + \frac{\mu_t}{\sigma_k})\frac{\partial k}{\partial x_i}] + P_k - \overline{\rho}\epsilon \tag{3.14}$$

$$\frac{\partial}{\partial t}(\overline{\rho} \epsilon) + \frac{\partial}{\partial x_i}(\overline{\rho}\widetilde{u}_i \epsilon) = \frac{\partial}{\partial x_i}[(\mu + \frac{\mu_t}{\sigma_\epsilon})\frac{\partial \epsilon}{\partial x_i}] + C_{\epsilon 1}\frac{\epsilon}{k} P_k - C_{\epsilon 2}\overline{\rho}\frac{\epsilon^2}{k} \tag{3.15}$$

P_k accounts for the production of turbulent kinetic energy due to the mean velocity gradients and it is given by:

$$P_k = -\overline{\rho}\widetilde{u_i'' u_j''}\frac{\partial \widetilde{u}_i}{\partial x_j} \tag{3.16}$$

The equation has four constants whose default values are given below [54]:

$$\sigma_k = 1.00, \quad \sigma_\epsilon = 1.30, \quad C_{\epsilon 1} = 1.44, \qquad C_{\epsilon 2} = 1.92 \tag{3.17}$$

This model is popular because it is simple and also provides k/ϵ and $\sqrt{\epsilon/\nu}$ which are needed to compute the integral and Kolmogorov scales [31]. However, this model also has some drawbacks. It assumes high Reynolds number, homogenous and isotropic turbulence. The velocity fluctuations due to low frequency motions are underestimated.

Realizable $k-\epsilon$ Model

The realizable $k-\epsilon$ model has two main improvements compared to the standard model [57]:

- A different formulation for turbulent viscosity is used.
- It uses a modified dissipation rate equation by deriving it from an equation for the transport of the mean-square vorticity fluctuation.

The equation for turbulent kinetic energy is the same as Equation 3.14. The modified equation for the dissipation rate is given below [57]:

$$\frac{\partial}{\partial t}(\overline{\rho}\epsilon) + \frac{\partial}{\partial x_i}(\overline{\rho}\widetilde{u}_i\epsilon) = \frac{\partial}{\partial x_i}[(\mu + \frac{\mu_t}{\sigma_\epsilon})\frac{\partial \epsilon}{\partial x_i}] + \overline{\rho}C_1 S\epsilon - \overline{\rho}C_2\frac{\epsilon^2}{k+\sqrt{\nu\epsilon}} \tag{3.18}$$

The eddy viscosity is calculated using Equation 3.13 but instead of using a constant value for C_μ, the following relation is used:

$$C_\mu = \frac{1}{A_0 + A_S\frac{kU^*}{\epsilon}} \tag{3.19}$$

where U^* is calculated using the mean deformation tensor S_{ij} and mean rotation tensor $\widetilde{\omega}_{ij}$. With this, the model takes solid body rotation or reference frame rotation effect on turbulence. They are calculated using the following relations:

$$U^* = \sqrt{S_{ij}S_{ij} + \widetilde{\omega}_{ij}\widetilde{\omega}_{ij}} \tag{3.20}$$

$$S_{ij} = \frac{1}{2}(\frac{\partial \widetilde{u}_i}{\partial x_j} + \frac{\partial \widetilde{u}_j}{\partial x_i}) \tag{3.21}$$

$$\widetilde{\omega}_{ij} = \omega_{ij} - 2\epsilon_{ijk}\omega_k, \quad \omega_{ij} = \overline{\omega_{ij}} - \epsilon_{ijk}\omega_k \tag{3.22}$$

$$\omega_{ij} = \frac{1}{2}(\frac{\partial \widetilde{u}_i}{\partial x_j} - \frac{\partial \widetilde{u}_j}{\partial x_i}) \tag{3.23}$$

where $\overline{\omega_{ij}}$ is the mean rotation rate viewed in a reference frame with angular velocity ω_k, ϵ_{ijk} is an alternating tensor and is equal to 1 if ijk is in cyclic order, -1 when it is anti-cyclic and 0 if any two indices are equal. $C_1 = max[0.43, \eta/(\eta+5)]$, C_2 = 1.9, A_0 = 4.04 and A_S = $\sqrt{6}\cos\phi$, where

$$\eta = k\sqrt{S_{ij}S_{ij}}/\epsilon \tag{3.24}$$

$$\phi = \frac{1}{3}\cos^{-1}(\sqrt{6}\frac{S_{ij}S_{jk}S_{ki}}{\sqrt{S_{ij}S_{ij}}^3}) \tag{3.25}$$

With these modifications, the realizable $k-\epsilon$ model includes the effect of rotation rate, making it perform better than the standard model in a lot of cases like rotating shear flows, channel flows, flows with pressure gradients and backward step flows [57].

3.3. Large Eddy Simulation (LES)

3.3.1. LES Equations

Typically, the small eddies are isotropic in nature and the large eddies are anisotropic and depend on the surrounding geometry and boundary conditions [58]. This principle is used in LES, where the large scale eddies are resolved and the small scale eddies are modeled using models called subgrid scale models.

LES use a spatial filtering operation which is given by:

$$\overline{\phi(x,t)} = \iiint G(x,x',\Delta)\phi(x',t)dx' \tag{3.26}$$

Where $\overline{\phi}$ represents a filtered quantity, G is the spatial filtering operation and Δ is the filter cut-off length (for implicit LES) which is given by:

$$\Delta = (\Delta x \Delta y \Delta z)^{\frac{1}{3}} \tag{3.27}$$

The filtering operation is applied to the governing equations (conservation of mass, momentum, chemical species and enthalpy from Section 2.1) for LES. The tilde operator represents Favre averaging [31].

- **Mass:**

$$\frac{\partial\overline{\rho}}{\partial t} + \frac{\partial}{\partial x_i}(\overline{\rho}\widetilde{u_i}) = 0 \tag{3.28}$$

- **Momentum:**

$$\frac{\partial\overline{\rho}\widetilde{u_i}}{\partial t} + \frac{\partial}{\partial x_j}(\overline{\rho}\widetilde{u_i}\widetilde{u_j}) + \frac{\partial\overline{p}}{\partial x_i} = \frac{\partial}{\partial x_j}[\overline{\tau_{ij}} - \overline{\rho}(\widetilde{u_i u_j} - \widetilde{u_i}\widetilde{u_j})] \tag{3.29}$$

- **Chemical species:**

$$\frac{\partial(\overline{\rho}\widetilde{Y_k})}{\partial t} + \frac{\partial}{\partial x_j}(\overline{\rho}\widetilde{u}_j\widetilde{Y_k}) = \frac{\partial}{\partial x_j}[\overline{V_{k,j}Y_k} - \overline{\rho}(\widetilde{u_j Y_k} - \widetilde{u}_j\widetilde{Y_k})] + \overline{\dot{\omega}_k} \tag{3.30}$$

- **Enthalpy:**

$$\frac{\partial \overline{\rho}\widetilde{h}_s}{\partial t}+\frac{\partial}{\partial x_j}(\overline{\rho}\widetilde{u}_j\widetilde{h}_s) = \frac{\overline{Dp}}{Dt}+\frac{\partial}{\partial x_j}\left[\overline{\lambda\frac{\partial T}{\partial x_j}} - \overline{\rho}(\widetilde{u_j h_s} - \widetilde{u}_j\widetilde{h}_s)\right]+\overline{\tau_{ij}\frac{\partial u_j}{\partial x_i}}-\frac{\partial}{\partial x_j}\left(\overline{\rho\sum_{k=1}^{N} V_{k,i}Y_k h_{s,k}}\right)+\overline{\dot{\omega}_T} \tag{3.31}$$

In the above equations, the following quantities are unclosed and require modeling:

- Unresolved Reynolds stresses, ($\widetilde{u_i u_j} - \widetilde{u}_i\widetilde{u}_j$), which require a subgrid scale turbulence model.
- Unresolved species fluxes ($\widetilde{u_j Y_k} - \widetilde{u}_j\widetilde{Y}_k$) and enthalpy fluxes ($\widetilde{u_j h_s} - \widetilde{u}_j\widetilde{h}_s$)
- Filtered laminar diffusion fluxes for species $\overline{V_{k,j}Y_k}$ and enthalpy $\overline{\lambda\frac{\partial T}{\partial x_j}}$ which are either neglected or modeled using a simple gradient assumption.
- Filtered chemical reaction rate, $\overline{\dot{\omega}_k}$.

3.3.2. Subgrid Scale Turbulence Models for the Reynolds Stresses

In LES, τ_{sgs} is used to represent the subgrid stress [N/m^2] which is given by:

$$\tau_{sgs} = \rho(\widetilde{u_i u_j} - \widetilde{u}_i\,\widetilde{u}_j) \tag{3.32}$$

In order to solve our governing equations with LES, we need an additional model to compute the subgrid stress which includes the effect of the smaller eddies which have been filtered on the larger eddies. Since they are isotropic in nature, eddy viscosity models can be used by using the following relation:

$$\tau_{sgs} = -\nu_{sgs}\left(\frac{\partial\widetilde{u}_i}{\partial x_j}+\frac{\partial\widetilde{u}_j}{\partial x_i}-\frac{2}{3}\delta_{ij}\frac{\partial\widetilde{u}_k}{\partial x_k}\right)+\frac{1}{3}\tau_{kk}\delta_{ij} \tag{3.33}$$

Where ν_{sgs} is the subgrid eddy viscosity [m^2/s] which can be calculated using models like the Smagorinsky model [59] and the wall-adapting local eddy-viscosity (WALE) model [60].

Smagorinsky Model

The Smagorinsky model [59] uses the Boussinesq hypothesis since the smallest eddies are isotropic in nature. It assumes equilibrium between the production and dissipation of subgrid turbulent kinetic energy. The subgrid eddy viscosity is given by:

$$\nu_{sgs} = L_s^2(2\widetilde{S_{ij}}\widetilde{S_{ij}})^{\frac{1}{2}} \tag{3.34}$$

Where L_s is the Smagorinsky length scale and S_{ij} is the strain rate tensor. The Smagorinsky length scale is given by:

$$L_s = C_s\Delta \tag{3.35}$$

The Smagorinsky model is very fundamental and has certain drawbacks. It does not perform accurately in near wall regions because the length scale does not tend to zero and the

Smagorinsky constant C_s is treated as a constant.

The behavior of the model close to the walls can be fixed by using a damping function like the Van Driest damping function which alters the filter length close to the walls.

WALE Model

The wall adapting local eddy-viscosity (WALE) [60] model is another approach to calculating the subgrid eddy viscosity. It is an algebraic model which not only performs well close to the wall, but is also computationally less expensive. The subgrid eddy viscosity is calculated using the following relation:

$$\nu_{sgs} = (C_w \Delta)^2 \frac{(S_{ij}^d S_{ij}^d)^{\frac{3}{2}}}{(\widetilde{S_{ij}}\,\widetilde{S_{ij}})^{\frac{5}{2}} + (S_{ij}^d S_{ij}^d)^{\frac{5}{4}}} \tag{3.36}$$

Where $C_w = 0.325$ and S_{ij}^d is the traceless symmetric part of the square of the velocity gradient tensor:

$$S_{ij}^d = \frac{1}{2}(\widetilde{g_{ij}}^2 + \widetilde{g_{ji}}^2) - \frac{1}{3}\delta_{ij}\widetilde{g_{kk}}^2 \tag{3.37}$$

Where $\widetilde{g_{ij}}$ is the filtered velocity gradient tensor $\frac{\partial \widetilde{u_i}}{\partial x_j}$

3.3.3. Combustion Modeling with LES

Two main challenges exist in LES for turbulent premixed combustion [31]:

- The thickness of the flame is small compared to the mesh size (Figure 3.2). Therefore, it is difficult to resolve the the flame thickness on an LES mesh.
- An important contribution to the reaction rates occur at subgrid scale level, which is not resolved. These contributions must be modeled carefully in order to accurately simulate premixed combustion using LES.

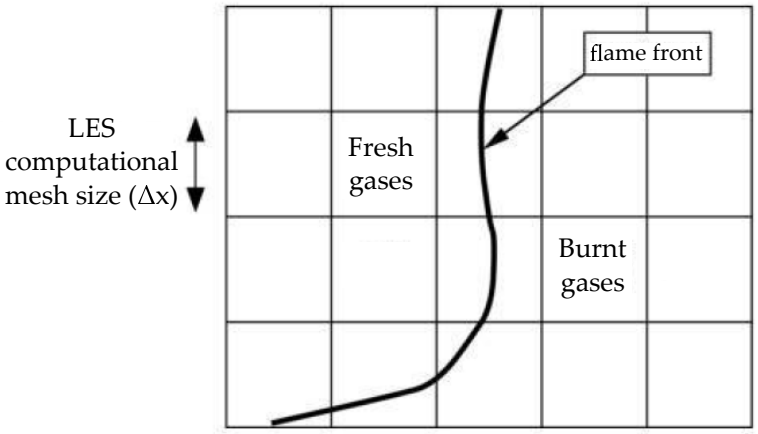

Figure 3.2: Comparing the premixed flame thickness with the LES mesh size from [31]

In the previous section, the closure models for the subgrid stress were discussed. However, in reactive flows, an additional closure model is needed to determine the filtered reaction rate $\overline{\dot{\omega}_k}$ which appears in the conservation of species mass fraction equation shown in Equation 3.30.

Several models [31] are available to calculate this filtered reaction rate and will be discussed in the following sections.

The Eddy Break-up Model (EBU)

The Eddy Break-up model assumes very fast chemistry [31] and it considers the reaction zone to be made up from a collection of fresh and burnt gas pockets, transported by eddies. Therefore, it is only the turbulence parameters that control the reaction rate. This type of assumption is suitable only for fast chemistry reactions with high Re and Da. Using these assumptions, the filtered reaction rate is calculated using the following equation:

$$\overline{w_k} = C_{EBU}\overline{\rho}\frac{\widetilde{c}(1-\widetilde{c})}{\tau_t^{SGS}} \tag{3.38}$$

Where C_{EBU} is a model constant,c is the reduced temperature of the mixture and τ_t^{SGS} is the subgrid turbulent time scale given by:

$$\tau_t^{SGS} = \frac{\Delta}{\sqrt{k_{SGS}}} \tag{3.39}$$

Where k_{SGS} is the subgrid turbulent kinetic energy which is calculated using algebraic expressions or an additional transport equation for k_{SGS} is solved [31].

The model is simple but it has several drawbacks. Firstly, it does not include any chemical kinetics effects (assumes chemistry is quasi instantaneous). Another drawback is the constant C_{EBU} which depends on several parameters and hence becomes dependent on the case setup.

Artificially Thickened Flame (ATF) Model

One of the challenges of performing LES simulations for reactive flows is that the flame thickness cannot be resolved on a given mesh unless it is made very fine. The ATF model bypasses that difficulty by artificially thickening the flame (Figure 3.3) which makes it possible to be resolved on the LES mesh [31] but unfortunately also modifies the turbulence-chemistry interaction. The model consists in multiplying the thermal diffusivity with a factor and dividing the reaction rate with the same factor. This approach should give us the same flame speed as the un-thickened case.

$$S_L \propto \sqrt{\alpha\overline{w_k}} \tag{3.40}$$

$$\delta_L \propto \frac{\alpha}{S_L} = \sqrt{\frac{\alpha}{\overline{w_k}}} \tag{3.41}$$

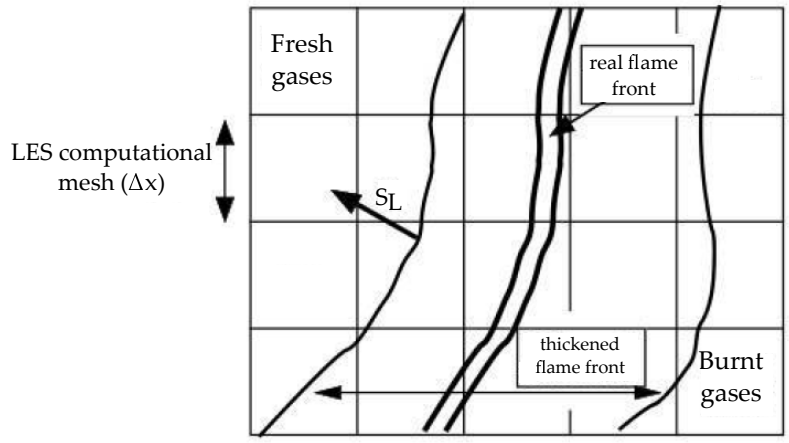

Figure 3.3: Artificially thickened flame from [31] showing the difference between the actual and modified flame thickness, allowing it to be resolved on the LES mesh.

From the above equations, we can see that when the thermal diffusivity α is multiplied and the filtered reaction rate $\overline{w_k}$ is divided by the same factor F, the flame speed remains unchanged and the flame thickness becomes $F\delta_l$.

This approach unfortunately modifies the turbulent-chemistry interactions by decreasing the Damköhler number, making the flame more insensitive to turbulence. This can be rectified by multiplying the reaction rate in Equation 3.30 with an efficiency function $\mathcal{E}$ [58], which models the subgrid scale flame wrinkling, countering the flame surface wrinkling reduction caused by the introduction of thickening factor F.

The G - Equation

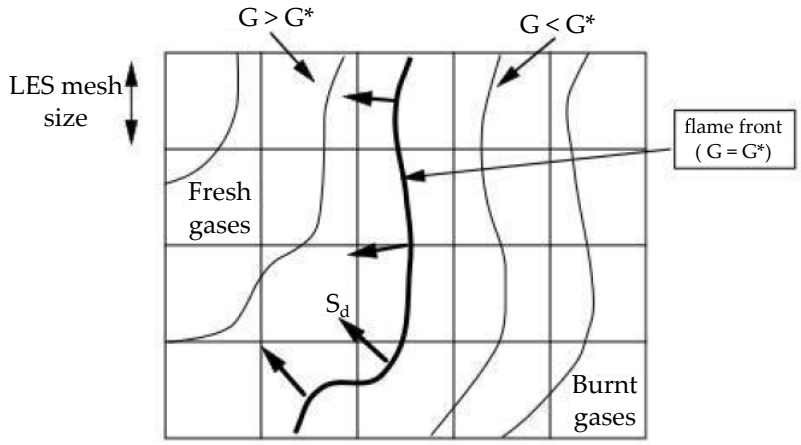

Figure 3.4: G-equation model from [31]. The flame front (represented by the dark curve) is associated with $\widetilde{G}$=G^*. The figure also shows the G field and what it looks like on either side of the flame front.

This method is based on an approach which is opposite to the thickened flame model. It assumes the flame thickness to be very thin and describes it with an iso-level G^*. This is seen in Figure 3.4, where the flame front is thinner compared to the flame front from ATF Model (Figure 3.3). The flame separates the burnt and unburnt sections which are represented with the field $\widetilde{G}$.

The burnt gases have $G < G^*$ and the fresh gases have $G > G^*$. The field $\widetilde{G}$ is obtained by solving the following equation:

$$\frac{\partial \overline{\rho}\widetilde{G}}{\partial t} + \frac{\partial \overline{\rho}\widetilde{u_i}\widetilde{G}}{\partial x_i} = \rho_0 \overline{S_t} \nabla |\overline{G}| \tag{3.42}$$

Where turbulent flame speed S_t is obtained using a correlation or a model [58].

The three models (Eddy Breakup, ATF and G-Equation) discussed in this subsection have their advantages and drawbacks. The Eddy Break-up Model is simple compared to ATF and G-Equation but it assumes very fast chemistry and the constant C_{EBU} also depends on various parameters [31].

The G-Equation model also has its own drawbacks. In Equation 3.42, a turbulent flame speed S_t is required which is found using a flame speed correlation or a model. Therefore it lacks universality. Also, it is known to exhibit numerical instabilities [58] which will require the use of an artificial diffusion scheme.

The ATF model is widespread in the literature and allows the flame front to be resolved on an LES mesh. It is however limited by the use of an efficiency function [58] which is required to retrieve the proper turbulence-flame interactions.

4

Modelling Approaches and Validation for Cold Flow Analysis

This chapter will include the description of the numerical modelling approaches used in Ansys Fluent. Section 4.1 will present the geometry of the trapped vortex burner and describe the model settings used in Fluent for the RANS and LES models. The boundary conditions, including the specification of the turbulent inlet for LES simulations, will be explained in Section 4.2. Section 4.3 will justify the choice of mesh used for the cold flow (non-reactive) simulations. Finally, Section 4.4 will show validation results consisting of comparisons of velocity profiles with PIV data obtained in the lab, and also comparisons with previous numerical work done by Gruber et al. [30].

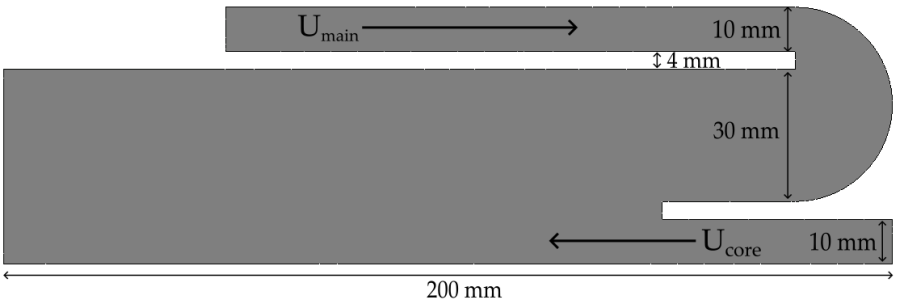

Figure 4.1: Side view of the trapped vortex burner with dimensions

4.1. Model Setup

The side, front and isometric views of the geometry used in this work are shown in Figures 4.1, 4.2 and 1.11. This two-dimensional design helps in simplifying the physics in the spanwise

direction, effectively making it a two-dimensional version of the FlameSheet™ burner. Gruber et al. [30] used a similar computational domain for their reactive and non-reactive LES simulations but have scaled down their channel heights by half (scaled down dimensions H1 and H2 by a factor of 2 in Figure 5.3). The same geometry is also studied experimentally with PIV at TU Delft's Combustion Lab in the Process and Energy Department.

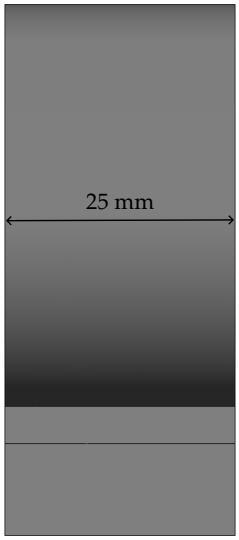

Figure 4.2: Front view of the burner geometry with the span wise width

In Figure 4.1, the inlet for the main stage is represented by U_{main} and the inlet for the core flow is represented by U_{core}. The main stage also features the 180-degree (U bend) bend around a tip (inner liner tip). Such a design helps disrupt the turbulent boundary layer in the main stage, by creating a trapped vortex (or a recirculation zone), which makes it more resistant to boundary layer flashback.

For cold flow simulations, the equivalence ratio of the incoming mixture is fixed at zero (only air). The experimental data which which will be used for validation is also collected for a mixture with $\phi = 0$ (only air). The target bulk velocities U_{main} and U_{core} are kept at 10.2 m/s to ensure the Reynolds number of the flow is 7000. Similar to the experimental setup, the air was supplied at a temperature of 298 K and atmospheric pressure.

For this work, Ansys Fluent, which is a commercial CFD software [61], is used. It uses finite volume method (FVM) to discretize the governing equations of fluid flow and has various RANS and LES models available.

The RANS simulation is performed using the realizable $k-\epsilon$ model in Fluent. For the pressure-velocity coupling, the Coupled algorithm is used.

For the LES simulation, the wall adapting local eddy-viscosity (WALE) model is used. The

SIMPLE algorithm [62] is used to solve the pressure-velocity coupling. The CFL based, adaptive time step option was used in Fluent and the maximum CFL number (Equation 4.1) was kept below 1. This restriction ensures that the fluid particle does not cover more than one grid cell in a single time step, allowing stable simulations [62]. Table 4.1 compares some of the computational options selected in Fluent for both RANS and LES models.

$$C = \frac{u\Delta t}{\Delta x} \tag{4.1}$$

	RANS	LES
Turbulence model	Realizable $k-\epsilon$	LES with WALE
Solver Type	Pressure - based	Pressure - based
Time	Steady	Transient
Pressure - Velocity Coupling	Coupled	SIMPLE
Gradient Discretization	Least Squares Cell Based	Least Squares Cell Based
Momentum Discretization	Second order Upwind	Bounded Central Differencing
Initialization	Hybrid Initialization	RANS Solution

Table 4.1: Table comparing some of the computational settings used in Fluent for RANS and LES

4.2. Boundary and Initial Conditions

4.2.1. Precursor Simulation

In order to obtain a fully developed turbulent flow in the U-bend region, the experimental setup has a long inlet (about 1 m in length). Simulating turbulent flow inside such a long channel together with the burner domain shown in Figure 4.1 would utilize a lot of computational resources. Lund et al. [63] proposed an approach in which a separate simulation is performed in parallel with the main simulation, using a domain created by extruding the inlet upstream by a short distance and applying periodic boundary conditions in the streamwise direction. The velocity profiles obtained in the auxiliary simulation are then introduced at the inlet of the main simulation. This makes it possible to obtain the inlet conditions using LES. However, such an approach is not easy to implement for all cases as it can be too expensive in terms of computer resources and effort [64]. To overcome this, several approaches have been proposed which generate fluctuating turbulence at the inlet using mean quantities [65].

In Fluent, Spectral Synthesizer is a method to generate fluctuating velocity components at the inlet for an LES simulation [66]. It is based on a random flow generation method described by Smirnov et al. [67]. To use this algorithm, realistic velocity (u), turbulent kinetic energy (k) and turbulent dissipation rate (ϵ) profiles must be provided at the inlet using a separate RANS simulation. For this work, a precursor simulation of a turbulent channel flow using RANS which has the same bulk inlet velocity as U_{main} (10.2 m/s for this cold flow case) is performed. Fig-

ure 4.3 shows the velocity profile obtained from such a precursor simulation. This profile is then given as an input to the spectral synthesizer algorithm in Fluent to generate turbulent fluctuations at the inlet for the LES simulation. These inlet profiles can also be used as inputs for the RANS simulation.

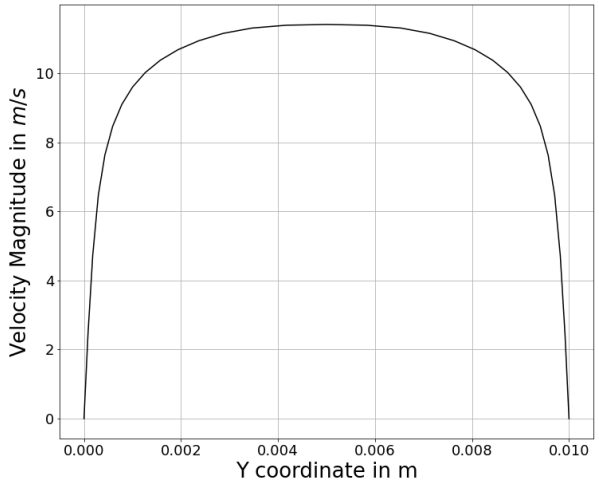

(a) Velocity magnitude

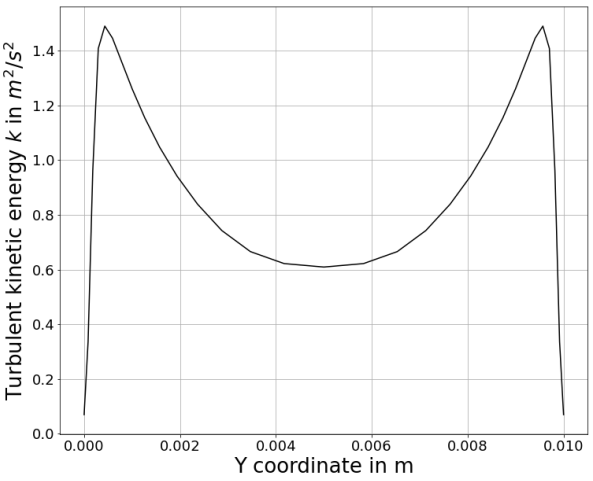

(b) Turbulent kinetic energy

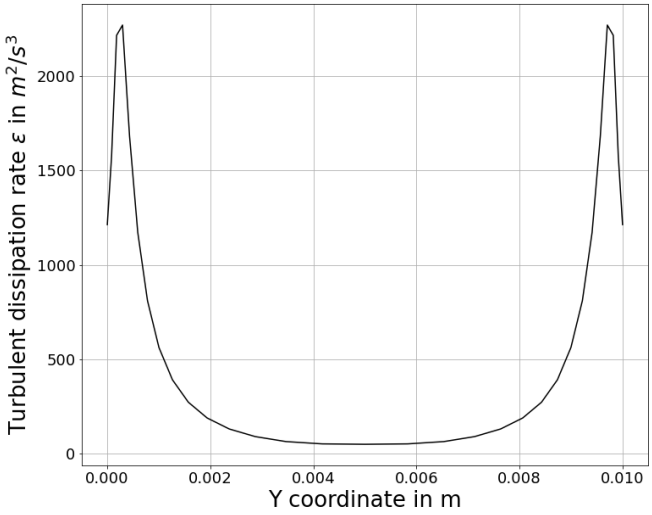

(c) Turbulent dissipation rate

Figure 4.3: Profiles provided as an input for the spectral synthesizer algorithm in Fluent. The algorithm uses this velocity profile along with the turbulent kinetic energy and dissipation rate profiles to add fluctuating turbulent profiles at the inlet of the domain

The precursor simulation was run using the realizable $k-\epsilon$ model which needed 16 CPU cores and required 6 CPU hours to reach convergence. The mesh was a wall-modeled mesh having 1 million cells.

4.2.2. Boundary Conditions for RANS

For the RANS simulation, the main and core inlets are defined as velocity inlets by providing the velocity profiles obtained using the precursor simulation (Figure 4.3). Along with velocity, k and ϵ profiles are also provided to calculate the turbulence parameters. By following this, the bulk velocity at both inlets is maintained at 10.2 m/s, giving an Re value of 7000.

The exit is defined using an Outflow boundary condition and periodic boundary conditions are imposed in the spanwise direction. All the walls in the geometry are assumed to be no-slip and maintained at room temperature (298 K).

4.2.3. Boundary Conditions for LES

At the main inlet, Spectral Synthesizer algorithm was used to add turbulence at the inlet. To use the algorithm, the profiles shown in Figure 4.3, obtained from the precursor simulation, were used as inputs. This ensures that the bulk velocity is maintained at 10.2 m/s.

At the core flow inlet, the same inlet conditions are imposed with U_{core} having a bulk velocity of 10.2 m/s. Outflow boundary condition is imposed at the exit and a periodic boundary condition is imposed in the span-wise (or z direction) direction. All walls are assumed to be no-slip and maintained at room temperature (293 K).

For the initial condition, a RANS simulation using realizable k-ϵ model in Fluent is used to obtain the initial velocity field inside the burner. Once the simulation has converged, the averaged velocity field is taken as the initial condition for the LES simulation. When the flow is fully developed with LES, data sampling is initiated.

4.3. Mesh Analysis

Fluent's meshing tool is used to generate an unstructured mesh with polyhedral cells (shown in Figure 4.4). A uniform boundary layer mesh with 10 layers was also added adjacent to the walls in order to capture the near wall turbulent flow features (Figures 4.5 and 4.6). Since we are not using any wall function, the average y+ value was maintained around 0.9 for the cells adjacent to the wall boundaries to ensure the near wall structures are sufficiently resolved.

In LES, it is necessary to ensure that the computational mesh is fine enough to capture the necessary details of the turbulent flow while avoiding excessive use of computational resources (CPU cores). This balance ensures that enough simulations, including those with modified geometrical features, can be performed within the time constraints of this research work. In order to come up with such an optimum mesh, the following three meshes were made and analyzed:

- Mesh M1: This is a highly resolved mesh with approximately 2.8 million cells. The cells

were kept very fine (a constraint of 0.3 mm) throughout the U-bend region.

- Mesh M2: This mesh contains less than 1 million cells. It has coarser cells (0.6 mm constraint) in the U-bend.
- Mesh M3: Containing only 1.1 million cells, this mesh has lesser cells than M1 but still contains fine cells (0.4 mm constraint) in the region around the inner liner tip.

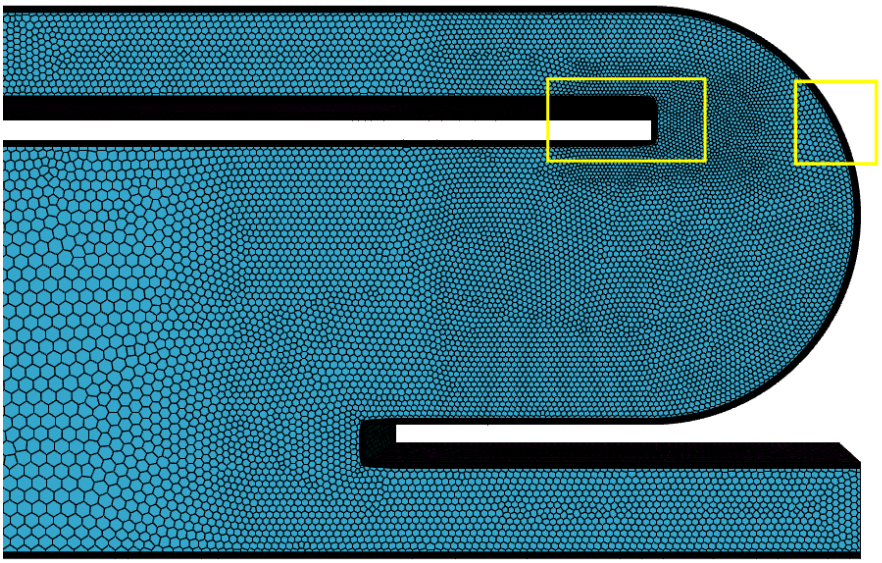

Figure 4.4: Unstructured mesh generated on Ansys Fluent. The yellow boxes show the areas magnified in Figures 4.5 and 4.6 to show the boundary layer mesh added adjacent to the walls

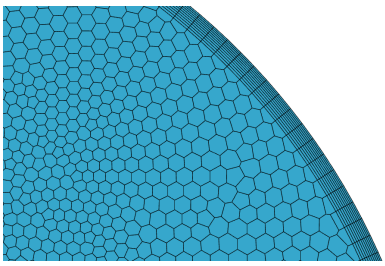

Figure 4.5: Cells adjacent to the outer wall in the U bend region

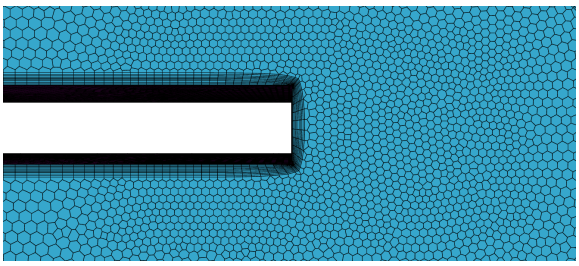

Figure 4.6: Cells around the inner liner tip of the burner

Figures 4.7a, 4.7b and 4.7c show the normal velocity profiles obtained along curves A, B and C (see Figure 4.8) using the three meshes. From these plots, qualitatively, we can see that there isn't a big difference between meshes M2 and M3. With M1, we can see slightly different profile close to the inner liner tip (between normalized distances 0.0 and 0.4). This difference maybe because of the different averaging times. Mesh M1 was averaged for 0.05s while meshes M2 and M3 were averaged for 0.2s. A huge difference in computational time was observed while running simulations with these meshes. Meshes M2 and M3 were using 18 and 20 CPU cores respectively and required around 4300 CPU hours to run 0.2 seconds of turbulent flow in the burner which was sufficient to reach a statistically steady state. Mesh

M1 on the other hand, required 28 CPU cores and 8000 CPU hours to run 0.05 seconds, making it more expensive than M2 and M3. Given the time constraints at play for this work and our ultimate goal of running multiple LES with different geometry modifications, mesh M1 was discarded for further analysis.

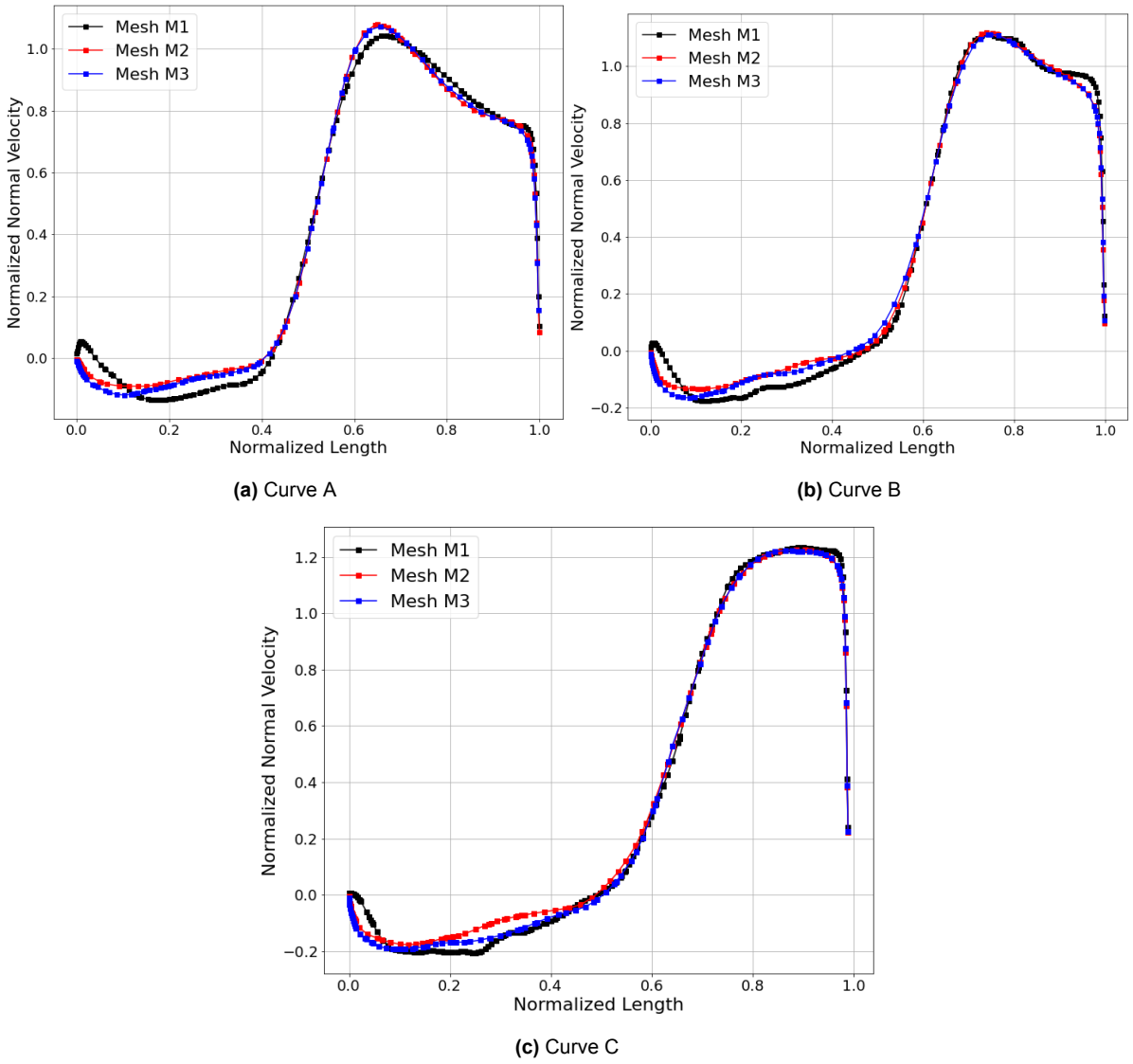

(a) Curve A

(b) Curve B

(c) Curve C

Figure 4.7: Comparison of normal velocity profiles along curves A, B and C (Refer to Figure 4.8 for curve locations) from LES using the three meshes M1, M2 and M3

Between the remaining two meshes, M3 was selected for future investigations since it has finer cells in the region around the inner liner tip, compared to M2. This area is one of the main regions of interest in our work and a finer mesh would allow us to resolve the turbulent structures more accurately.

4.4. Validation of the methodology

From the Combustion Lab at TU Delft's Process and Energy Department, velocity data for the curves shown in Figure 4.8 inside the main stage of the burner is available. This information can be used to validate both our RANS and LES simulation setups used for cold flow analysis. This is important as it ensures that our choice of options to simulate cold flow is adapted and can accurately capture the turbulent flow inside the burner.

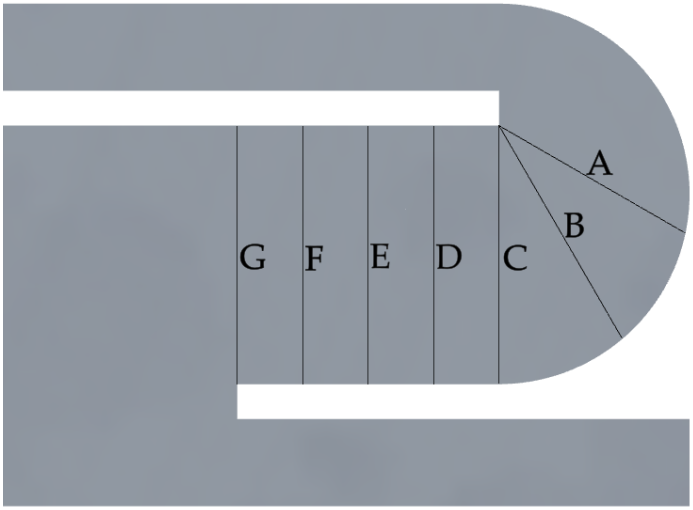

Figure 4.8: Profiles (named A to G) along which normal velocities, obtained using PIV, are available for validation

4.4.1. Validation of the RANS Model

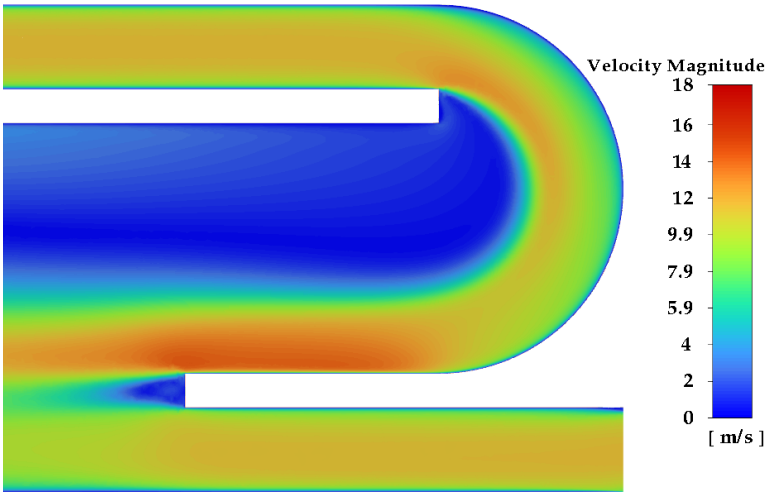

Figure 4.9: Velocity magnitude contours obtained using RANS. The contours are drawn on a plane created in the domain's midsection in the span-wise direction.

The RANS model used in this work serves two purposes. Firstly, the solution obtained from this model is used as the initial condition for the LES simulation. And secondly, because of its inexpensive computational cost, RANS computations can be used to perform quick cold flow simulations with different geometrical modifications. From these RANS results, general tendencies can be observed and a few interesting cases can be selected for additional analysis with LES. The RANS simulation was run using 20 cores, requiring a total of 15 CPU hours (which is the total simulation time times the number of CPU cores used) and 353 iterations.

Figure 4.9 shows the velocity magnitude contours obtained using RANS. Figure 4.10 is a streamline plot, coloured with velocity magnitude values. Both figures clearly shows the presence of a recirculation zone in the main stage. Such a structure helps in stabilizing the flame and making the burner more resistant to flashback as it disrupts the turbulent boundary layer close to the inner liner tip.

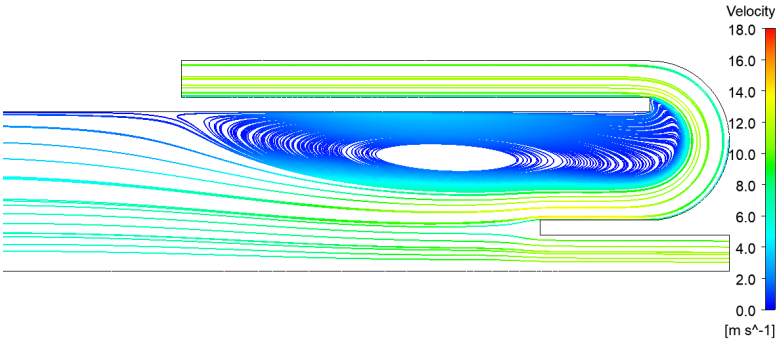

Figure 4.10: Velocity magnitude streamlines obtained using RANS. The streamlines are drawn on the same plane used in Figure 4.9

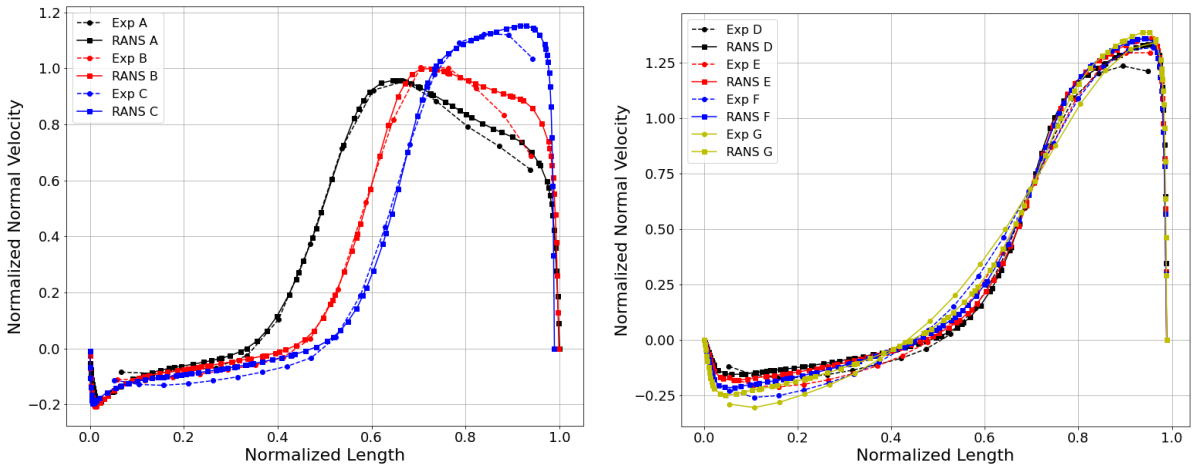

(a) Along curves A, B and C

(b) Along curves D, E, F and G

Figure 4.11: Comparison of normal velocity profiles from RANS with PIV data

The validation results are shown in Figures 4.11a and 4.11b. In these plots, the normal velocity along the curves shown in Figure 4.8 are non-dimensionalized using the bulk velocity (10.2 m/s). The first and the last point in the PIV data is discarded due to inaccuracies in measuring

values close to the wall. From these results, we can see that our RANS model is quite accurate and can be used as an appropriate initial solution for LES. This allows us to extend our model to perform RANS simulations with modified burner geometries (which will be shown in Chapter 5).

4.4.2. Validation of the LES Model

Now that an appropriate mesh has been selected (M3), validation of our LES model can be done by comparing the velocity data with the PIV measured velocities along the curves shown in Figure 4.8.

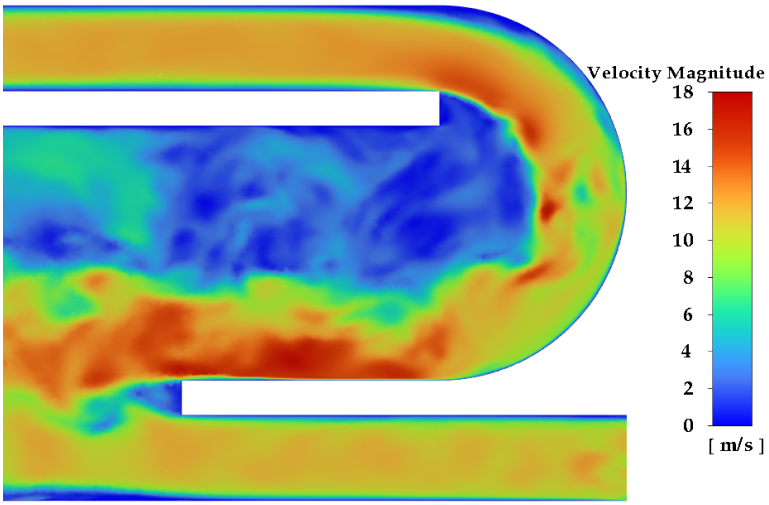

Figure 4.12: Velocity magnitude contours obtained using LES. The contours are drawn on a plane created in the domain's midsection in the span-wise direction.

Figure 4.12 shows a contour of the instantaneous velocity magnitude inside the burner, taken after a statistically steady state has been reached. Clearly, from these LES simulations, more information can be gained about the turbulent flow inside the U-bend when compared to a RANS simulation. Certain structures like vortex shedding in front of the inner liner tip, flow separation from the outer bend as the flow is inverted in the bend may play a role in flame flash-back. Chapter 6 will contain a more thorough discussion about such features. The present objective of this chapter is to simply validate the model against experimental data.

The validation results are shown in Figures 4.13a and 4.13b. The normal velocities are non-dimensionalized using the bulk velocity (10.2 m/s). Figure 4.13a shows the results for the curves A, B and C which are located in the bend region while Figure 4.13b contains the curves further downstream in the main channel. All the profiles show a slightly higher peak velocity than the PIV data, close to the outer wall of the bend. Apart from this difference the LES simulations show a good agreement with the PIV velocity profiles and the model can be used for other LES cold flow simulations.

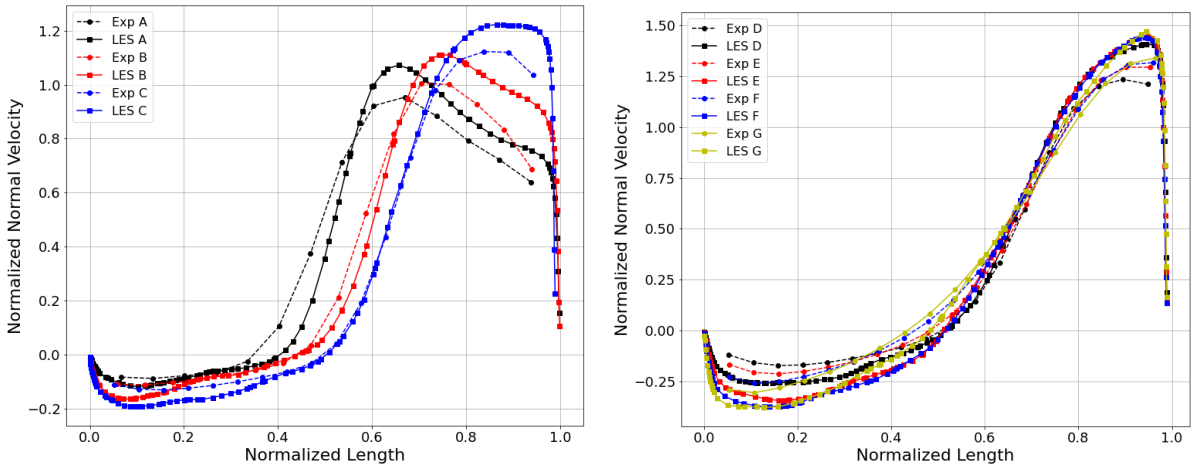

(a) Along curves A, B and C

(b) Along curves D, E, F and G

Figure 4.13: Comparison of normal velocity profiles from LES (with Mesh M3) with PIV data

4.4.3. Comparison with Previous Numerical Work

	Our work	Gruber et al. [30]
CFD Solver	Fluent	OpenFOAM
Turbulence model	LES with WALE	LES with dynamic K equation
Pressure - Velocity Coupling	SIMPLE	PIMPLE
Re	7000	3500
Velocity inlet	Spectral Synthesizer	Synthetic Eddy Method
Mesh size	1.1 million	60 million
Initialization Method	RANS	Unsteady RANS

Table 4.2: Table comparing Gruber et al.'s model setup [30] with our work

In this subsection, a comparison with previous numerical work done on the FlameSheet™ burner by Gruber et al. [30] is shown. From our literature review, this was the only numerical work done on such a burner which was available. For their non-reactive simulation, a similar computational domain was used but with channel dimensions scaled down by a factor of 2. This would mean that their Reynolds number is 3500 instead of 7000 at the inlet, since the channel height at the inlet is reduced by half. Table 4.2 compares their model setup with our Fluent LES model. Using slightly different inlet bulk velocity compared to the experiments, Gruber et al. [30] have a higher peak velocity value compared to the PIV data but still show satisfactory agreement and are able to predict the general flow patterns and position of the peak velocity regions quite well. The over-prediction of their peak velocity value and also the difference we see in the middle of the domain might be because of the reduced channel height.

Figures 4.14a, 4.14b and 4.14c show how our LES results compare with PIV values and also with the LES simulations performed by Gruber et al. [30]. From these curves, we can see that

our current LES results are much closer to the experimental results than the previous numerical simulations and this is probably because the exact domain dimensions were used in our work.

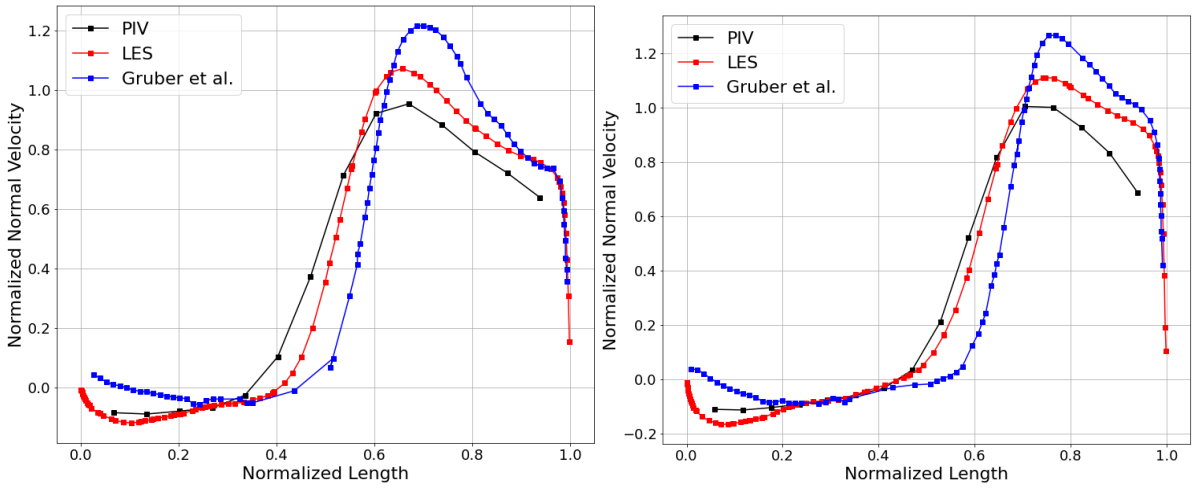

(a) Curve A

(b) Curve B

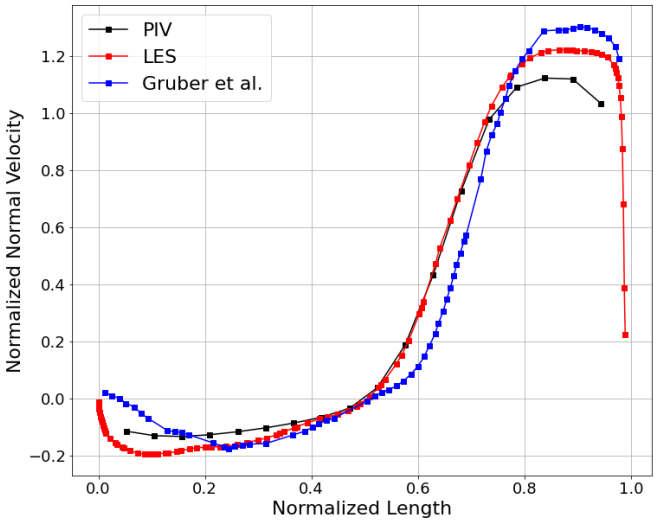

(c) Curve C

Figure 4.14: Comparison of normal velocity profile along curves A, B and C with Gruber et al. [30] and PIV values

5

Parameter Study with RANS

In the previous chapter, the validation of the RANS and LES models was discussed, which showed good agreement with experimental results. With this, we have a model which can be used to analyze the main features of the turbulent flow inside the trapped vortex burner. Using a similar mesh and setup in Fluent, numerical simulations can be performed on modified versions of the burner's geometry. This chapter will describe the various parameters considered for cold flow analysis and also show the results obtained from the simulations, which were performed using RANS. RANS was selected because of its affordable computational cost, which will help when running several cases and enable to perform a preliminary analysis with the results.

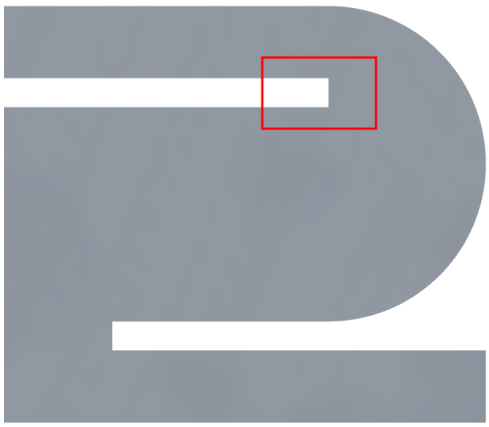

Figure 5.1: Geometry of the trapped vortex burner with the blunt shaped tip. The red box shows the focus location which will be studied with the first parameter.

5.1. Geometrical Parameters

In this work, three geometrical features were selected for analysis. The first feature was the shape of the inner liner tip which is shown in Figure 5.1. This feature was also studied by Gruber et al. [30], they have investigated two shapes: blunt and sharp tip (see Fig. 5.2c). For our work the following tip shapes have been considered which are also shown in Figure 5.2:

- **T1** - Blunt: This shape, which has already been simulated will be the base case with which comparisons will be made.
- **T2** - Semi-circular: The blunt faces are replaced with a semi-circular arc having a diameter of 4 mm, same as the thickness of the liner tip (Figure 5.2a).
- **T3** - Quarter-circular: Similar to T2 but with a quarter-circular arc having a radius of 4mm (Figure 5.2b).
- **T4** - Sharp tip with a flat top: The top surface of this tip makes a 30° angle with the horizontal (Figure 5.2c).
- **T5** - Sharp tip with a curved top: Similar to T4 but the flat top is replaced with a smooth curved surface whose tangent on the lower end makes a 30° angle with the horizontal (Figure 5.2d).

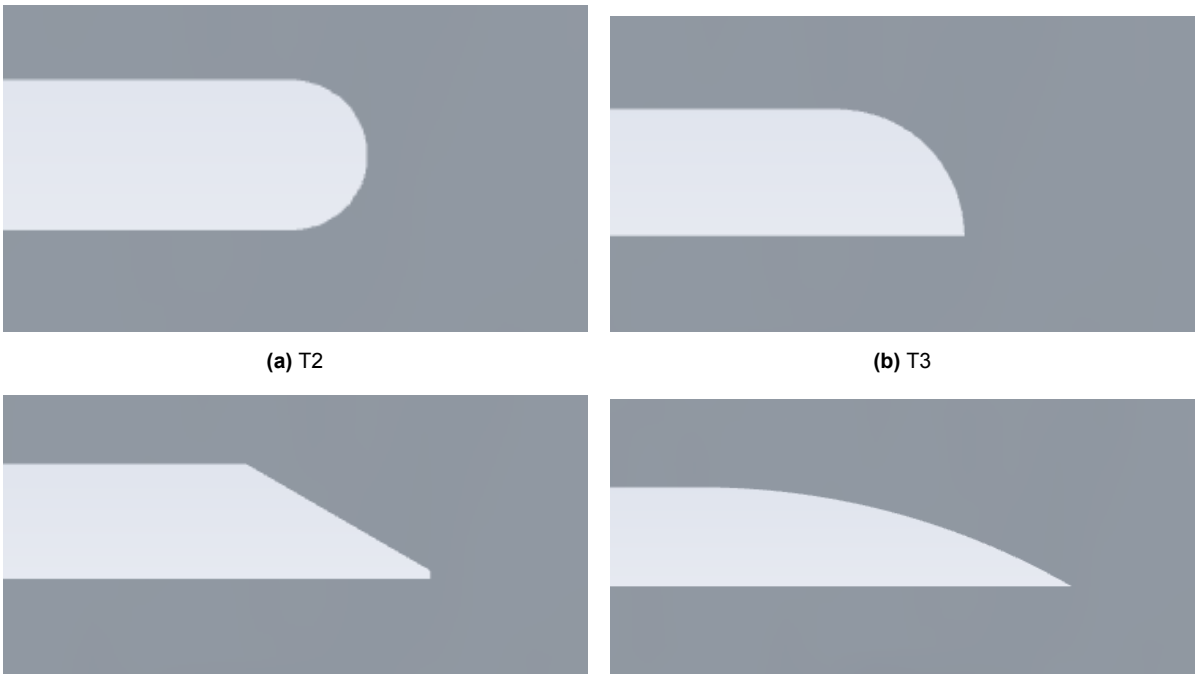

(a) T2 **(b)** T3

(c) T4 **(d)** T5

Figure 5.2: Different tip shapes studied in this work using RANS

Figure 5.3 shows the second feature which was considered. Dimension H1 represents the height of the channel upstream of the bend. The value of H1 for the base case is 10 mm. H2 represents the height of the channel downstream of the bend and it is 30 mm in length for the base case. The ratio of these dimensions (H2/H1) is another parameter which was considered

by Gruber et al. [30]. By reducing the ratio to 2 (base case has a ratio 3), the velocity in the downstream channel was increased which would help in pushing back the flame and thus, making it more flashback resistant.

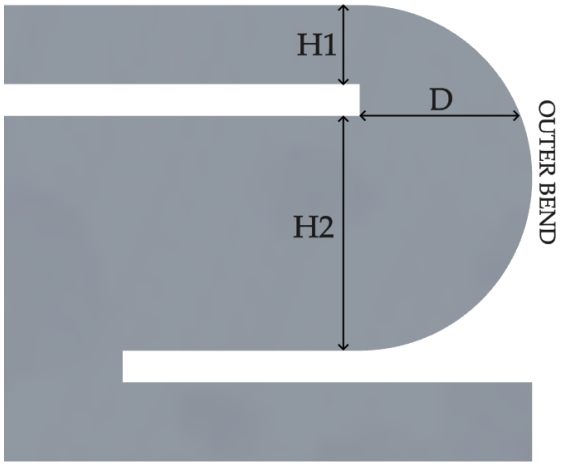

Figure 5.3: Burner geometry with dimensions H1, H2 and D shown. H1 represents the height of the main channel inlet and H2 represents the height of the channel downstream. D represents the distance between the inner liner tip and the outer bend of the burner

The third parameter is the distance between the end of the inner liner tip and the outer bend (denoted by D in Figure 5.3). This distance is 20 mm in the base case. Since the flow separates from the outer wall as it enters the U bend, a lesser D length would help in reducing the size of this separation layer. This would make it harder for the flame to propagate upstream through this layer. The D length was reduced by 5 mm and studied with the various tip shapes. Figure 5.4 summarizes the features discussed with a matrix in which each white box represents a simulated case and the modified parameters are given by the row and column names.

	H2/H1 = 3 D = 20 mm	H2/H1 = 2 D = 20 mm	H2/H1 = 3 D = 15 mm
T1			
T2			
T3			
T4			
T5			

Figure 5.4: Matrix showing the 15 cases designed by varying the three parameters: tip shape, H2/H1 ratio, and length D. Each white box in the matrix represents a modified case which was simulated with RANS

5.2. Analysis with different liner tip shapes

In this section, the simulations with different tip shapes will be discussed (first row in Tab. 5.4). These cases have the same H2/H1 ratio (H2/H1 = 3) and distance D (20 mm) as the base case. These simulations were all run using 20 CPU cores and required around 15 CPU hours.

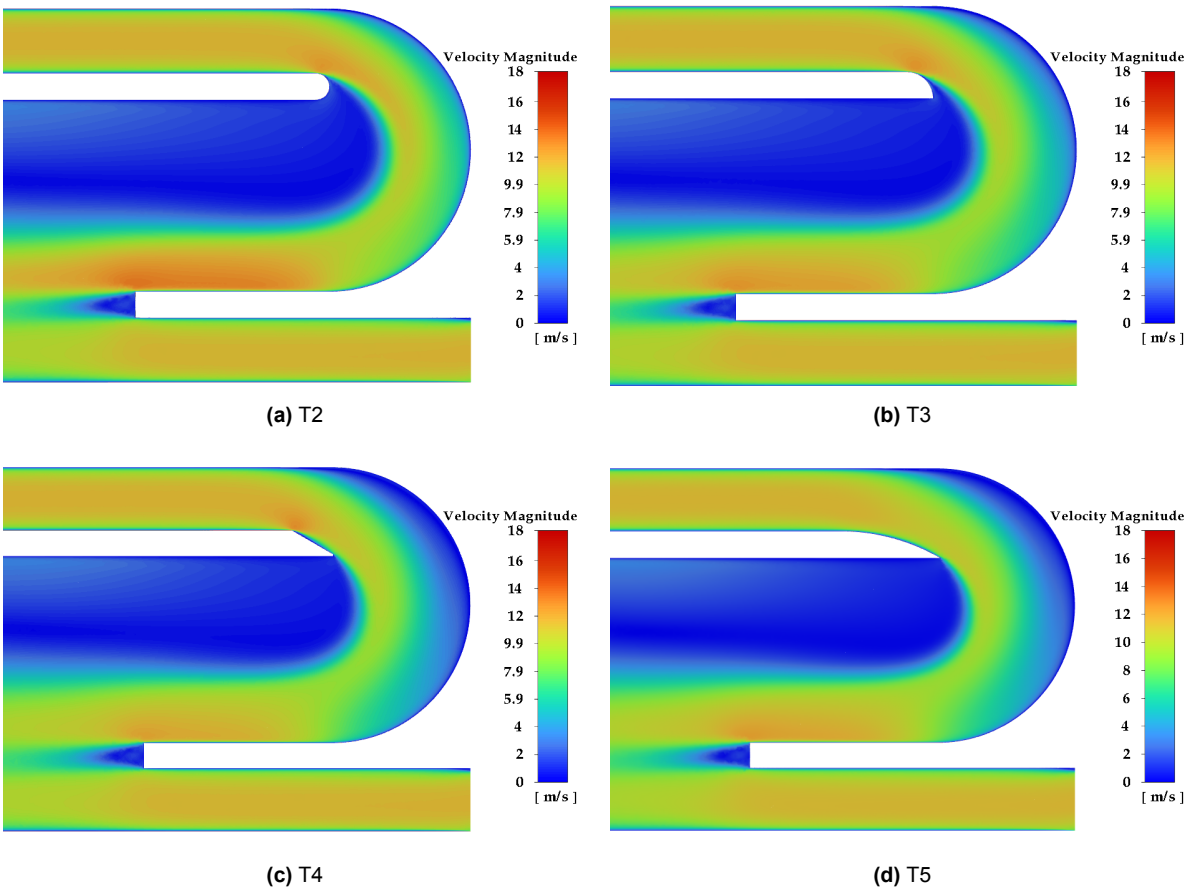

(a) T2 **(b)** T3

(c) T4 **(d)** T5

Figure 5.5: Velocity magnitude contours for tips T2, T3, T4 and T5 with H2/H1 = 3 and D = 20mm

Figure 5.5 shows the velocity contour plots obtained. On comparing these contours qualitatively with the base case (Figure 4.9), we observe similar flow patterns with tips T2 and T3. The flow separates from the upper edge of the circular arc shaped tip and follows the shape of the outer bend before entering the downstream channel (channel with height H2). Tips T4 and T5 also follow a similar pattern but we can clearly see a low velocity layer adjacent to the outer bend in the contour plots (Figures 5.5c and 5.5d). The presence of such a low velocity layer can act as a low resistance path for the hydrogen flame to propagate upstream, leading to flashback.

The velocity profiles along curves A and C (from Figure 4.8) are shown in Figure 5.6. These profiles clearly highlight differences in normal velocity fields between different tips. Tips T1, T2 and T3 show similar trends in their velocity profiles and T4 and T5 seem to behave differently, especially in the region close to the tip. Tip T1, the base case has the highest peak velocity

in the layers adjacent to the outer bend for both location. Sharper tips T4 and T5, exhibit the lowest peak velocity among the different tip shapes. However, in Figure 5.6a, the sharp tips have a higher velocity profile close to the inner liner tip, since the flow seems to follow the liner tip shape more closely compared to the other cases. The other tips (T1, T2 and T3) show a lower velocity profile in this region (even becoming negative) since the flow separates from the liner tip at a more upstream position compared to the sharp tips.

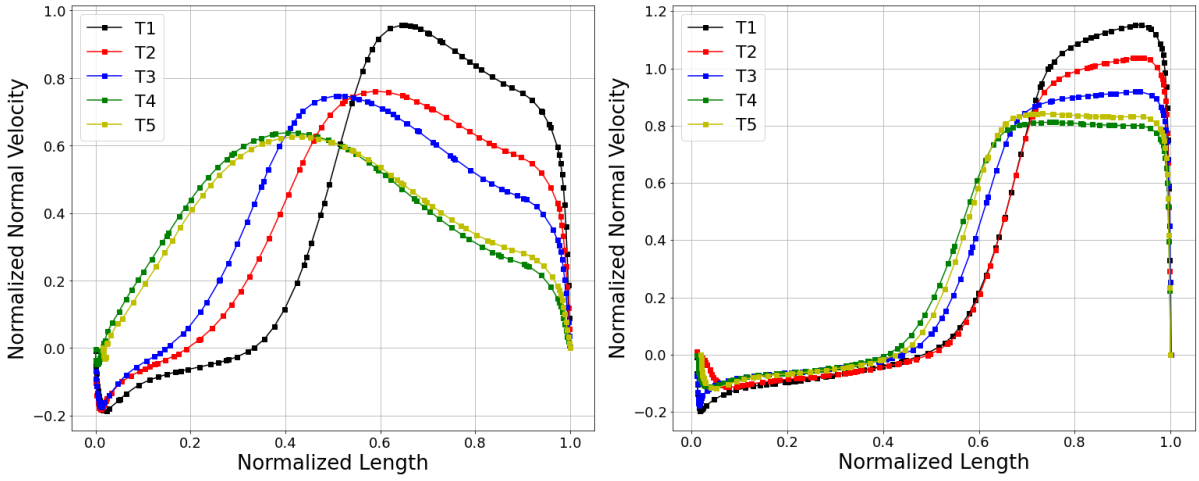

(a) Along curve A

(b) Along curve C

Figure 5.6: Normal velocity profiles along curves A and C with different liner tip shapes

5.3. Analysis with H2/H1 = 2

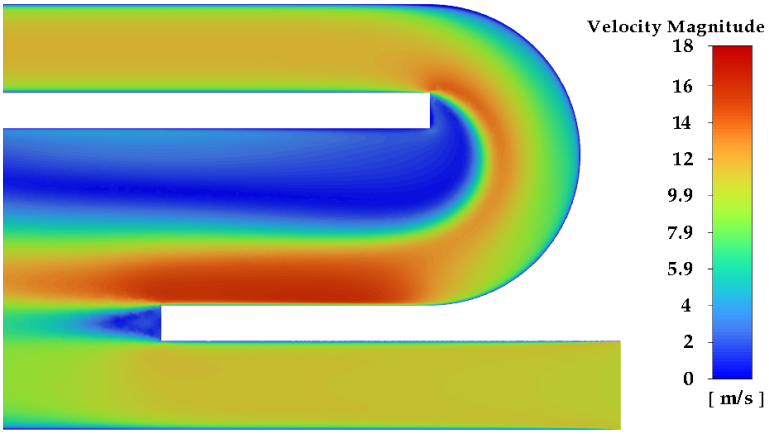

Figure 5.7: Velocity magnitude contour for tip T1 with H2/H1 = 2 and D = 20 mm

In the previous section, we discussed the importance of the velocity layer adjacent to the outer bend in preventing flame flashback. Using the continuity equation, we know that the velocity profile through a channel can be increased by decreasing the height of the channel. Gruber et al. [30] reduced the ratio H2/H1 to 2 and found that the burner, with a sharp liner tip and a

preheated hydrogen-air mixture, was more resistant to flame flashback. This was because of the increased resistance offered by the increased flow velocity. In our work, a similar cold flow analysis was performed with H2/H1 = 2 for the various tips, and distance D having a value of 20 mm (same as the base case).

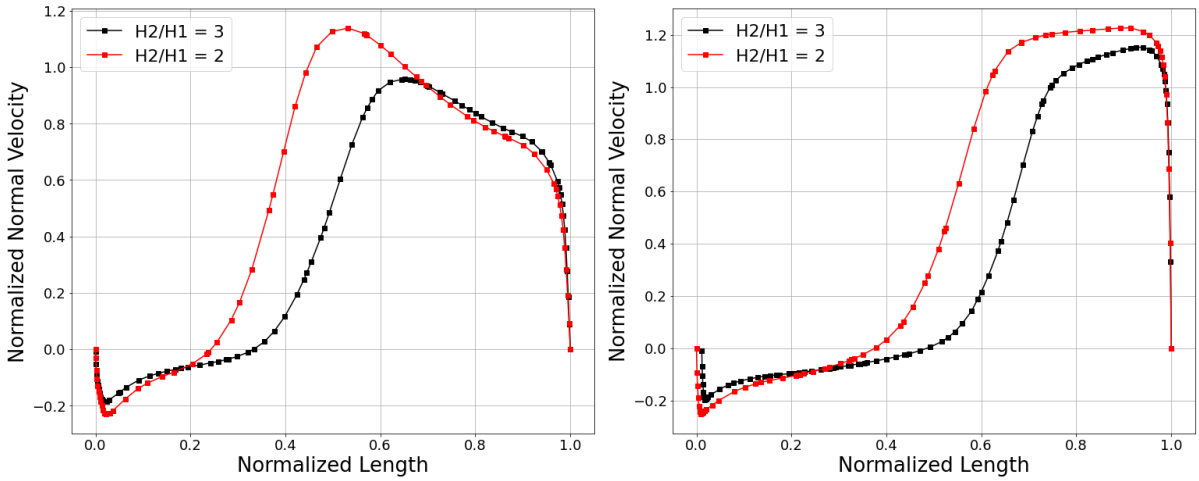

(a) Along curve A

(b) Along curve C

Figure 5.8: Normal velocity profiles along curves A and C with tip T1 for different values of H2/H1

Figure 5.7 shows the velocity contours with H2/H1 = 2 and the base case tip shape (blunt). Qualitatively, we see the same features as for the base case, Figure 4.9 (H2/H1 = 3). However, on observing the velocity magnitudes, we can see a higher flow velocity close to the outer wall in the lower channel. Figure 5.8 also confirms this. From the non-dimensionalized lengths, we also see that the percentage of the curve having a high flow velocity is also increased which is useful in making a more flashback resistant burner.

The velocity contours for the different liner tips with H2/H1 ratio of 2 are shown in Figure 5.9. Similar to the analysis done with T1, we observe the same flow patterns with the other tips when compared with the contours obtained in Figure 5.5 (with H2/H1 = 3). We also see the increased flow velocity in the bend region, similar to Figure 5.7.

The normal velocity profiles along curves A and C are shown in Figure 5.10. Here we also compare the results with the profiles shown in Section 5.2 (H2/H1 = 3). The higher flow velocity especially in this bend region is an improvement since we know that this should help in reducing the flashback tendency of the hydrogen flame. Apart from the higher flow velocity, we notice that the sharp tips (T4 and T5) have velocity profiles which are now comparable with tips T2 and T3. From this, we can conclude that the ratio of the channel heights (H2/H1) is an important parameter in increasing the flashback resistance of the trapped vortex burner.

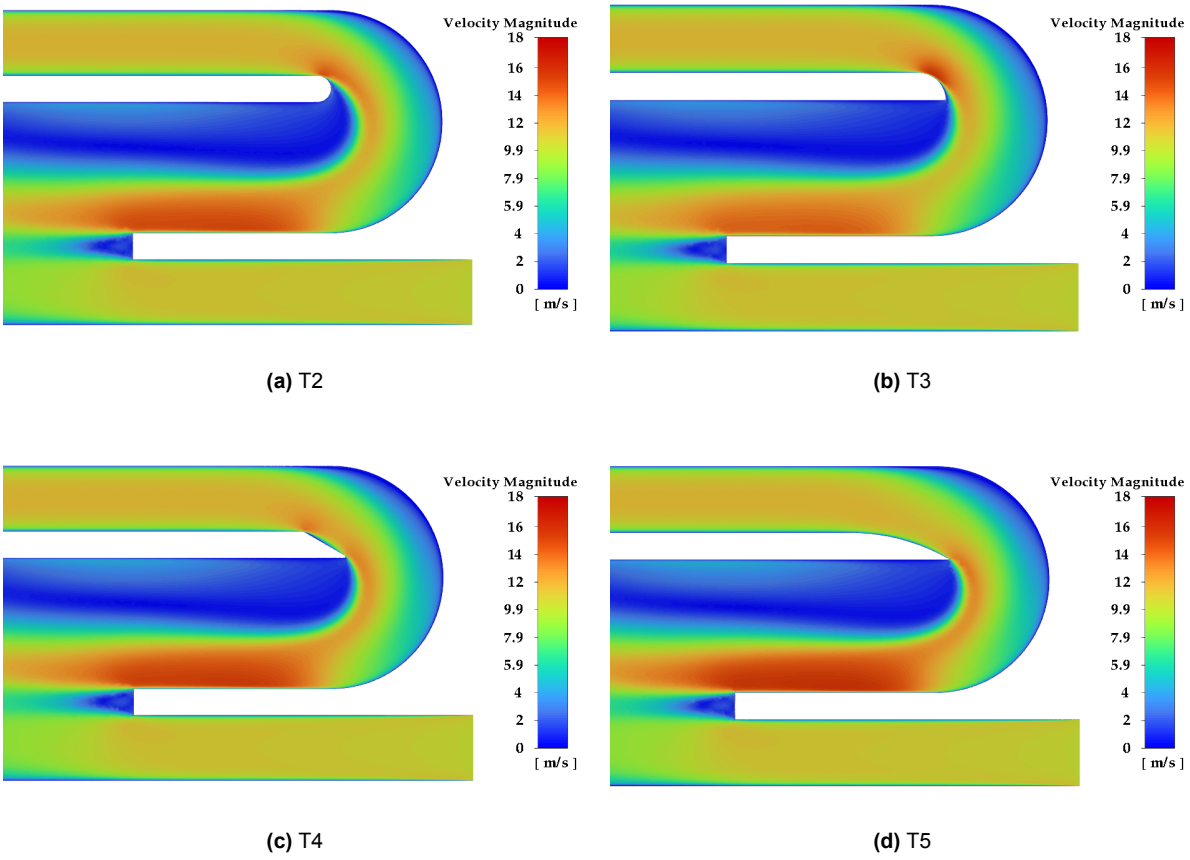

(a) T2 **(b)** T3

(c) T4 **(d)** T5

Figure 5.9: Velocity magnitude contours for tips T2, T3, T4 and T5 with H2/H1 = 2 and D = 20mm

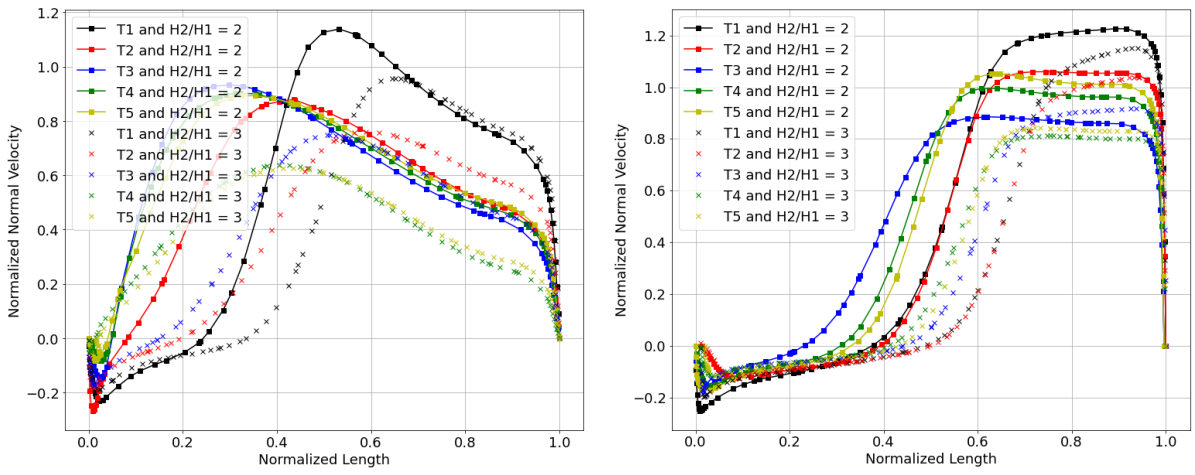

(a) Along curve A **(b)** Along curve C

Figure 5.10: Normal velocity profiles along curves A and C with different liner tip shapes and H2/H1 ratios

5.4. Analysis with D = 15 mm

From the previous two sections, we noticed a layer of low velocity adjacent to the outer bend in most of our simulations, especially the ones with the sharp tips (T4 and T5). By pushing the inner liner tip some distance inside the bend, it might be possible to reduce the size of this low velocity layer. In the base case, the liner tip is located at a distance of 20 mm horizontally from the outer bend. The geometries in this section have been modified by reducing this distance D to 15 mm. This change would cause the flow to 'stick closer' to the outer bend, making the velocity layer adjacent to the bend more flashback resistant due to the increased flow velocity in this region.

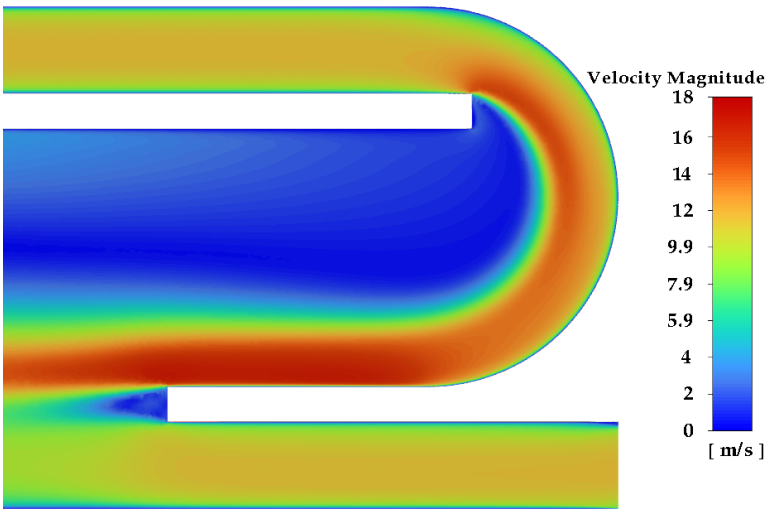

Figure 5.11: Velocity magnitude contour for tip T1 with H2/H1 = 3 and D = 15 mm

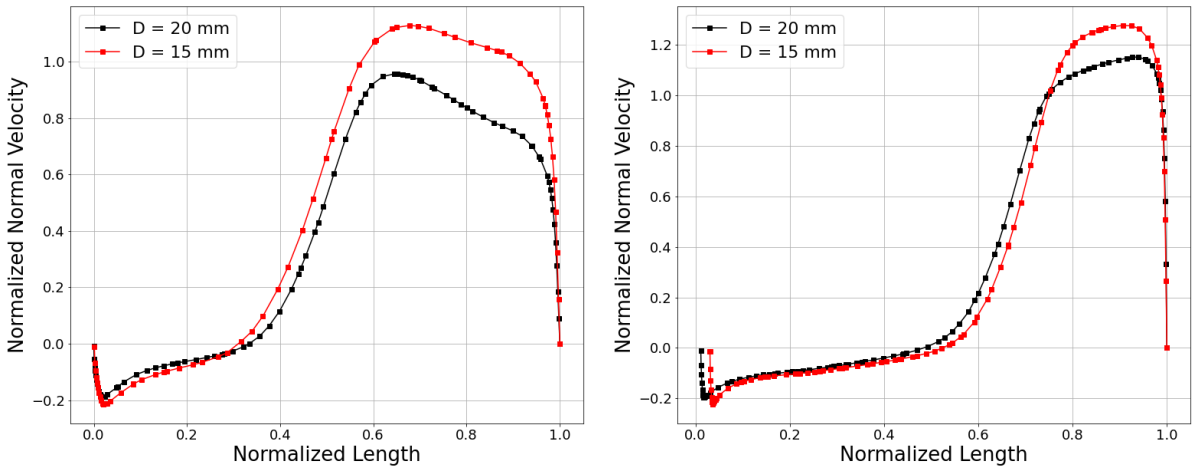

(a) Along curve A

(b) Along curve C

Figure 5.12: Normal velocity profiles along curves A and C with tip T1 for different values of D

Figure 5.11 shows the velocity contours when the base case was modified by reducing D to 15 mm. We observe the same flow pattern as the previous simulations with tip T1. But when

we look at the velocity profiles along the curves A and C (Figure 5.12), we notice that the flow velocity has increased close to the outer bend. This increase in velocity values close to the outer wall of the U-bend would 'improve' the boundary layer flow adjacent to the wall as it reduces the frequency of the low-velocity streaks in these layers. This might help in making the burner more flashback resistant.

The same change was done to the geometries used in Section 5.2, reducing D from 20 mm to 15 mm (last column in Tab. 5.4). Figure 5.13 has the velocity contour plots for all the other tips (T2, T3, T4 and T5). When we compare these contours with Figure 5.5, we notice that the low velocity region next to the outer bend has reduced in thickness.

The velocity profiles along curves A and C for the different tip shapes with D = 15 mm are shown in Figure 5.14. The data from Section 5.6 was also plotted for comparison. From Figure 5.14a, we can see that the velocity profile close to the tip at the A location remains almost the same while in the region close to the outer bend it has increased, showing an improvement. For curve C, we don't see a large difference in velocity values except for tips T1 and T2, which have very clearly increased.

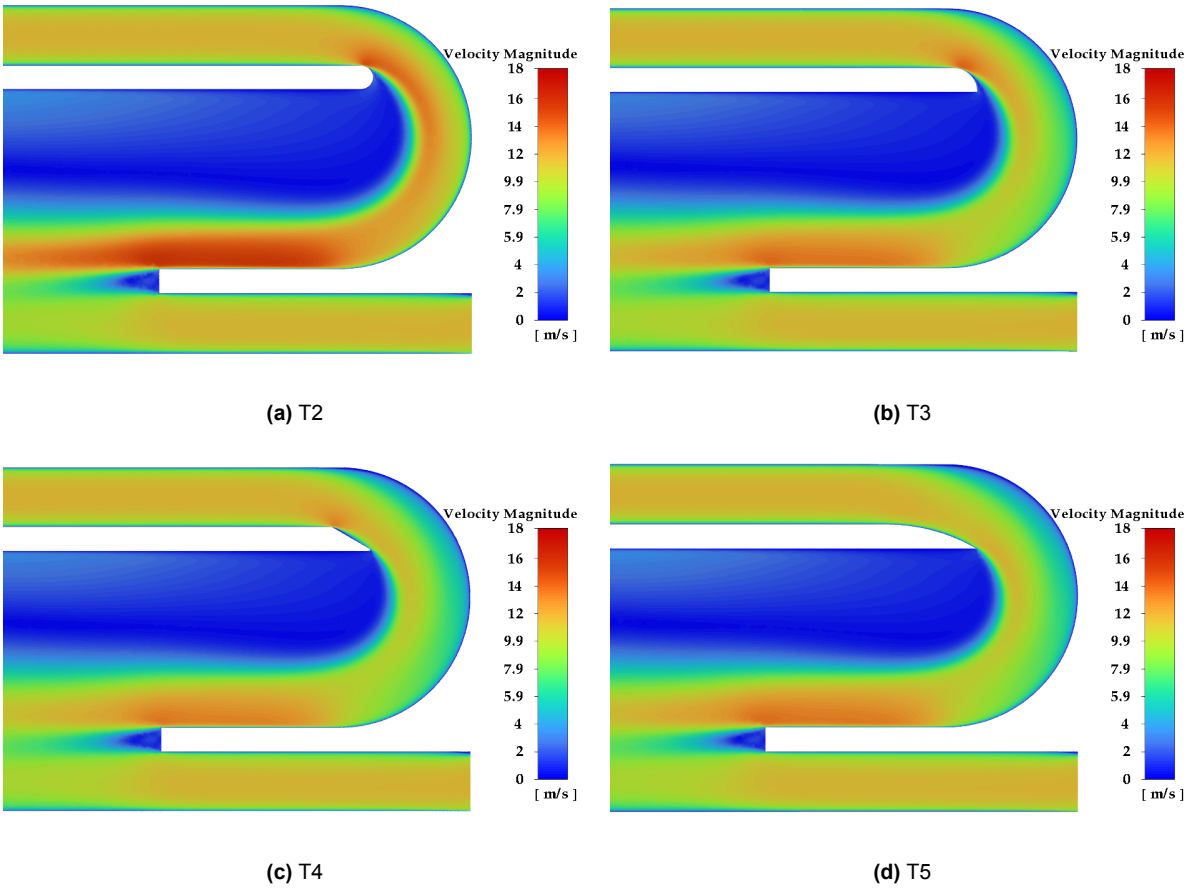

(a) T2 **(b)** T3

(c) T4 **(d)** T5

Figure 5.13: Velocity magnitude contours for tips T2, T3, T4 and T5 with H2/H1 = 3 and D = 15mm

These results show that the distance D between the inner liner tip and the outer wall of the

bend is another important parameter which can be considered while optimizing the shape of the trapped vortex burner to make it more flashback resistant.

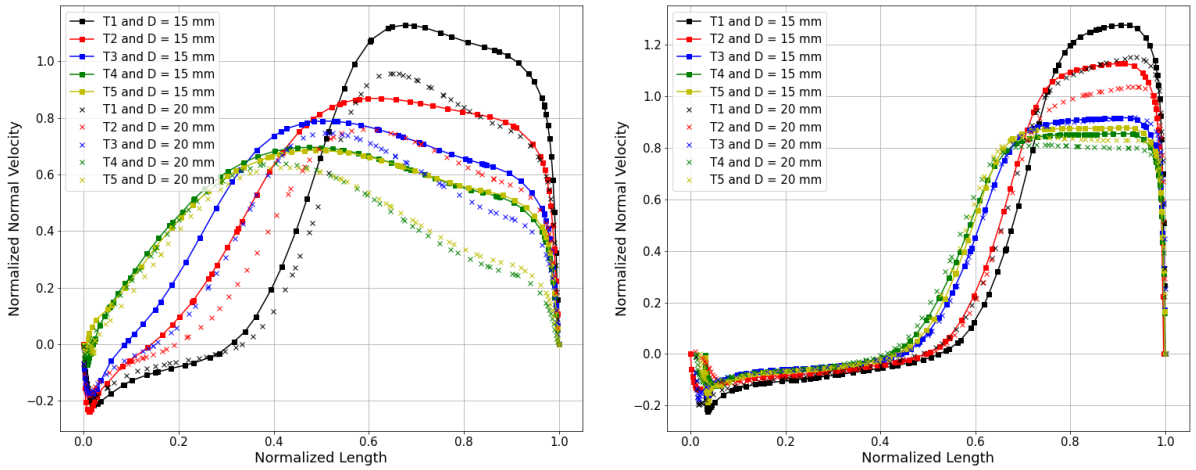

(a) Along curve A

(b) Along curve C

Figure 5.14: Normal velocity profiles along curves A and C with different liner tip shapes and distances D

5.5. Discussion

A total of 15 simulations have been performed using RANS. Parameters like shape of the inner liner tip, the ratio of the channel heights (H2/H1) and the distance between the inner liner tip and outer wall of the bend (denoted by D) have been varied and analyzed. From the velocity profiles shown in Sections 5.2, 5.3 and 5.4, we can see that all the three parameters can potentially be leveraged to play a key role in controlling the flashback resistance of the trapped vortex burner.

However, the drawback from these RANS simulations is that unsteady structures like vortices, or the presence of low velocity streaks close to the wall surfaces cannot be seen from these averaged velocity profiles. This is where LES, as a CFD tool, becomes important. Now that we have an idea of how the averaged air flows through these modified geometries, some amongst the interesting or relevant designs can be selected for further analysis using LES.

Unfortunately, due to time constraints, it is not possible to study all the cases with LES. Four out of the fifteen cases (including the base case which was shown in Section 4.4.2) will be simulated with LES. The sharp tips, T4 and T5, are quite interesting because the spiked shape changes the way the flow separates from the inner liner tip and may play a role in flashback if the flame propagates upstream close to that tip. The sharp tip T4 is also being studied experimentally at TU Delft's Process and Energy Department. Because of these reasons, T4 is selected for further analysis as the numerical results obtained in this work with LES can be useful in the future when more insight is required (for example, by experimentalists). So along with the base case, the sharp tip T4 (with H2/H1 = 3 and D = 20 mm) will be run with LES.

Gruber et al. [30] have already studied the impact of the channel height ratio H2/H1 on flame

flashback but the third parameter, distance D between the inner liner tip and outer wall of the bend, is still missing key information especially in the upper part of the U-bend where the flow separates from the outer wall (this was not visible in curves A to C). Therefore, the remaining two cases will be run with D = 15 mm and H2/H1 = 3. As for the tip shape in these two cases, both sharp tips T4 and T5 will be used.

Figure 5.15 summarizes all the cases which have been studied with RANS and the ones selected for further analysis are shaded in green. This will be discussed in the next chapter.

	H2/H1 = 3 D = 20 mm	H2/H1 = 2 D = 20 mm	H2/H1 = 3 D = 15 mm
T1			
T2			
T3			
T4			
T5			

Figure 5.15: Matrix showing the 4 cases selected for further analysis with LES (shaded in green)

6

Analysis with Large Eddy Simulation

After performing a preliminary study with RANS, four cases have been shortlisted for further analysis with LES. Table 6.1 provides a description of the LES cases. The first case, Case 1, has already been discussed in Section 4 and it is included here to serve as a reference case to compare with the other LES simulations.

Case Name	Tip Shape	H2/H1	D in mm
Case 1	T1	3	20
Case 2	T4	3	20
Case 3	T4	3	15
Case 4	T5	3	15

Table 6.1: Table describing the shortlisted geometries to be analysed with LES

6.1. Case Setup in Fluent

The LES simulations in this section are run using mesh M3 from Chapter 4, which was able to capture the turbulent flow accurately in the U-bend. Along with the mesh, the same boundary conditions discussed in Section 4.2 are used. Since we are only modifying the geometry in the U-bend region, the same inlet profiles can be used with the spectral synthesizer algorithm in Fluent. WALE was the subgrid scale model used for the simulations. Since the same inlet profiles were used, the Reynolds number for all the simulations was 7000.

The RANS simulations obtained in the previous chapter were used as the initial solutions for the LES simulations. An adaptive time step was used to ensure that the simulations do not become unstable due to a high CFL number. Table 6.2 contains all the details regarding the time step size and the maximum CFL number observed in the simulations. The table also

mentions the number of CPU cores and CPU time (no. of cores $\times$ total run time) used for the simulations. Cases 1 and 3 required shorter run times compared to the other cases due to a larger time step. Once the flow has fully developed (we see the presence of turbulent structures) in the burner (which was around 0.05s), data sampling was started and continued until the simulation ran for a total time of 0.02s (when it has become statistically steady).

Case Name	No. of CPU cores	Total CPU time [hours]	Avg. Δt [s]	max. Courant number
Case 1	20	4300	2.9e-06	0.81
Case 2	22	11600	1.1e-06	0.69
Case 3	18	5600	2.3e-06	0.63
Case 4	20	10000	1.13e-06	0.96

Table 6.2: No. of CPU cores, CPU time (to run 0.2s of flow), time step Δt and Courant number for each case

6.2. Results and Discussion

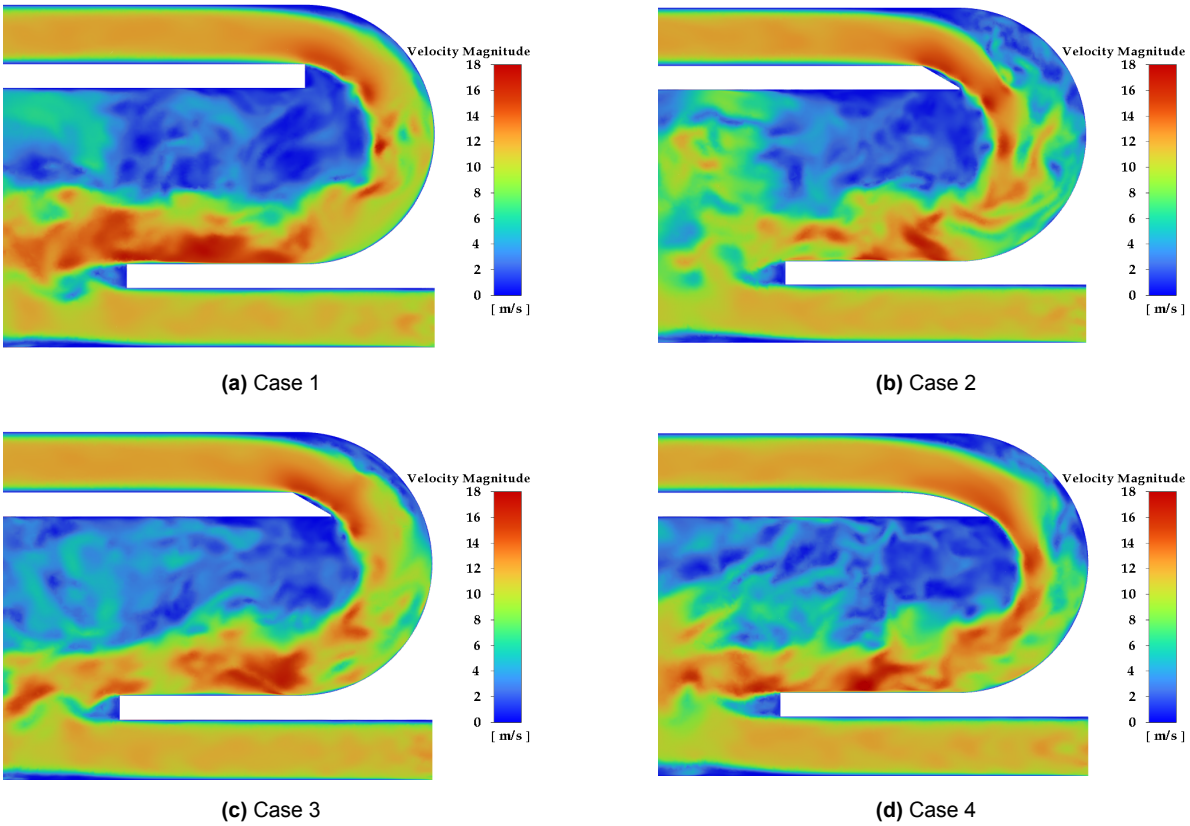

(a) Case 1

(b) Case 2

(c) Case 3

(d) Case 4

Figure 6.1: Instantaneous velocity magnitude contours for Cases 1, 2, 3 and 4

With LES, it is possible to observe and study transient features that may occur when turbulent air flows through a geometry like the trapped vortex burner. Figure 6.1 shows the instantaneous velocity contour plots for all the four cases and we can clearly see the presence of

some unsteady flow structures in the bend region.

As the flow separates from the inner liner tip, we see vortical structures appearing along the inner shear layer of the flow in all four cases. We also see the flow separating from the outer wall of the bend as it enters the U-bend region, something we already observed from the RANS simulations. However, with these LES results, we notice these thin low velocity 'finger' like structures or 'streaks' also present adjacent to the curved wall. These low velocity layers, which flow downstream along with the high velocity turbulent flow, may serve as a pathway for flame flashback when it strikes a flame front in the burner.

In order to gain more insight into these near wall structures, a plane was created in Fluent to visualize the flow from the top as it enters the bend (shown in Figure 6.2).

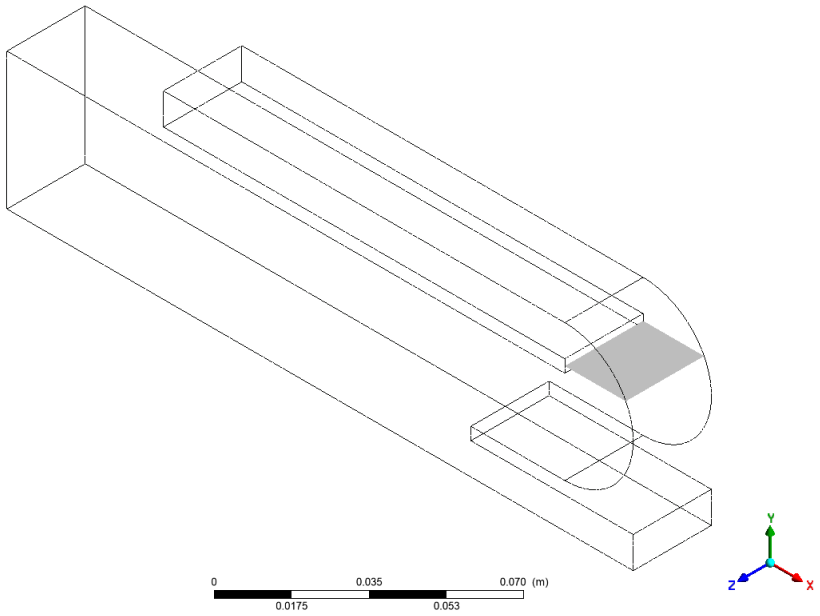

Figure 6.2: The plane (grey) used for visualizing the flow as it enters the U-bend region of the burner

The velocity contours visualized on this plane are shown in Figure 6.3. From these figures, a couple of observations can be made qualitatively. Firstly the layers adjacent to the outer bend show the low velocity 'streaks' that we noticed in Figure 6.1. For Cases 1, 3 and 4, these streaks don't extend as far away from the wall as Case 2. This would suggest that by altering the distance between the liner tip and the outer wall (distance D), the presence of low velocity streaks away from the wall can be altered.

The second observation can be made by looking at the layers adjacent to the liner tip, which is another path through which the flame can propagate upstream. Case 1, which had the blunt tip T1, has the largest low velocity area in this region and this is because the flow detaches from the upper edge of the tip as it enters the bend. On the other hand, the flow follows the surfaces of the sharp tips more closely, which we can clearly see from the size of the low

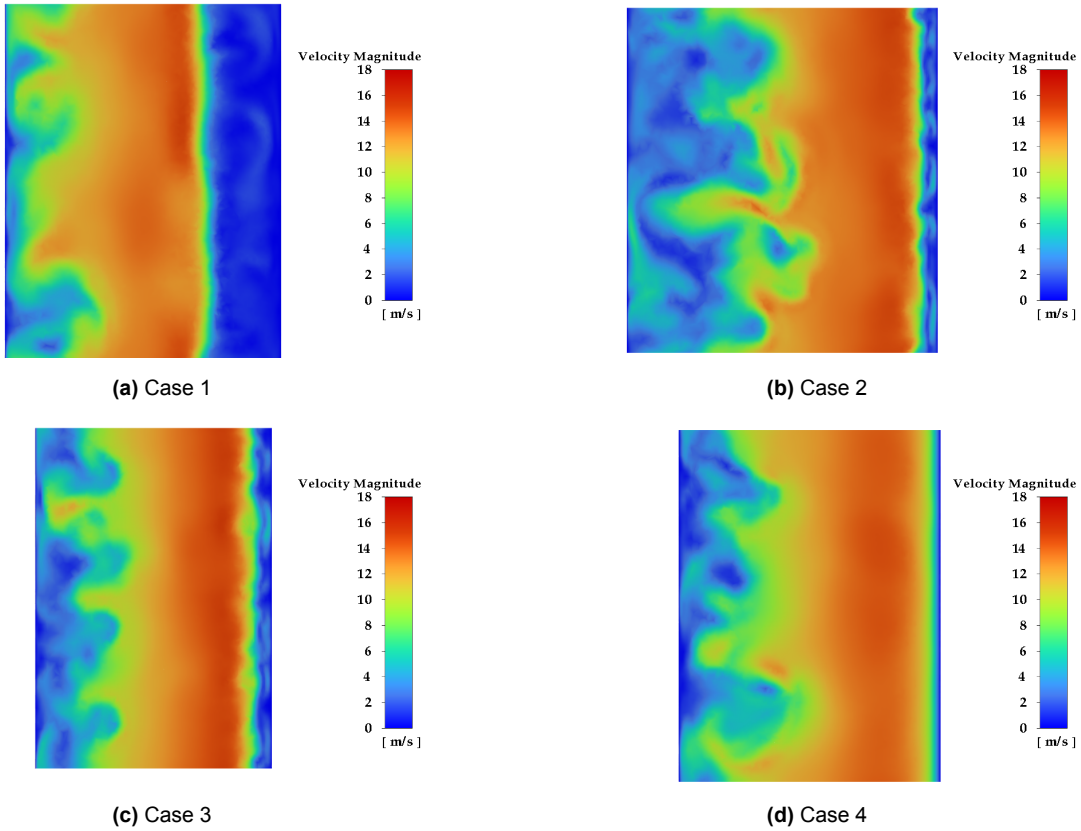

(a) Case 1

(b) Case 2

(c) Case 3

(d) Case 4

Figure 6.3: Instantaneous velocity magnitude contours, visualized on the plane shown in Figure 6.2 for Cases 1, 2, 3 and 4. The right side of the plots is the liner tip wall and the left side is the outer bend wall.

velocity layers. Case 4, which uses tip T5 (the sharp tip with a curved upper surface), has an even smaller low velocity area compared to Cases 2 and 3, which uses tip T4 (the sharp tip with a flat upper surface). This reduction in low velocity layer size can make it harder for a flame to creep upstream, around the liner tip, making it more resistant to flame flashback.

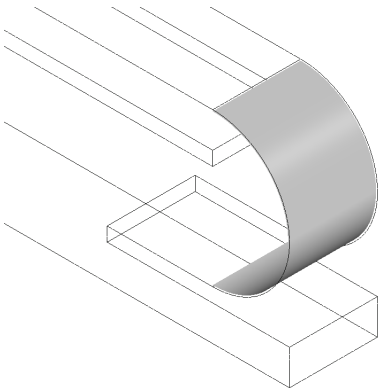

Figure 6.4: The curved plane (grey) used for visualizing the flow adjacent to the outer wall of the bend

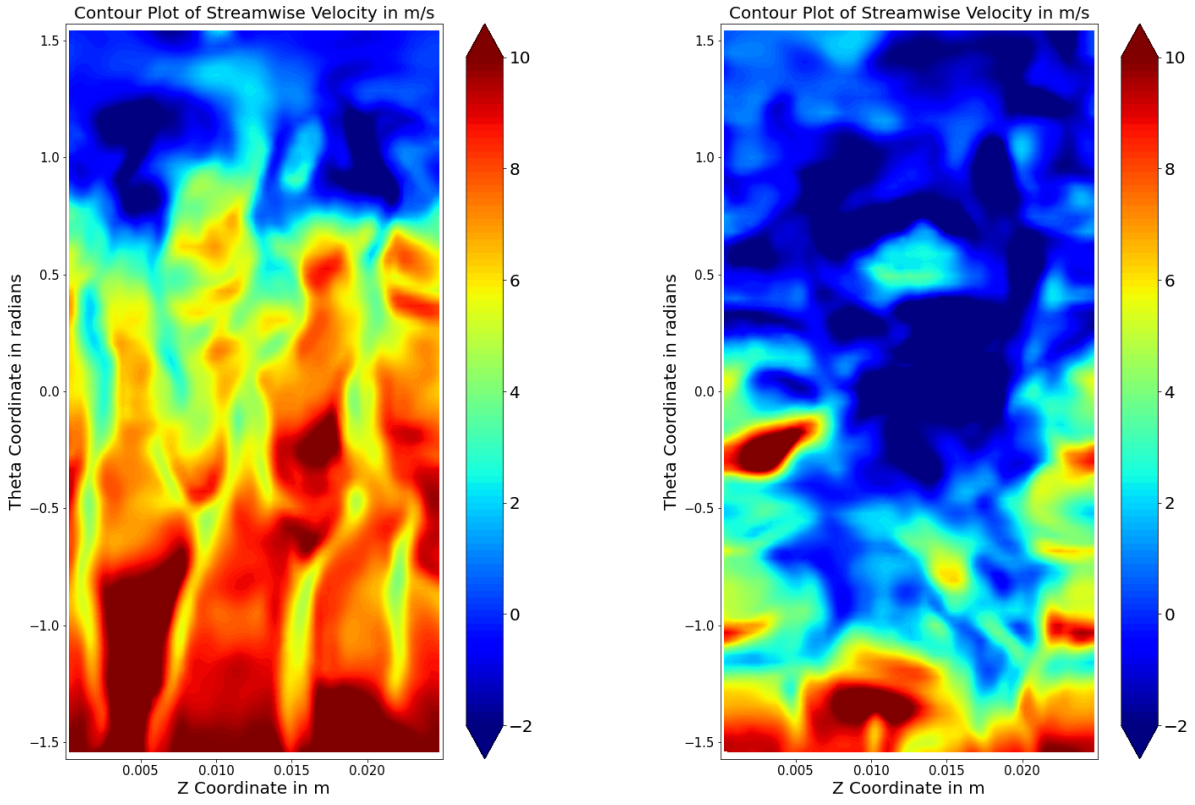

(a) Case 1

(b) Case 2

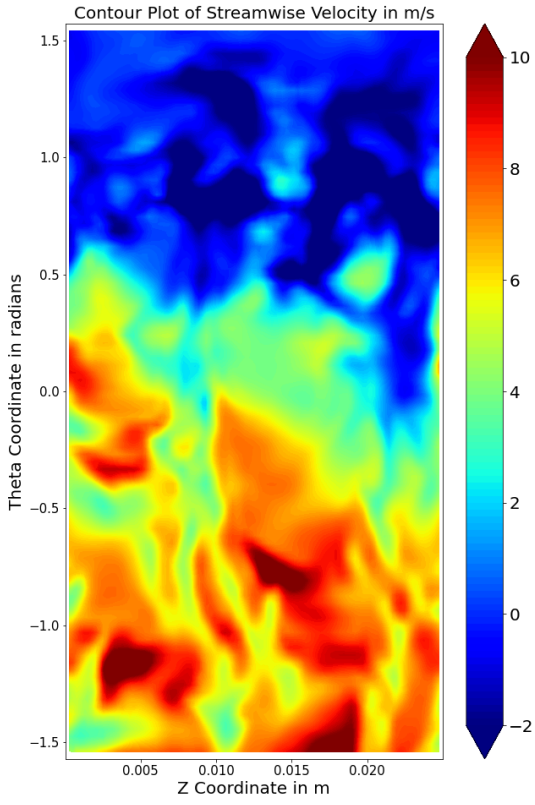

(c) Case 3

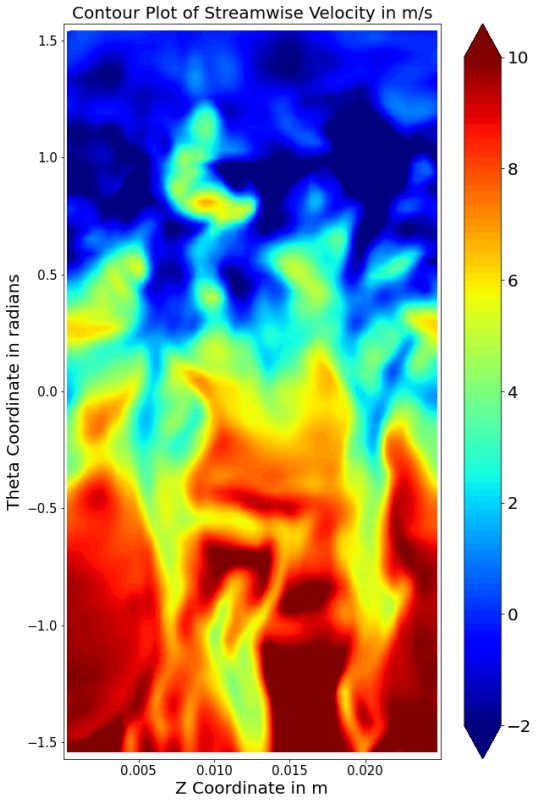

(d) Case 4

Figure 6.5: Instantaneous streamwise velocity [m/s] contours for Cases 1, 2, 3 and 4

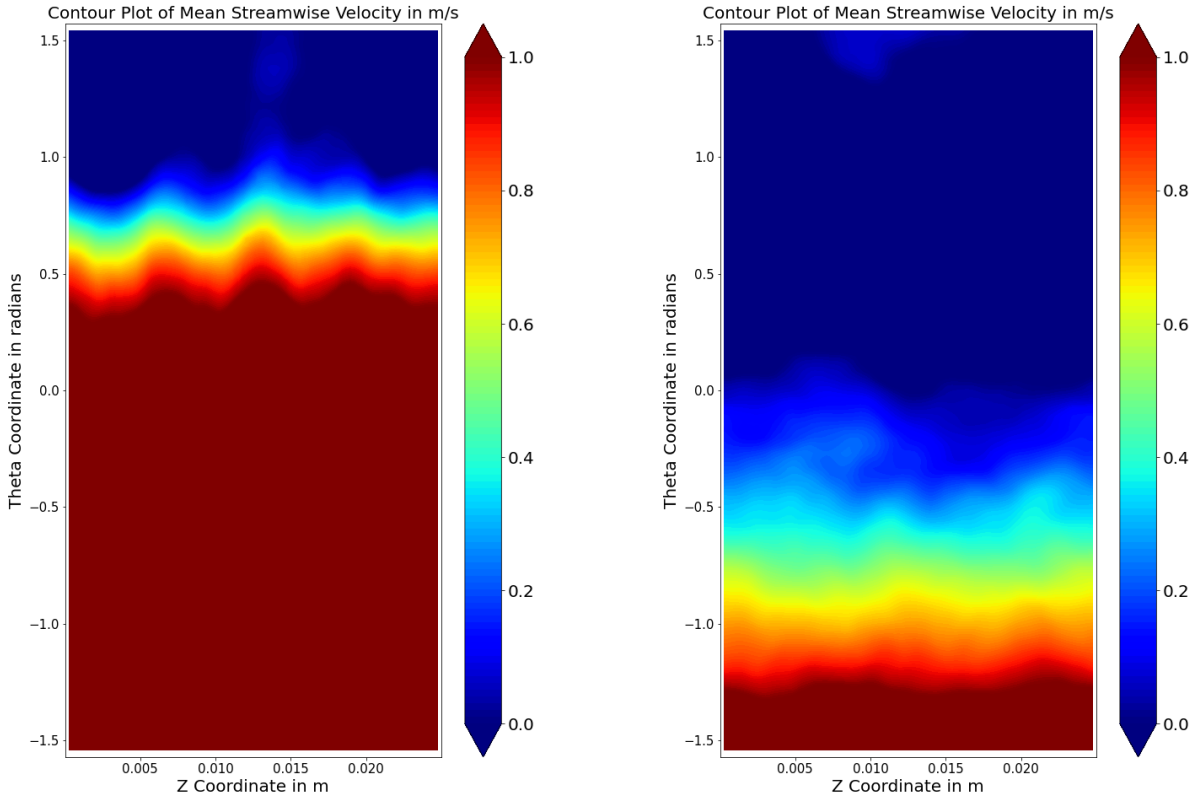

(a) Case 1

(b) Case 2

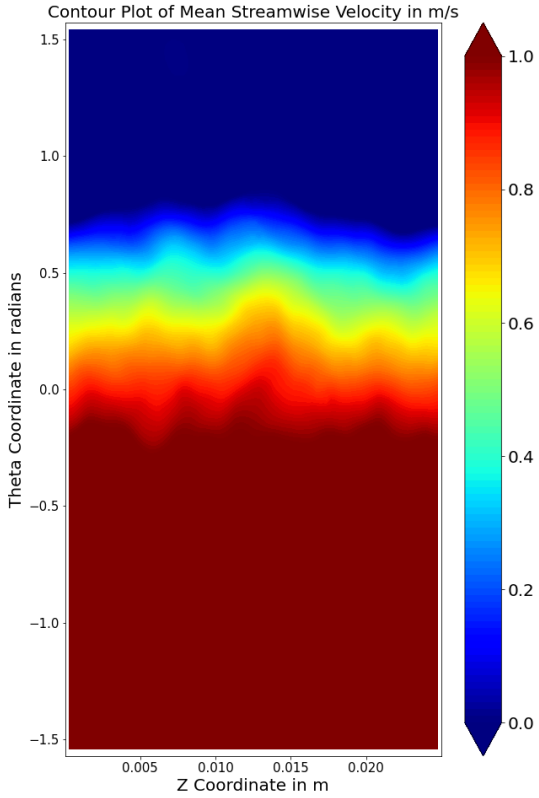

(c) Case 3

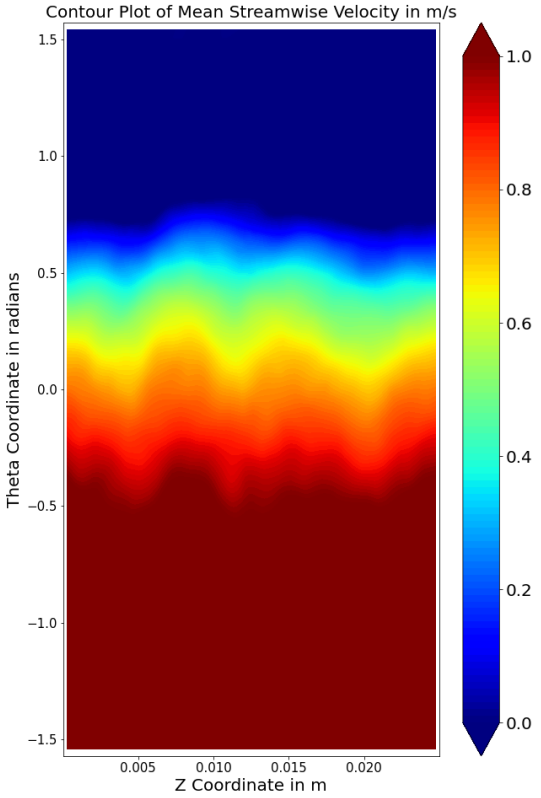

(d) Case 4

Figure 6.6: Mean streamwise velocity [m/s] contours for Cases 1, 2, 3 and 4

In order to perform a detailed analysis on the flow close to the outer bend, several curved planes were created, offset from the outer bend. One such plane is shown in Figure 6.4 and it can be used to visualize flow structures close to the outer bend.

For visualizing the velocity contours on this curved plane, the x and y velocities (in Cartesian system) were converted into tangential and radial (in cylindrical system) velocities using a Python script. This new velocity system is more appropriate for describing the flow features since the tangential velocity would be in the streamwise direction of the flow, making it the streamwise velocity. This streamline velocity from the curved plane is then displayed on a flat surface on Python to make it easier to visualize the flow (this is similar to taking the curved surface and flattening it).

Figure 6.5 shows instantaneous streamwise velocity contours obtained at a y+ value of 15 (from the outer wall of the bend). This y+ value was selected for analysis because the interaction between the turbulent flow and premixed flame front first occurs around this distance [15, 7]. Gruber et al. [15], from their DNS simulations, have found that this turbulence-flame interaction is responsible for the creation of back-flow regions of the flow and are usually found in near wall regions (y+ $\leq$ 20). In these contour plots, we can clearly visualize the structures that are found in the near wall regions.

The contour plots for all four cases show the presence of a recirculation zone in the upper part of the surface (above the plane shown in Figure 6.2). The size of this recirculation zone (in blue) is the largest for Case 2 (Figure 6.5b). These recirculation zones and the low velocity streaks (green coloured structures) may help in allowing the flame to propagate upstream of the bend as they offer lesser resistance to the flame front compared to the higher velocity turbulent flow.

The mean streamwise velocity contours along the same curved surface are shown in Figure 6.6. Figure 6.6b also shows how the streamline extend of the recirculation zone adjacent to the outer bend is the largest in Case 2, compared to the other cases. Both Cases 3 and 4 show identical instantaneous (Figures 6.5c and 6.5d) and mean (Figures 6.6c and 6.6d) streamwise profiles in these near wall regions. These sharp tips seem to only influence the velocity layers close to the liner tip (shown in Figures 6.3c and 6.3d).

In order to quantify these low velocity and recirculation structures, cumulative distribution functions of streamwise velocity in this curved surface (y+ = 15) for all the four cases were made. These curves are shown in Figure 6.7 and they give us an idea about the frequency of the low velocity structures found in the near-wall layers. From these curves it is quite clear that Case 2 has the highest frequency of low velocity structures compared to the other cases. Separation of flow in the boundary layer occurs in these low velocity streaks and an increased frequency of such structures would mean an increased chance of boundary layer separation in Case 2. And since boundary layer flashback occurs due to separation of the flow upstream of the flame, Case 2 would show an increased tendency to flashback with hydrogen flames.

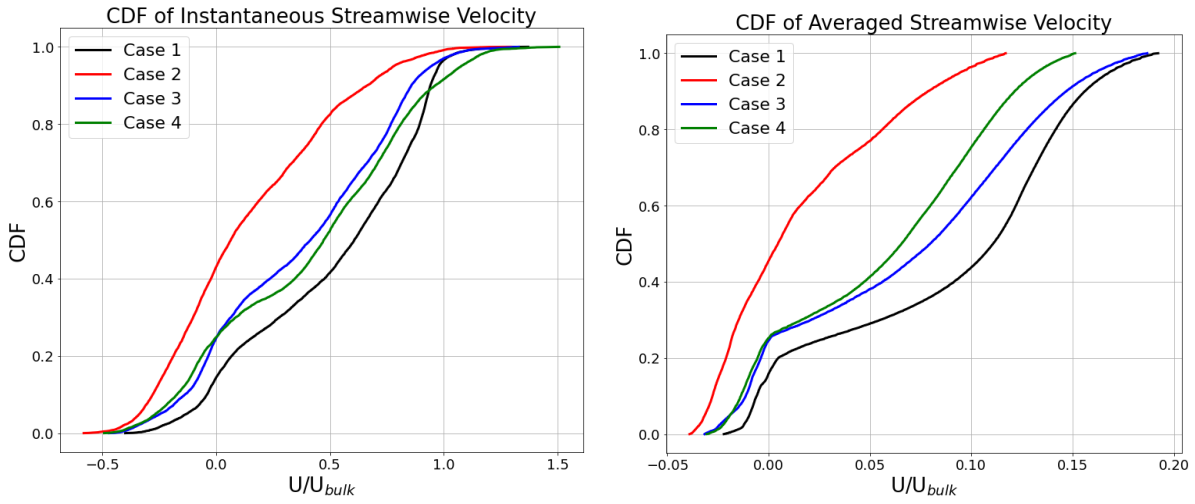

(a) CDF of instantaneous streamwise velocity

(b) CDF of mean streamwise velocity

Figure 6.7: CDF of streamwise velocity at y+ = 15 for all cases

An attempt at describing these low velocity structures using two-point correlations of streamwise velocity fluctuations was also done. Two point correlation for velocities u_1 and u_2 at locations x_1 and x_2 respectively is given by Equation 6.1 and normalized by Equation 6.2.

$$C_{u_1,u_2}(x_1, x_2) = \overline{u_1(x_1)u_2(x_2)} \tag{6.1}$$

$$R_{u_1,u_2}(x_1, x_2) = \frac{C_{u_1,u_2}(x_1, x_2)}{C_{u_1,u_2}(x_1, x_2)} \tag{6.2}$$

These correlations can also be computed by choosing a location x_1 and taking a separation vector r using Equation 6.3.

$$R_{u_1,u_2}(x_1, r) = \frac{\overline{u_1(x_1)u_2(x_1 + r)}}{\overline{u_1(x_1)u_2(x_1)}} \tag{6.3}$$

If the separation vector r is along the streamwise direction (parallel to the streamwise velocity vector), then we are computing the longitudinal correlations and if r is perpendicular to the velocity vector, we are computing the transverse correlations.

Figure 6.8 shows the longitudinal two point correlations of streamwise velocity fluctuations at $y+ = 15$, on the same curved surface shown in Figure 6.4. Low coefficient values would indicate uncorrelated velocities and high coefficient values would mean highly correlated velocities at these separation distances. The points in the upper half of the surface (above theta = 0 rad) have been ignored as they mostly contain the recirculation zone. With these coefficient curves, we notice Case 2 dropping to lower coefficient values at a faster rate compared to the other cases, implying uncorrelated velocities at these separation distances. This is probably due to the larger recirculation zone we see in Case 2, which would decrease the size of the other low and high velocity structures we see on this surface.

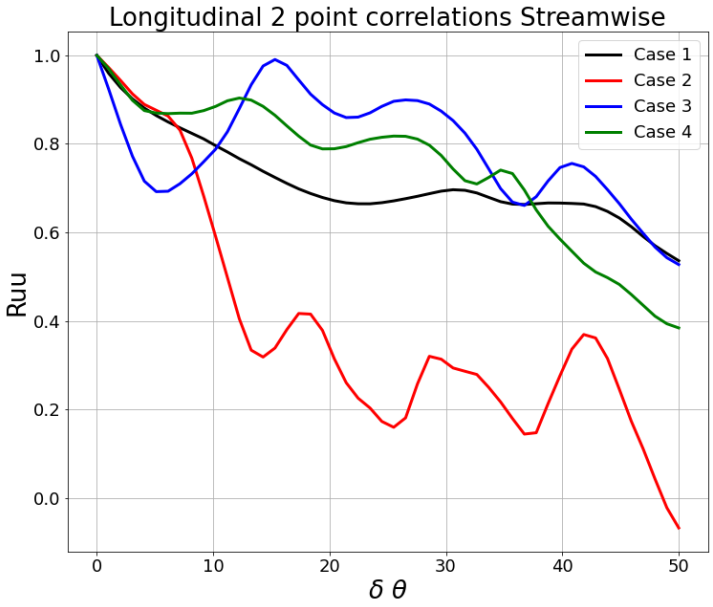

Figure 6.8: Longitudinal two point correlations of streamwise velocity fluctuations at y+ = 15

Cases 1, 3 and 4 show similar correlation trends since they have a similar structure. A higher correlation coefficient would indicate similar velocity values at the ends of the separation vector r. Unfortunately, due to these high coefficient values, it is not possible to compute the approximate length scales of these structures. The turbulent length scales are calculated by finding the area under these curves (integrating the coefficient functions from 0 to infinity). This difficulty is probably due to the complex nature of the flow in the bend region, which is inverted and highly turbulent in nature. Also from the mean plots, it is clear that the simulation has not reached complete convergence so this might also be an issue.

6.3. Summary

The previous section described the analysis done with the cold flow LES simulations in detail. Starting with a qualitative description of the flow using the side and top views of the burner, we observed the presence of certain low velocity structures close to the boundary layers of the flow adjacent to the outer bend. Visualizing these structures by calculating the velocity in the streamwise direction of the flow was successfully done which clearly showed the size of the recirculation zone and also the low velocity streaks appearing like 'fingers' between the high velocity turbulent flow.

From the streamwise contour plots and the cumulative distribution curves, we clearly see a huge difference between Case 2 and the remaining sharp tip cases. Case 2, which has its inner liner tip at a larger distance from the outer curved wall compared to Cases 3 and 4, shows a higher frequency of low velocity structures, which may indicate a higher flashback tendency. The curvature of the upper surface of the liner tip is also shown to influence the

thickness of the low velocity layer adjacent to the liner wall. Therefore. the size of the tip and also its distance from the outer bend are important parameters to control flame flashback in the trapped vortex burner as they influence the nature and size of the low velocity structures which might come in contact with the flame front.

An attempt at describing the size of these structures was made by using two point correlation functions. Unfortunately, the complex geometry and highly chaotic, turbulent nature of the flow makes it difficult to obtain useful information from the coefficient curves. Apart from this obstacle, we were successful in obtaining a lot of information and details about the flow in the U-bend region of the burner using the LES simulations and this will be useful in the future while optimizing the design of the trapped vortex burner.

7

Reactive Flow inside the Trapped Vortex Burner

This chapter will describe the reactive flow simulation performed on the trapped vortex hydrogen burner using LES. Section 7.1 will describe the model setup used in Fluent to run the reactive flow simulation. It will also include the initial and boundary conditions used. The validation of the results with PIV data will be shown in Section 7.2. This will be followed by a comparison with Gruber et al. [30], the only other available numerical work for a trapped vortex burner. Section 7.4 will include the results and analysis done with the simulation.

7.1. Model Setup

The mesh that was used for the cold flow analysis (M3 from Section 4.4.2) is used here for the reactive flow simulation. The simulation is performed for Re = 7000 with a hydrogen-air mixture, having an equivalence ratio of 0.3 at ambient conditions, flowing through the main inlet and a plain air mixture through the core inlet.

The geometry of the burner has the tip shape T1, H2/H1 ratio of 3 and D value of 20 mm. This is the same geometry for which the validation of the cold flow RANS/LES modelling was done in Section 4.4.2. In order to include the chemistry via finite rate kinetics, the artificially thickened flame model in Fluent was used. The LiDryer mechanism file [38], which contains 19 reactions and 9 species, is used since it has lesser reactions and species compared to mechanisms like GRI 3.0 or San Diego and it includes more up-to date data to represent hydrogen combustion under gas turbine conditions [68]. Table 7.1 summarizes the settings used in Fluent for the reactive flow analysis.

At the main inlet, a bulk velocity of 11.886 m/s was used to ensure the Reynolds number of flow was around 7000. Similar to the cold flow LES simulations, Fluent's spectral synthesizer

algorithm was used to artificially add the turbulence at the inlet. The mean velocity, turbulent kinetic energy and dissipation rate profiles, which are needed as inputs for the spectral synthesizer algorithm, are obtained from a precursor simulation of a hydrogen-air mixture flowing through a long channel. An outflow boundary condition was imposed at the outlet and the walls in the z-direction were defined as periodic boundaries.

LES Model	WALE
Chemistry Model	Finite rate with Thickened Flame
Tip Shape	T1
H2/H1	3
D	20 mm
Mechanism File	LiDryer
Pressure-Velocity Coupling	SIMPLE
No. of CPU cores	28
CPU time	16500 hours

Table 7.1: Simulation settings for the reactive flow

All the walls were assumed to be no-slip and isothermal, maintained at a constant temperature of 300K. In real case scenarios, the walls of the burner, especially the liner tip walls would have a hotter temperature value during combustion. However, due to the lack of information about the wall temperatures, they were assumed to be isothermal. Note that this is different from what Gruber et al. assume in their analysis where they used adiabatic condition for all the walls.

A precursor RANS reactive simulation was performed to obtain the initial solution for the transient LES simulation. Combustion was initiated by creating a high temperature patch (an area of high temperature) downstream of the U-bend section at the start of the simulation. This patch would help in igniting the fuel-air mixture, mimicking the actual ignition process in an experimental setup. Figure 7.1 shows the temperature field of the initial state. The next section will discuss the validation of the LES reactive model.

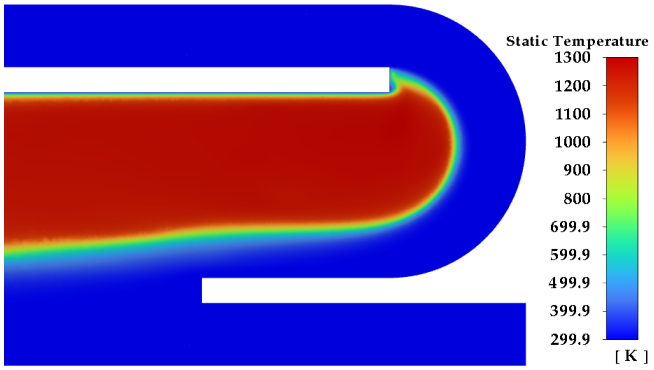

Figure 7.1: The temperature field of the initial solution, obtained using RANS

7.2. Validation with PIV

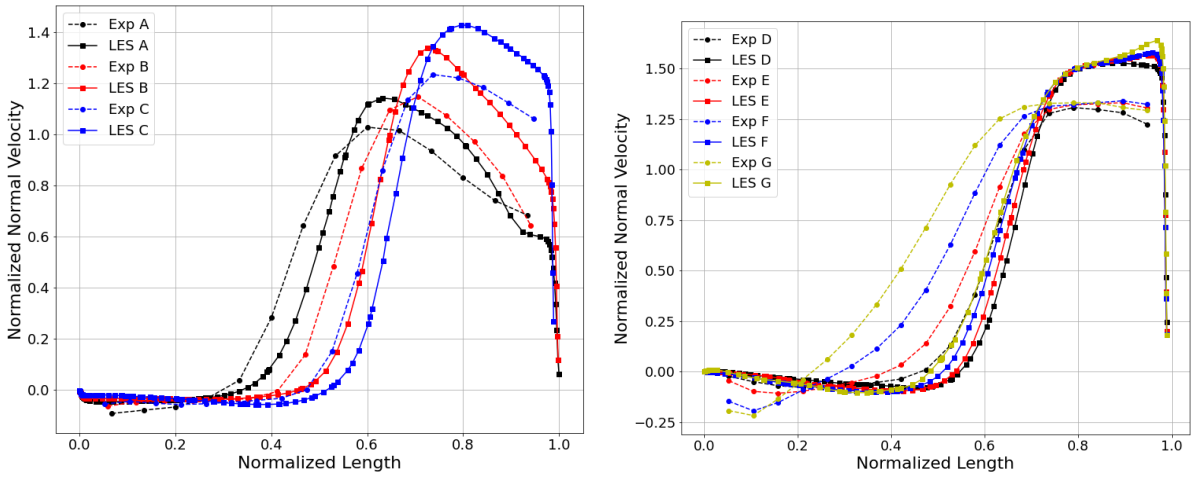

(a) Along curves A, B and C

(b) Along curves D, E, F and G

Figure 7.2: Comparison of normal velocity profiles with PIV data along the curves shown in Figure 4.8

The LES simulation ran for around 16500 CPU hours using 28 cores. An adaptable time step was used to ensure the simulation remains stable by not allowing high CFL numbers. The maximum CFL number was observed to be 1.3 and the average time step was 3.7x10^{-06} seconds.

In order to validate the approach, PIV results obtained with the same geometry and hydrogen-air mixture was used for comparison. Figure 7.2 shows how the velocity profiles obtained from our LES simulation compares with the PIV data. The velocity profiles are obtained along the curves shown in Figure 4.8. The velocity profiles show good agreement with the PIV data and seem to describe the velocity field accurately enough, especially in the bend region which had finer cells. The lack of experimental temperature data makes it difficult to validate our assumption about the wall temperatures.

We see some difference between the velocity profiles close to the liner wall in Figure 7.2b and this might be because of the presence of coarser cells (compared to the bend region). The size of the computational cells is important to accurately capture the chemistry interactions between all the species and hence this might be a reason we see a small deviation in these parts of the curves. However, the overall agreement with PIV is good and the model can be used to study the hydrogen flame in the trapped vortex burner.

7.3. Comparison with Previous Numerical Work

From our literature review of the trapped vortex burner, the only available numerical work with such a design was Gruber et al.'s [30] work using Reactive LES simulations on OpenFOAM's reactingFoam solver. They have used PIMPLE, which is hybrid version of SIMPLE and PISO

schemes, for the pressure-velocity coupling. The source term in the species equation is solved using a Partially-Stirred Reactor model and the dynamicKEqn eddy viscosity model is used as the eddy viscosity model for LES, which solves a transport equation for the subgrid scale turbulent kinetic energy [30].

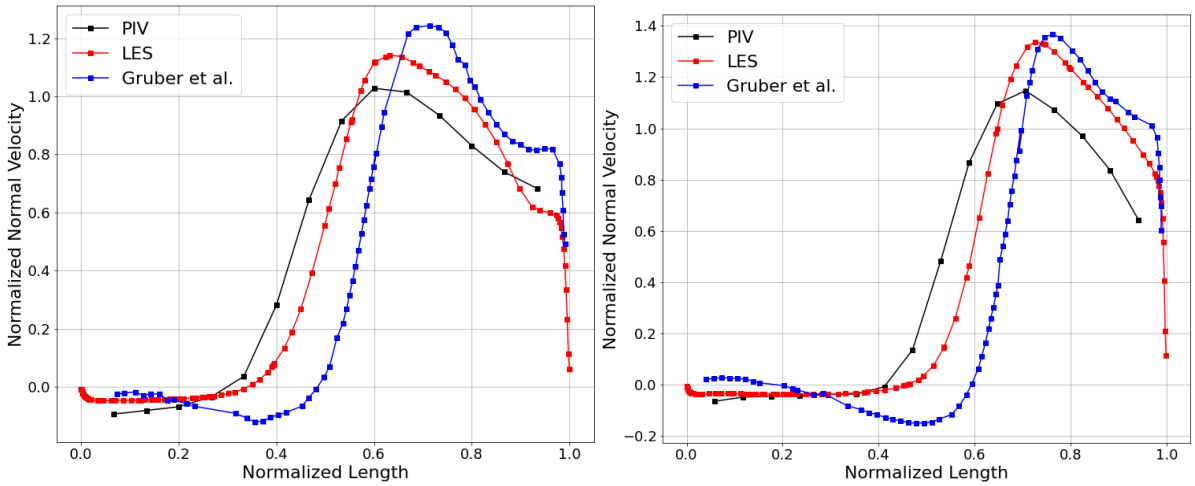

(a) Curve A

(b) Curve B

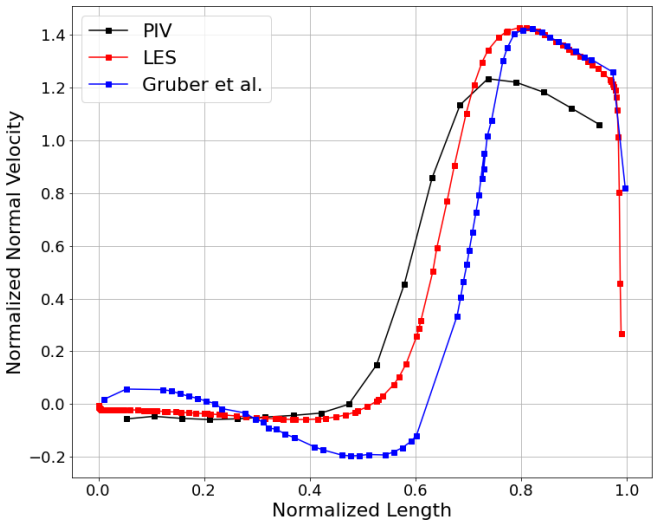

(c) Curve C

Figure 7.3: Comparison of normal velocity profile along curves A, B and C with Gruber et al. [30] and PIV values

For their main inlet, an algorithm called Synthetic Eddy Method (SEM), is used to generate synthetic turbulence at the inlet. The walls of the burner are assumed to be no-slip and isothermal (same temperature as the reactant mixture) but the liner walls (including the liner tip) are simulated with adiabatic boundary condition. Because of their scaled dimensions (channel heights H1 and H2 reduced by half), their simulations are actually performed with a Reynolds number of 3500 instead of 7000. Gruber et al. used a mesh with 60 million cells while our mesh M3 had only 1.1 million cells.

Figures 7.3a, 7.3b and 7.3c show the comparison of our LES results with Gruber et al.'s [30]

work for curves A, B and C respectively. Unlike the cold flow comparisons, where their peak velocity was higher than our LES profiles, the reactive flow profiles from both LES simulations seem to have almost the same peak values. A small difference exists in the high gradient region in the middle of the U-bend, where our results seem to be closer to the PIV results (Gruber et al.'s exhibit a small recirculation zone). This comparison, along with the validation shown in Section 7.2, show that our reactive flow model on Fluent is sufficient to provide some insights on combustion phenomena inside the trapped vortex hydrogen burner, and can be used for studying the behavior of the hydrogen flame.

7.4. Analysis of the Hydrogen Flame

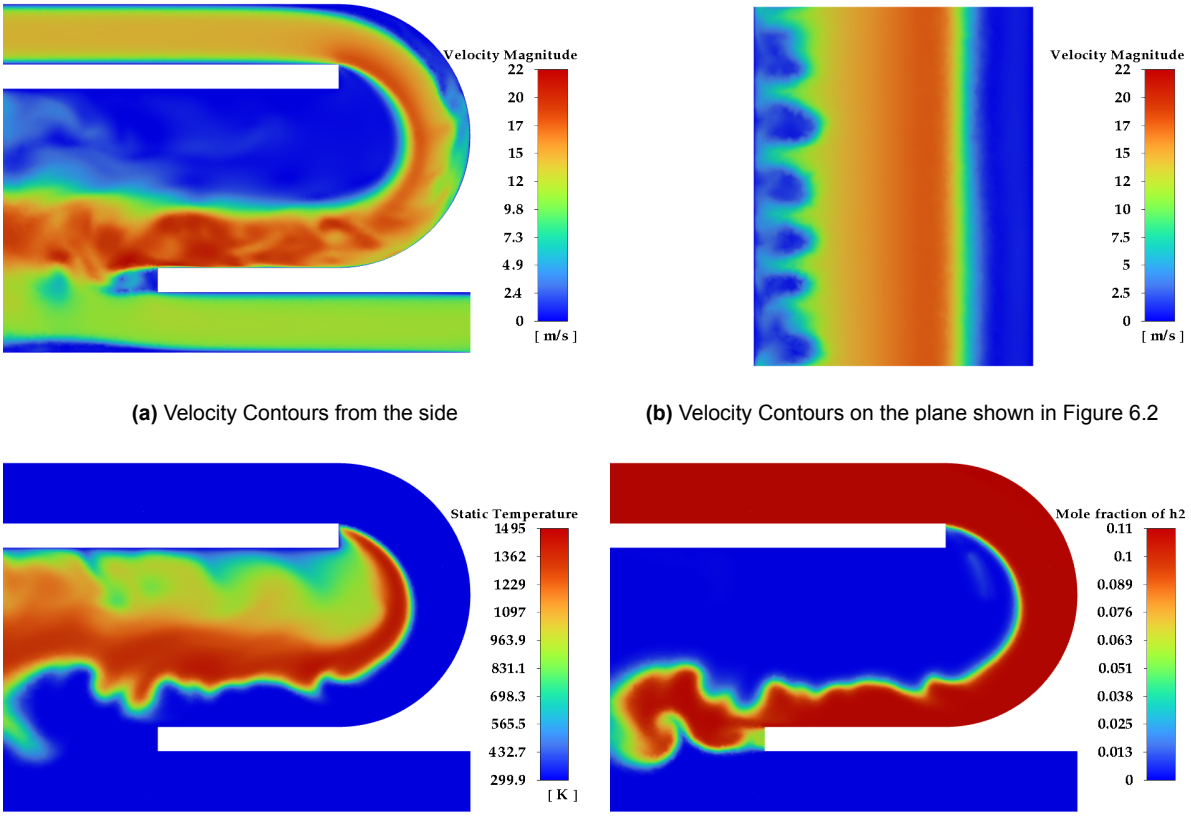

(a) Velocity Contours from the side

(b) Velocity Contours on the plane shown in Figure 6.2

(c) Temperature Contours

(d) Mole Fraction of H_2

Figure 7.4: Results from the Reactive LES Simulation

Figure 7.4 shows typical instantaneous velocity, temperature and H_2 mole fraction contours obtained from our LES simulation. The contours show how the hydrogen flame is stabilized in the trapped vortex region which is created due to the separation of the flow from the liner tip. They also show the presence of instabilities downstream of the U-bend region, in the shear layer between the secondary flow inlet and the core flow inlet. From these images, it is also apparent that resolution in the downstream area could be increased, however due to

the limitation of computational resources this is deemed sufficient for the present exploratory analysis.

The velocity contour (Figure 7.4a) qualitatively shows the same flow pattern as the cold flow result obtained in Section 4.4.2. The presence of a separation layer from the outer bend wall can clearly be seen and a top view like Figure 7.4b shows the low velocity structures adjacent to the wall (which we also see in our cold flow LES cases in Chapter 6).

The temperature contour in Figure 7.4c gives us an idea of what the flame front looks like inside the trapped vortex burner. The stabilized flame in the U-bend seems to have a smooth convex shape upstream, probably helped by the high velocity flow, but this changes downstream as we see the presence of convex and concave shaped cusps.

Figure 7.4d also shows the presence of unburnt H_2 downstream of the U-bend, implying incomplete combustion. Gruber et al. [30] have also observed the same feature and pointed out that it might be because of the low equivalence ratio of the hydrogen-air mixture (ϕ = 0.3), which is close to its lower flammability limit.

From a preliminary study using Cantera, we know that the adiabatic flame temperature for a hydrogen-air mixture with ϕ = 0.3, using the same LiDryer chemical mechanism and a multicomponent transport model, is around 1180 K. However, the temperature field from our LES simulation shows a much higher value close to 1400K around the flame front. This might be a super adiabatic flame temperature, a phenomenon where the temperature of a premixed flame is higher than its adiabatic flame temperature [69, 70]. Schurr et al. [70] mention that this phenomenon is caused by the endothermic reactions that occur when H_2O dissociates in the post flame region and also because of the presence of super equilibrium concentrations of species like H_2.

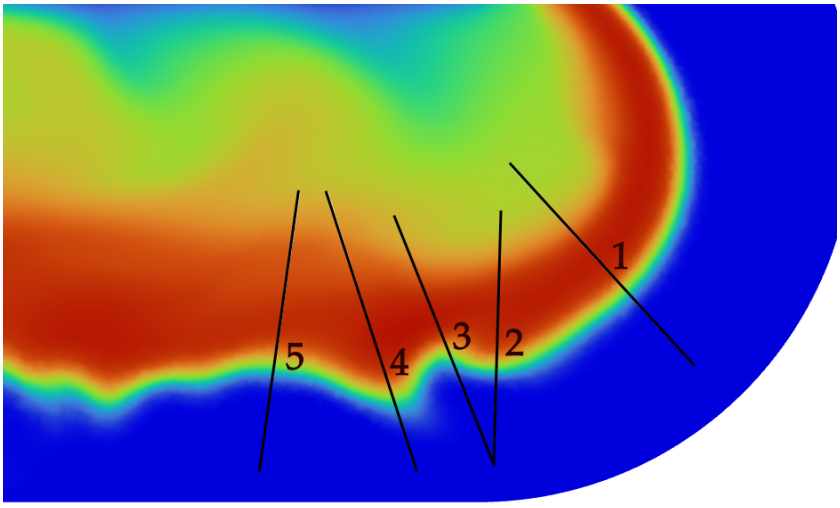

Figure 7.5: Profiles used for analyzing the diffusion of H_2 across the flame front

In order to understand the behavior of the hydrogen flame in the trapped vortex burner, it is necessary to understand how hydrogen diffuses into the flame. Hydrogen has a non-unity Lewis number (less than one) which causes it to have unequal thermal and mass diffusion rates. This property causes the flame to behave differently when compared to other stable hydrocarbon flames, giving it a cellular structure and developing thermo-diffusive instabilities on its surface (explained in Section 2.4.4).

To analyze this, 5 profiles (labelled 1 to 5), shown in Figure 7.5, are drawn across the flame front. For a stationary flame, the convex parts of a flame front (shaped like the parts represented by curves 2 and 4) would be richer in hydrogen compared to the concave parts (like profiles 3 and 5). However, in the trapped vortex burner, the presence of a turbulent flow can alter this behavior by convecting some of the hydrogen into the flame.

The mole fraction of H_2 and the temperature along the different profiles are shown in Figure 7.6. The results are also compared with a one-dimensional flame from Cantera. In Figure 7.6a, we observe how the H_2 concentration profiles across the flame front in the trapped vortex burner have a different slope compared to Cantera. The presence of an incoming turbulent flow which has been inverted due to the structure of the burner (ignored in Cantera) seems to significantly alter the behavior of the flame. Figure 7.6b shows the flame exhibiting a higher flame temperature, which is the super adiabatic flame temperature discussed before. This might be because of the existence of higher concentrations of the reacting fuel species in these convex/concave cusps, creating regions with a higher local equivalence ratio.

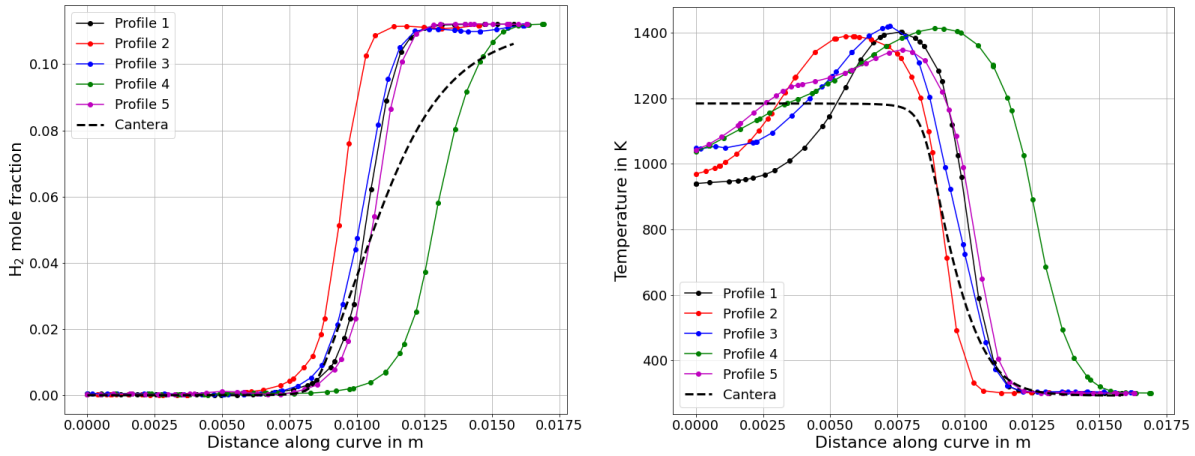

(a) H_2 mole fraction

(b) Temperature

Figure 7.6: Comparison of H_2 mole fraction and temperature along the curves shown in Figure 7.5

In order to investigate the local fuel/air ratio, mixture fraction Z for the flow is computed using [31]:

$$Z = \frac{Z_H/(nW_H) + 2(Y_{O_2,u} - Z_O)/(\nu'_{O_2} W_{O_2})}{Z_{H,1}/(mW_H) + 2Y_{O_2,u}/(\nu'_{O_2} W_{O_2})} \tag{7.1}$$

where Z_j is the mass fraction of element j in the mixture, subscript 1 is used to denote the fuel stream (here assumed to be pure H_2), n is the total number of moles, W_j is the molecular weight of species j and ν'_j is the stoichiometry coefficient of O_2. This term is usually used for non-premixed flames since they have non-homogenous mixtures so an expression for local fuel/air ratios is more relevant for diffusion flames. The mixture fraction is defined in such a way that Z has a value 1 in the fuel stream and 0 in the oxidizer stream. Figure 7.7 shows the mixture fraction contour obtained for our reactive flow.

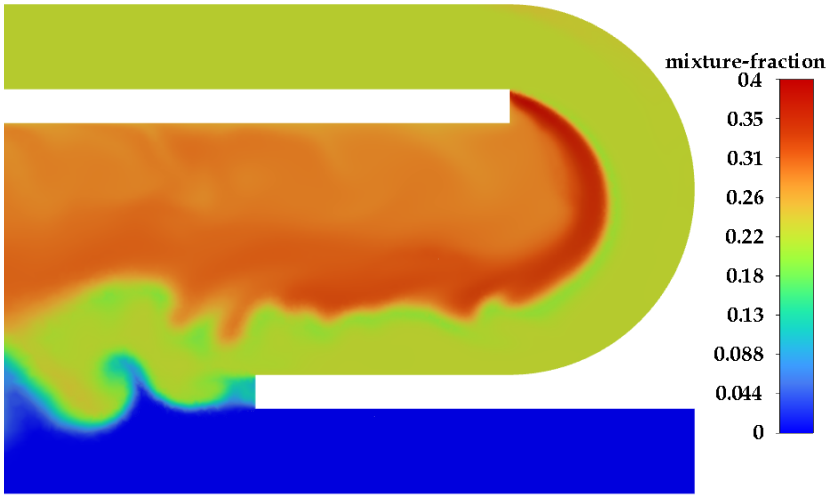

Figure 7.7: Mixture fraction contour for the reactive flow

In Figure 7.7, we observe regions within the burnt gases having a higher concentration of the reacting fuel species than the incoming flow. This confirms the presence of higher amounts of hydrogen diffusing into the convex/concave structures of the flame, leading to significantly higher temperatures in these structures.

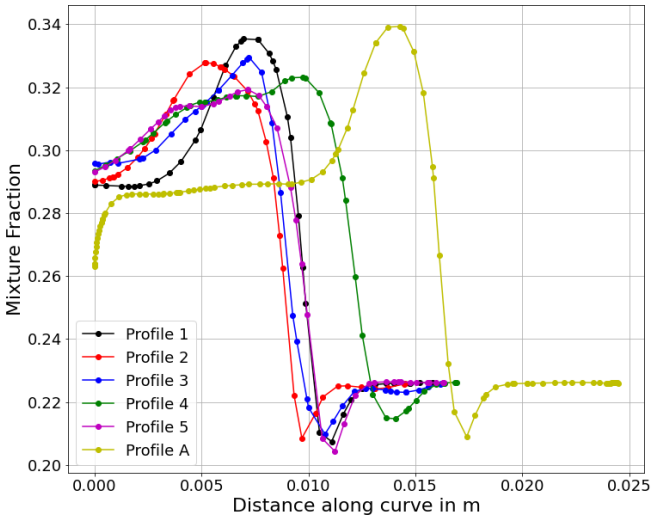

Figure 7.8: Comparison of mixture fraction along the curves shown in Figure 7.5 and Curve A from Figure 4.8

Figure 7.8 shows the comparison of the mixture fraction values along various curves drawn across the flame front. The peak mixture fraction for all the curves are different, which would mean that the diffusion of hydrogen into the flame is non-uniform across the structure of the flame. Profiles A, 1, 2 and 4 are drawn across the convex parts of the flame and Profiles 3 and 5 across the concave structures. The more downstream locations seem to have a lower local fuel/air ratio compared to the upstream region.

This analysis of the combustion of hydrogen in the trapped vortex burner gave us interesting insights into the flame structure and diffusion of the fuel into the flame. From a smooth convex shaped front in the initial part of the bend, to a wrinkled structure downstream in the channel of the burner, the diffusion of the reacting hydrogen species seem to be different across these flame structures. Further analysis might be required to understand this phenomenon better in the trapped vortex burner.

8

Conclusion and Recommendations

Hydrogen as a fuel has generated a lot of interest due to its ability to not produce any carbon dioxide during combustion, making it a popular choice as an alternative to fossil fuels. However, from our literature review, we can see that there are still some challenges, particularly boundary layer flashback, that need to be overcome in order to safely use it in gas turbines.

The main objective of this work was to study the flow (both non-reactive and reactive) inside an academic trapped vortex hydrogen burner using RANS and LES, and understanding the effect of certain design parameters on the flow features. From Eichler's work [10], we know that boundary layer flashback happens because of the separation of the flow upstream of the flame. This makes the turbulent boundary layer important for our study. Hence, the cold flow (non-reactive) simulations on the trapped vortex burner were used to study the boundary layer in the U-bend region.

Various geometrical parameters that might affect the boundary layer flashback tendency of the burner were identified and simulated. Previous numerical study on a similar design [30] have found the shape of the inner liner tip and channel thickness (H2/H1) to be important parameters. The distance between the inner liner tip and the outer wall of the U-bend is another feature which we investigated along with the previous two. A detailed analysis to identify and study the low velocity structures adjacent to the outer bend was done.

Finally, reactive flow inside the burner was also simulated in Fluent to study the features of the hydrogen flame. An analysis which involved studying the temperature profile, shape of the flame front in the burner and also the diffusion of hydrogen into the flame was done and interesting observations were made which showed the hydrogen flame exhibiting super adiabatic flame temperatures close to the flame front due to the increased fuel/air ratios within the flame.

This chapter concludes the research work done in this thesis and the concluding remarks related to the objectives, described in Chapter 1, are given below:

- What are the computational model requirements necessary to study the boundary layer in the U-bend section of the trapped vortex burner?
  - Cold flow RANS and LES models were made with Fluent to describe the flow inside the trapped vortex hydrogen burner. The RANS model makes it possible to run different geometrical parameters at a low computation cost and the LES model can be used for a detailed analysis of the turbulent structures. An optimized mesh was identified which gave good agreement with experimental results and also saved a lot of computation effort instead of running a highly refined mesh. The realizable $k-\epsilon$ RANS and WALE LES models were used for the simulations. Both models could be extended to study different design versions of the trapped vortex burner.
  - A reactive LES model was also developed on Fluent to study the hydrogen flame features inside the trapped vortex burner. For this, finite rate chemistry, combined with the Artificially Thickened Flame model was used to capture the combustion chemistry. This Fluent model was also validated with PIV data and could be used to describe the flow and flame features quite accurately.
- What effect does the inner liner tip, channel height ratio and the distance of the tip from the outer bend wall have on the turbulent structures and how can this be used to reduce flashback tendency of the flame?
  - Different configurations were analyzed with LES, focusing on the low velocity structures that were visualized close to the outer wall. Since we know that a flame propagates upstream through the boundary layers of the incoming flow, it was necessary to find ways to improve the velocity profile in these regions.
  - The parametric study done using RANS showed how the modifications impacted the turbulent flow in the bend. By changing the shape of the tip, the low velocity layer adjacent to the liner tip could be altered. Sharp tips T4 and T5 showed interesting results as they had a lower boundary layer thickness adjacent to the liner tip walls, compared to the initial design of the burner. Among the sharp tips, T5 showed the lowest boundary layer thickness close to the liner tip.
  - Channel height ratio (H2/H1), which was identified by Gruber et al. [30], was another parameter investigated using RANS. By reducing the channel height ratio, the downstream velocity profile adjacent to the bend could be improved by increasing the velocity in these layers.
  - The distance of the tip from the outer bend wall (parameter D) was the third parameter investigated with RANS and further analysis was done using LES. This parameter also improved the velocity profile adjacent to the outer wall by reducing the thickness of the boundary layer adjacent to the outer wall of the U-bend.

- With the cold flow LES analysis, the streamwise low velocity structures were visualized along with the size of the recirculation zone adjacent to the outer wall of the U-bend region. From this analysis, Case 2 showed the least desirable structures while Cases 1, 3 and 4 showed similar results qualitatively. Cumulative distribution functions showed that Case 2 had the highest frequency of low velocity structures compared to the other cases.

8.1. Recommendations

This work opens up several ideas for future investigations. Considering the results, future work can be directed towards:

- Investigating the remaining geometry configurations from Figure 5.15 (Tips T2 and T3) that unfortunately could not be done in this work due to time constraints.
- Performing reactive flow simulations with various burner geometries, similar to the cold flow analysis done in this work. The reactive flow can be studied with different geometrical modifications like tip shape, channel height ratio and distance of the tip from the outer wall.
- Incorporating the correct liner wall temperature to make the simulations more accurate especially in the areas close to the liner.
- Simulating reactive flows with a different combustion model to investigate if the turbulence-chemistry interaction may have been modified significantly because of the use of a thickening factor.
- Performing a transient analysis to investigate the flashback limits of the different configurations and also to study the flashback paths taken by the hydrogen flame.
- Study the cold and reactive flow features inside the burner at elevated temperature and pressure conditions, similar to that of an operating gas turbine.

References

[1] IPCC. *Climate Change 2023: Synthesis Report. Contribution of Working Groups I, II and III to the Sixth Assessment Report of the Intergovernmental Panel on Climate Change*. 2023.

[2] IEA. *CO2 Emissions in 2023, IEA, Paris https://www.iea.org/reports/co2-emissions-in-2023*. 2024.

[3] *Paris Agreement*. Viewed on 12-02-2024. URL: `https://unfccc.int/process-and-meetings/the-paris-agreement`.

[4] *Article on COP 28*. Viewed on 12-02-2024. URL: `https://www.bbc.com/news/science-environment-67143989`.

[5] IPCC. *Climate Change 2022: Mitigation of Climate Change. Working Group III Contribution to the IPCC Sixth Assessment Report*. 2022.

[6] F. Dawood, M. Anda, and G.M. Shafiullah. “Hydrogen production for energy: An overview”. In: *International Journal of Hydrogen Energy* 45 (2020).

[7] V. Hoferichter. *Boundary Layer Flashback in Premixed Combustion Systems*. 2017.

[8] H. Pitsch. “The transition to sustainable combustion: Hydrogen- and carbon-based future fuels and methods for dealing with their challenges”. In: *Proceedings of the Combustion Institute* (2024).

[9] A. Kalantari and V. McDonell. “Boundary layer flashback of non-swirling premixed flames: Mechanisms, fundamental research, and recent advances”. In: *Progress in Energy and Combustion Science* 61 (2017), pp. 249–292.

[10] C.T. Eichler. *Flame Flashback in Wall Boundary Layers of Premixed Combustion Systems*. 2012.

[11] M. Kroner et al. “Flame Propagation in Swirling Flows—Effect of Local Extinction on the Combustion Induced Vortex Breakdown”. In: *Combustion Science and Technology* 179 (2007).

[12] G.M. Baumgartner. *Flame Flashback in Premixed Hydrogen-Air Combustion Systems*. 2014.

[13] B. Lewis and G. Von Elbe. “Stability and structure of burner flames”. In: *The Journal of Chemical Physics* 11 (1943).

[14] G. Von Elbe and M. Mentser. “Further Studies of the Structure and Stability of Burner Flames”. In: *The Journal of Chemical Physics* 13 (1945).

[15] A. Gruber et al. “Direct numerical simulation of premixed flame boundary layer flashback in turbulent channel flow”. In: *Journal of Fluid Mechanics* 709 (2012).

[16] A. Endres and T. Sattelmayer. “Large eddy simulation of confined turbulent boundary layer flashback of premixed hydrogen-air flames”. In: *International Journal of Heat and Fluid Flow* 72 (2018).

[17] A. Endres and T. Sattelmayer. “Numerical investigation of pressure influence on the confined turbulent boundary layer flashback process”. In: *Fluids* 4 (2019).

[18] V. Hoferichter, C. Hirsch, and T. Sattelmayer. “Prediction of Confined Flame Flashback Limits Using Boundary Layer Separation Theory”. In: *J. Eng. Gas Turbines Power* 139 (2017).

[19] V. Hoferichter et al. “Comparison of Two Methods to Predict Boundary Layer Flashback Limits of Turbulent Hydrogen-Air Jet Flames”. In: *Flow, Turbulence and Combustion* 100 (2018).

[20] B. S. Stratford. “The prediction of separation of the turbulent boundary layer”. In: *Journal of Fluid Mechanics* 5 (1959).

[21] J. Tober. *Boundary layer flashback prediction of a low emissions full hydrogen burner for gas turbine applications*. 2019.

[22] O. H. Björnsson. *Boundary layer flashback prediction for low emissions full hydrogen gas turbine burners using flow simulation*. 2019.

[23] C.K. Sarakatsanis. *Boundary layer flashback prediction for high hydrogen flames at gas turbine burner geometry and operating conditions*. 2020.

[24] Y.C. Lin et al. “Turbulent Flame Speed as an Indicator for Flashback Propensity of Hydrogen-Rich Fuel Gases”. In: *J. Eng. Gas Turbines Power* 135 (2013).

[25] A. Kalantari, E. Sullivan-Lewis, and V. McDonell. “Flashback Propensity of Turbulent Hydrogen–Air Jet Flames at Gas Turbine Premixer Conditions”. In: *J. Eng. Gas Turbines Power* 138 (2016).

[26] P. Stuttaford et al. “FlameSheetTM Combustor Engine and Rig Validation for Operational and Fuel Flexibility with Low Emissions”. In: *Proc. ASME Turbo Expo* (2016).

[27] P. Stuttaford et al. *Flamesheet combustor dome*. US Patent 9,752,781 B2. 2017. URL: `http://www.google.it/patents/US9752781`.

[28] P. Stuttaford and H. Rizkalla. *Flamesheet combustor contoured liner*. US Patent 10,060,630 B2. 2018. URL: `http://www.google.it/patents/US10060630`.

[29] D. Noble et al. “Assessment of Current Capabilities and Near-Term Availability of Hydrogen-Fired Gas Turbines Considering a Low-Carbon Future”. In: *Journal of Engineering for Gas Turbines and Power* 143 (2021).

[30] A. Gruber et al. “Numerical and Experimental Investigation of a Geometrically Simplified, Two-Dimensional FlameSheet™ Hydrogen Burner”. In: *Proceedings of the ASME Turbo Expo 2023: Turbomachinery Technical Conference and Exposition. Volume 3B: Combustion, Fuels, and Emissions* (2023).

[31] T. Poinsot and D. Veynante. *Theoretical and Numerical Combustion*. 3rd ed. 2012.

[32] *Full Multicomponent Diffusion in Fluent*. Viewed on 12-08-2024. URL: https://www.afs.enea.it/project/neptunius/docs/fluent/html/ug/node320.htm.

[33] J. Warnatz, U. Maas, and R.W. Dibble. *Combustion: Physical and Chemical Fundamentals, Modeling and Simulation, Experiments, Pollutant Formation*. 2006.

[34] P. K. Kundu, I. M. Cohen, and D. R. Dowling. *Fluid Mechanics*. 6th ed. 2016.

[35] F.T.M. Nieuwstadt, J. Westerweel, and B.J. Boersma. *Turbulence: Introduction to Theory and Applications of Turbulent Flows*. 2016.

[36] *Basics of Turbulent Flow*. Viewed on 20-03-2024. URL: https://www.mit.edu/course/1/1.061/www/dream/SEVEN/SEVENTHEORY.PDF.

[37] Y. A. Çengel and J. M. Cimbala. *Fluid Mechanics: Fundamentals and Applications*. 3rd ed.

[38] J. Li et al. “An Updated Comprehensive Kinetic Model of Hydrogen Combustion”. In: *International Journal of Chemical Kinetics* (2004).

[39] G. Balakrishnan, M.D. Smooke, and F.A. Williams. “A numerical investigation of extinction and ignition limits in laminar nonpremixed counterflowing hydrogen-air streams for both elementary and reduced chemistry”. In: *Combustion and Flame* (1995).

[40] M. O’ Conaire et al. “A comprehensive modeling study of hydrogen oxidation”. In: *Int. J. Chem. Kinet.* 36 (2004).

[41] P. Boivin. *Reduced-Kinetic Mechanisms for Hydrogen and Syngas Combustion Including Autoignition*. 2011.

[42] *GRI-Mech*. Viewed on 06-02-2024. URL: http://combustion.berkeley.edu/gri-mech/releases.html.

[43] A.C. Benim and K.J. Syed. *Flashback Mechanisms in Lean Premixed Gas Turbine Combustion*. 2015.

[44] C.K. Law and C.J. Sung. “Structure, aerodynamics, and geometry of premixed flamelets”. In: *Progress in Energy and Combustion Science* 26 (2000), pp. 459–505.

[45] *Mass Diffusion Coefficient in Fluent*. Viewed on 12-08-2024. URL: https://www.afs.enea.it/project/neptunius/docs/fluent/html/ug/node322.htm.

[46] *Thermal Conductivity in Fluent*. Viewed on 12-08-2024. URL: https://www.afs.enea.it/project/neptunius/docs/fluent/html/ug/node298.htm.

[47] *Cantera Package*. Viewed on 06-02-2024. URL: https://cantera.org/.

[48] N. Peters. “The turbulent burning velocity for large-scale and small-scale turbulence”. In: *Journal of Fluid Mechanics* 384 (1999).

[49] N. Peters. “Laminar flamelet concepts in turbulent combustion”. In: *Symposium (International) on Combustion* 21 (1988).

[50] A.N. Lipatnikov and J. Chomiak. “Effects of premixed flames on turbulence and turbulent scalar transport”. In: *Progress in Energy and Combustion Science* 36 (2010), pp. 1–102.

[51] A.J. Aspden, M.S. Day, and J.B. Bell. “Characterization of low Lewis number flames”. In: *Proceedings of the Combustion Institute* 33 (2011).

[52] S.B. Pope. *Turbulent Flows*. 2000.

[53] A. Favre. “Statistical equations of turbulent gases”. In: *Problems of hydrodynamics and continuum mechanics* (1969).

[54] B.E. Launder and D.B. Spalding. “The numerical computation of turbulent flows”. In: *Computer Methods in Applied Mechanics and Engineering* 3 (1974).

[55] D.C. Wilcox. “Formulation of the k-w Turbulence Model Revisited”. In: *AIAA Journal* 46 (2008).

[56] F.R. Menter. “Two-equation eddy-viscosity turbulence models for engineering applications”. In: *AIAA Journal* 32 (1994), pp. 1598–1605.

[57] T. Shih et al. “A new k-□ eddy viscosity model for high reynolds number turbulent flows”. In: *Computers and Fluids* (1995).

[58] O. Colin et al. “A thickened flame model for large eddy simulations of turbulent premixed combustion”. In: *Physics of Fluids* 12 (2000).

[59] J. Smagorinsky. “General circulation experiments with the primitive equations”. In: *Monthly Weather Review* 91 (1963).

[60] F. Nicoud and F. Ducros. “Subgrid-Scale Stress Modelling Based on the Square of the Velocity Gradient Tensor”. In: *Flow, Turbulence and Combustion* 62 (1999).

[61] *Ansys Fluent*. Viewed on 19-07-2024. URL: `https://www.ansys.com/products/fluids/ansys-fluent`.

[62] J.H. Ferziger and M. Peric. *Computational Methods for Fluid Dynamics*. 3rd ed. 2002.

[63] T.S. Lund, X. Wu, and K.D. Squires. “Generation of Turbulent Inflow Data for Spatially-Developing Boundary Layer Simulations”. In: *Journal of Computational Physics* 140 (1998).

[64] A. Skillen, A. Revell, and T. Craft. “Accuracy and efficiency improvements in synthetic eddy methods”. In: *International Journal of Heat and Fluid Flow* 62 (2016).

[65] G.R. Tabor and M.H. Baba-Ahmadi. “Inlet conditions for large eddy simulation: A review”. In: *Computers and Fluids* 39 (2010).

[66] *Inlet Boundary Conditions for the LES Model in Fluent*. Viewed on 21-07-2024. URL: `https://www.afs.enea.it/project/neptunius/docs/fluent/html/th/node96.htm`.

[67] A. Smirnov, S. Shi, and I. Celik. “Random Flow Generation Technique for Large Eddy Simulations and Particle-Dynamics Modeling”. In: *Journal of Fluids Engineering* 123 (2001).

[68] J. Ströhle and T. Myhrvold. “An evaluation of detailed reaction mechanisms for hydrogen combustion under gas turbine conditions”. In: *International Journal of Hydrogen Energy* (2007).

[69] F. Liu et al. “Numerical study of the superadiabatic flame temperature phenomenon in hydrocarbon premixed flames”. In: *Proceedings of the Combustion Institute* (2002).

[70] J.L. Schurr et al. “Super adiabatic combustion of H2/Air and H2/N2O mixtures”. In: *Combustion and Flame* (2024).

A

Mass Diffusivity in Fluent

In this thesis, Fluent's multicomponent model [45] is used to calculate the mass diffusivity for a species i in species j. This model uses the kinetic theory (with ideal gas law enabled) to calculate the diffusivity by using the Lennard Jones parameters, the L-J characteristic length σ_i and the L-J energy parameter $(\epsilon/k_B)_i$.

Fluent uses a modified version of Chapman-Enskog formula to estimate the diffusion coefficient using kinetic theory:

$$D_{ij} = 0.00188 \frac{\left[T^3 \left(\frac{1}{M_{w,i}} + \frac{1}{M_{w,j}}\right)\right]^{\frac{1}{2}}}{p_{abs}\sigma_{ij}^2 \Omega_D} \tag{A.1}$$

where p_{abs} is the absolute pressure, M_w is the molecular weight and Ω_D is the diffusion collision integral calculated as a function of T_D^*, where:

$$T_D^* = \frac{T}{(\epsilon/k_B)_{ij}} \tag{A.2}$$

where k_B is the Boltzmann constant and $(\epsilon/k_B)_{ij}$ for the mixture is given by:

$$(\epsilon/k_B)_{ij} = \sqrt{(\epsilon/k_B)_i \epsilon/k_B)_j} \tag{A.3}$$

and σ_{ij} is calculated using:

$$\sigma_{ij} = \frac{1}{2}(\sigma_i + \sigma_j) \tag{A.4}$$

B

Thickened Flame Model in Fluent

In Fluent, the thickened flame model first calculates a thickening factor F in the following way:

$$F = \frac{N\Delta}{\delta_L} \tag{B.1}$$

where N is the number of points in the flame (default value is 8), δ_L is the laminar flame thickness and Δ is the grid size. The grid size and flame thickness are given by:

$$\Delta = V^{\frac{1}{3}} \tag{B.2}$$

$$\delta_L = \frac{D}{S_L} \tag{B.3}$$

where V is the volume of the cell, D is the thermal diffusivity and S_L is the laminar flame speed.

All species diffusion coefficients are multiplied by F and reaction rates are divided by F. In order to avoid any errors away from the flame, only the region in a narrow band around the flame front is dynamically thickened. This narrow band is calculated by multiplying F with another factor Ω, where:

$$\Omega = \tanh\left(\beta \frac{\overline{|R|}}{max(\overline{|R|})}\right) \tag{B.4}$$

where β is a constant with value 10 and $\overline{|R|}$ is the spatially filtered absolute value of reaction rate. Ω has a value of 1 in the band and 0 outside the band.

Since using a thickened flame model modifies the flame-turbulence chemistry, the reaction rate must be multiplied with an efficiency function $\mathcal{E}$, which is the ratio of the flame wrinkling factors with and without thickening, given by:

$$\mathcal{E} = \frac{1 + \alpha\Gamma_0 \frac{u'_{\Delta_e}}{S_L}}{1 + \alpha\Gamma_1 \frac{u'_{\Delta_e}}{S_L}} \tag{B.5}$$

where u'_{Δ_e} is the subgrid scale turbulent velocity, Δ_e is the filter width that corresponds to the thickened flame (default value is 10 times the local cell grid spacing). α, Γ_0 and Γ_1 are given by:

$$\alpha = \beta \frac{2 \ln 2}{3c_{ms}[\xi\sqrt{Re_t} - 1]} \tag{B.6}$$

where β is a parameter of order unity, c_{ms} is a constant with value 0.28 and ξ is a correction parameter that varies from 0 to 1 and it depends on the turbulence.

$$\Gamma_0 = 0.75 \exp(-1.2/(u'_{\Delta_e}/S_L)^{0.3})(\Delta_e/\delta_L^0)^{\frac{2}{3}} \tag{B.7}$$

$$\Gamma_1 = 0.75 \exp(-1.2/(u'_{\Delta_e}/S_L)^{0.3})(\Delta_e/\delta_L^1)^{\frac{2}{3}} \tag{B.8}$$

where superscript 1 refers to the thickened flame and 0 refers to the flame without thickening.

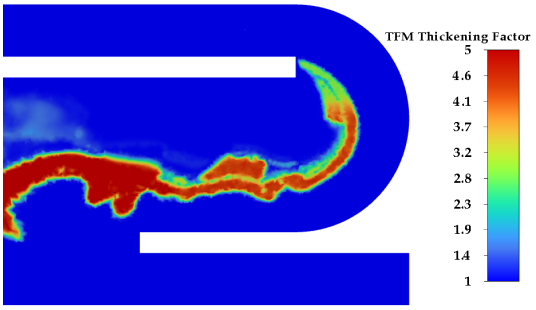

(a) Thickening Factor F

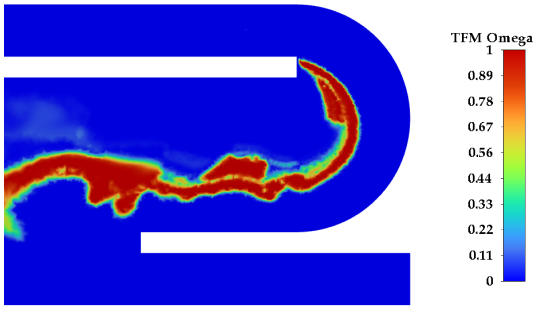

(b) Ω

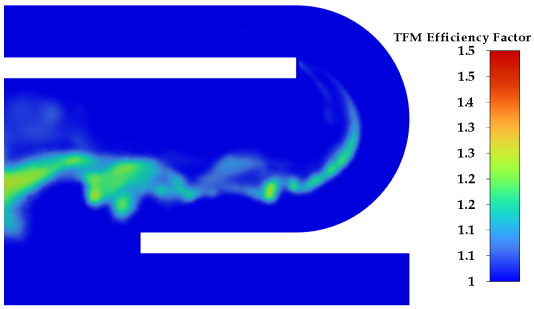

(c) Efficiency Function $\mathcal{E}$

Figure B.1: The Thickened Flame model's thickening factor F, Ω and Efficiency function $\mathcal{E}$ obtained from our reactive LES simulation

Figure B.1 shows the Thickened flame model parameters used in our simulations with Fluent. We can clearly see how Fluent uses the model in the region around the flame front by using the thickening factor F.